UNIVERSITÀ DEGLI STUDI DI PADOVA

Facoltà di Scienze Matematiche Fisiche Naturali

DIPARTIMENTO DI FISICA

Scuola di Dottorato di Ricerca in Fisica
XX ciclo

New materials for the next generation of criogenic gravitational wave detectors.

Direttore della Scuola: *Ch.mo Prof.* Attilio Stella
Supervisiore: *Ch.mo Prof.* Massimo Cerdonio Chiaromonte
Correlatore: *Dott.* Jean-Pierre Zendri

Dottorando: Nicola Liguori

DATA CONSEGNA TESI
31 Gennaio 2008

Riassunto.

Il lavoro di ricerca svolto per la presente tesi di dottorato riguarda la misura di dissipazioni meccaniche a bassa temperatura del silicio e del carburo di silicio come materiali candidati per la realizzazione della massa sensibile del rivelatore di onde gravitazionali di futura generazione DUAL.

Le misure sono realizzate presso la Test Facility (TF) ultra-criogenica sita nello stesso capannone che ospita il rivelatore di onde gravitazionali AURIGA, presso i Laboratori Nazionali di Legnaro (LNL), INFN, Padova. In attesa che il refrigeratore a diluizione della TF presso i LNL fosse operativo per il prossimo run ultracriogenico (2008), solo alcune misure ultracriogeniche sono state eseguite presso il Laboratorio di Basse Temperature del Dipartimento di Fisica dell'Università degli Studi di Trento.

La TF è stata inizialmente progettata per la misura del rumore termico di catene di trasduzione e amplificazione per rivelatori acustici di onde gravitazionali; in essa è stato eseguito il test del readout capacitivo completo del rivelatore AURIGA (cioè il trasduttore capacitivo, l'amplificatore a doppio stadio SQUID, lo stadio di adattamento risonante LC) nelle stesse condizioni fisiche in cui sarà operativo nel rivelatore principale. Il dottorando ha partecipato attivamente alla fase di upgrading per adattare questa struttura alla misura a temperatura criogenica e ultra-criogenica delle dissipazioni meccaniche dei materiali di interesse in campioni di forma circolare (dischi) o rettangolare (cantilevers).

La TF è stata equipaggiata della sensoristica necessaria a svolgere queste misure, cioè un attuatore piezoelettrico guidato da elettronica ad alta tensione, quattro linee di lettura e altrettante di carica per sensori di spostamento di tipo capacitivo, una linea di lettura per misure di spostamento con il metodo della leva ottica, quattro linee per termometri sensibili anche a bassa temperatura, lettori di pressione.

Sono stati sviluppati e realizzati sistemi di fissaggio a bassa dissipazione da applicare su campioni di forma circolare (dischi o wafer). In particolare è stato realizzato un sistema di sospensione cosiddetto

"nodale" per il quale il disco sottile viene fissato al centro tra due sfere. Poichè per molti modi normali il centro è un punto fisso, tale sistema di acchiappo non dovrebbe contribuire significativamente alla dissipazione totale. Questo sistema di sospensione nodale è stato sperimentato a temperature criogeniche nella versione con e senza colla sui punti di contatto. Tale sospensione nodale è stata utilizzata per le misure di angolo di perdita su dischi di carburo di silicio infiltrato e mono-cristallino di tipo 6H e 4H, e su dischi di silicio. In particolare sul silicio mono-cristallino con questa sospensione si sono misurati angoli di perdita estremamente bassi (dell'ordine di 10^{-8}) e si è evidenziato nettamente che sopra i 40 K la dissipazione dominante è quella termoelastica.

Le misure di dissipazione meccanica vengono eseguite con il metodo cosiddetto del "ring down" (eccitazione e misura del decadimento dei modi normali del campione in esame). È stato progettato e realizzato in pochi prototipi un sensore di spostamento di tipo capacitivo per campioni in materiale dielettrico (non conduttori). Il sensore è stato realizzato in due versioni, grande e piccola area. Esso è stato utilizzato nelle misure su silicio e su carburo di silicio mono-cristallino presentate in questo lavoro di tesi. Per esempio, utilizzando questo dispositivo si è misurata la curva della dissipazione termoelastica in funzione della temperatura di un disco sottile di silicio, riportata nella tesi. Esso viene tuttora utilizzato con successo per misure criogeniche di dissipazione meccanica. Si potrebbe valutare la possibilità che un tale sensore, se opportunamente ottimizzato, possa avere una sensibilità sufficientemente alta da consentire la misura del rumore termico. Questo potrebbe essere utile, per esempio, nel caso in cui il rivelatore DUAL venisse realizzato in materiale non conduttore.

Per quanto riguarda il carburo di silicio, le misure di dissipazione sono state eseguite su vari campioni realizzati in diversa forma e con diverse procedure di fabbricazione. Il carburo di silicio è stato indagato nei tipi sinterizzato, infiltrato e mono-cristallino nei politipi 4H e 6H. Nel migliore dei casi (6H-SiC) l'angolo di perdita misurato risulta dell'ordine di 10^{-7}, purtroppo ancora alto per le richieste del rivelatore DUAL. Comunque un miglioramento è atteso da trattamenti termici dei campioni.

Infine, allo scopo di valutare se la massa di DUAL puø' essere realizzata "incollando" campioni di silicio più piccoli, è stata fatta una prima misura delle perdite meccaniche di wafer di silicio realizzato tramite la cosiddetta tecnica del "direct bonding" (incollaggio diretto) di wafer più sottili. Il risultato di queste misure è che l'angolo di perdita dello strato di bonding è circa 5×10^{-3}, non lontano dalla richiesta di DUAL

(angolo di perdita dell'ordine di 10^{-3}).

La presente tesi di dottorato è strutturata come segue.

- Il capitolo 1 è semplicemente un'introduzione al lavoro sviluppato nella tesi. In essa si descrivono gli elementi di base e il contesto nel quale il lavoro di tesi si è sviluppato.

- Nel capitolo 2 si dà una visione d'insieme sul rivelatore DUAL. Viene presentato e discusso brevemente un certo numero di sorgenti di possibile interesse. La sensibilità attesa è confrontata con quella di altri rivelatori di futura generazione, come per esempio gli interferometri, nella stessa banda di frequenze. Segue una breve discussione sul principio di funzionamento del rivelatore: sono analizzate alcune questioni fondamentali come per esempio l'ottimizzazione allo Standard Quantum Limit e il ruolo cruciale della dissipazione del materiale. Infine viene trattato il caso del rivelatore DUAL a massa singola.

- Nel capitolo 3 è riportata una breve descrizione della Test Facility (TF) ultra-criogenica sita presso i LNL dell'INFN. La TF è descritta in ogni sua parte.

- Il capitolo 4 è interamente dedicato alla progettazione, ottimizzazione e calibrazione di un sensore di spostamento capacitivo per campioni non conduttori, come per esempio i wafer di silicio o il SiC nei politipi 4H e 6H. Essendo il dispositivo costituito da una serie di coppie identiche di elettrodi rettangolari, la stima della sua capacità viene eseguita dapprima nel caso di una singola coppia. Successivamente tre casi sono considerati consecutivamente per la coppia di elettrodi: spazio vuoto, presenza del substrato e infine presenza del campione come uno specchio di fronte alla serie completa di elettrodi. La sensibilità del sensore viene stimata considerando l'intero dispositivo come un numero di coppie di elettrodi di segno opposto connessi in parallelo. Quindi il sensore viene ottimizzato massimizzandone la sensibilità su un'area sensibile fissata. Esso viene realizzato in due prototipi, di grande e piccola area; quest'ultimo è stato calibrato su banco e la calibrazione è riportata nell'ultima sezione del capitolo 4.

- Nel Capitolo 5 sono raccolte le misure eseguite su silicio e silicio bondato. Sono descritti i campioni utilizzati e l'analisi dei loro modi normali con il metodo degli elementi finiti (FEM). Ulteriori dettaglio sul modello elastico del campione indagato sono riportati nella Appendice A. Sono poi descritti la sospensione nodale per i

dischi sottili e il readout ottico e capacitivo. Infine sono descritte e discusse un certo numero di cause di dissipazione meccanica e il loro contributo alle perdite totali.

- Similmente, nel capitolo 6 sono raccolte tutte le misure eseguite su diversi politipi del carburo di silicio. Molti argomenti sono in comune con il precedente capitolo, come per esempio la sospensione nodale, il readout, il procedimento di misura e così via. perciò questi argomenti vengono trattati molto brevemente. Più ampio spazio è dato alle misure criogeniche e ultra-criogeniche e alla discussione sulle possibili sorgenti delle perdite misurate.

- Il capitolo 7 è dedicato, infine, alle conclusioni e alle prospettive. I risultati ottenuti sono riassunti e commentati.

Abstract.

The research work developed in the present PhD thesis deals with the measurement of mechanical dissipations at low temperature of silicon and silicon carbide, as candidate materials in the carrying out the sensitive mass of the next generation gravitational wave detector DUAL.

Measurements are performed at the ultra-cryogenic Test Facility located in the same building that houses the gravitational waves detector AURIGA, at Legnaro National Laboratories (LNL), INFN, Padova, Italy. Few ultra-cryogenic measurements are performed at Low Temperature Laboratories, Physics Department, University of Trento, Italy, because in the meantime the LNL dilution refrigerator was under upgrading for the next (2008) ultra-cryogenic run. Early the Ultra-Cryogenic Transducer Test Facility was designed in order to measure the thermal noise of transduction and amplification chains for acoustic detectors of gravitational waves; it allowed to test the whole capacitive readout of the AURIGA detector (i.e. capacitive transducer + double stage SQUID amplifier + resonating LC matching line) in the same environment as it will be operating in the main detector. The writer participated actively to the upgrading phase in order to rearrange this apparatus for mechanical dissipation measurements of interesting materials in samples of circular (disks) or rectangular (cantilevers) shape, as function of cryogenic and ultra-cryogenic temperature.

TF has been provided for all the sensors required to perform these measurements, i.e. a piezoelectric actuator driven by high voltage amplifier, four readout and as much as charge lines for capacitive displacement sensors, a readout line for displacement measures to be performed by the optical lever method, four lines for thermometers sensitive also at low temperature, pressure sensors.

Low losses clamping systems has been developed to be employed on samples of circular shapes (wafers or disks). In particular, a clamping system so called "nodal" has been developed. With this nodal suspension a thin disk is clamped on its centre by two spheres. Since for most normal modes the centre is at rest, nodal suspension should contribute in neglecting amount to total loss. This type of nodal sus-

pension has been experimented at cryogenic temperatures in the two versions with and without glue on contact points. Such nodal suspension has been employed in loss angle measurements on infiltrated and mono-crystalline (polytypes 4H and 6H) silicon carbide disks. In particular, on mono-crystalline silicon, employing this suspension, very low loss angles has been measured (of the order of 10^{-8}) and it was pointed out that above 40 K thermoelastic dissipation dominates.

Mechanical loss measurements are performed by the so called "ring down" method (excitation and decay acquisition of the normal modes of the sample under investigation). A special capacitive displacement sensor has been designed and carried out in few prototypes for samples of dielectric material (not conductors). This sensor was carried out in two models, large and small area. It has been employed in loss angle measurements on silicon and mono-crystalline silicon carbide, reported in the present thesis. For instance, employing this sensor, the thermoelastic dissipation curve has been measured as function of temperature for a thin silicon wafer, as reported in the thesis. This sensor is still employed successfully for cryogenic measurements of mechanical dissipation. It could be evaluated the possibility that, if suitably optimized, this sensor could have a displacement sensitivity high enough to allow the measurement of thermal noise. This could be very useful, for instance in the case that DUAL detector should be carried out in a non conductor material.

As concerning silicon carbide, mechanical dissipation measurements have been performed on different samples of different fabrication methods. Silicon carbide was investigated as sintered, infiltrated and 4H and 6H mono-crystalline polytypes. In the best case (6H-SiC) the measured loss angle results of the order of 10^{-7}, unfortunately still too high to fit the requirements of DUAL detector. However an improvement is awaited from thermal post processing on samples.

Finally, in order to estimate if the whole mass of DUAL detector could be machined bonding together smaller silicon parts, the first measurement of mechanical dissipation as a function of temperature has been performed on a silicon wafer that was made by direct bonding technique starting from three thinner wafers. The result of these measurements is that the measured loss angle due to the (two) bonding layers is about 5×10^{-3}, not far from the DUAL requirement (loss angle of the order of 10^{-3}.

The present thesis is structured as follows.

- Chapter 1 is simply an introduction to the work developed in the thesis. It describes the basis elements and the contest in which the thesis is developed.

- In Chapter 2 an overview on DUAL detector is reported. A number of possible interesting sources are listed and discussed. The expected sensitivity is compared with the one of other future generation detectors, like as interferometers, in the same frequency band. A brief discussion follows on detector's working principle: they are analyzed some fundamental issues like for instance an estimation of the detector thermal noise and the optimization at the Standard Quantum Limit and the crucial role of the material's dissipation. Finally the case of the single mass DUAL detector is dealt with.

- A brief description of the ultra-cryogenic Test Facility located at LNL laboratories of INFN is reported in Chapter 3. The facility is described in all its parts.

- Chapter 4 is entirely dedicated to design, optimization and calibration of a capacitive displacement sensor for not conductive samples, as for instance silicon wafers or 6H and 4H SiC. Being the device made of an array of rectangular identical electrode pairs, the estimation of capacity is made in the case of a single couple first. Three cases are considered in succession for the electrodes couple: free space, presence of the substrate, and presence of the sample as a mirror in front of the multistrip array. The device sensitivity is evaluated considering the whole array as a number of couples connected in parallel. Then the device is optimized maximizing the sensitivity over the fixed sensitive area. Two prototypes were realized, with large and small area; the latter calibration on bench is reported in the last section of Chapter 4.

- All measurements on both bulk and bonded silicon are collected in Chapter 5. The employed sample is described and its normal modes are analyzed by Finite Element Method (FEM). More details on the elastic model of the sample are reported in the Appendix A. The nodal suspension for thin disks, capacitive and optical readout are described in details. Finally, a number of dissipation sources and their contribution to total losses are described and discussed.

- Similarly, Chapter 6 collects all measurements and results about the different polytypes of Silicon Carbide. Many topics are shared with the previous chapter, such as the nodal suspension, readout, measurement process and so on. For this reason these topics are dealt with very briefly. Large space is dedicated to cryogenic and

ultra-cryogenic measurements and to a discussion about possible sources of measured losses.

- Finally, Chapter 7 is dedicated to conclusions and perspectives. Obtained results are summed up and commented.

Contents

a Francesco

Chapter 1

Introduction.

The DUAL collaboration is investigating a new kind of acoustic gravitational wave detector which can provide both high sensitivity and wide bandwidth ([5], [6], [7]). [1] In order to check the feasibility and to optimize the design, a R&D program was proposed and approved for duration of 3 years. It is a feasibility study and its aim is to understand if, at the present situation of knowledge, the detector can be carried out. The results of the R&D will be the demonstration at prototype level of the relevant technologies needed for the realization of the readout, performing a complete study of the most critical issues:

- detector design: identification of the optimal configuration with respect to both sensitivity and bandwidth;
- readout system: readout configuration towards the Standard Quantum Limit (SQL);
- test mass development: choice of material and fabrication method.

The work developed in the present PhD thesis enters in the 3rd point. We are looking for a material to make with the sensitive mass for the DUAL detector. The material to be chosen has to satisfy a number of requirements in order to optimize the detector wide bandwidth and sensitivity. It can be shown that the detector sensitivity scales as the ratio Y^2/ρ, where Y is the Young's modulus and ρ is the density of the material. This is true under the following hypothesis

- the readout of the system is optimized at the Standard Quantum Limit (SQL);
- the topology of the sensitive mass is fixed to have cylindrical symmetry;

[1] Throughout the present introduction, references can be found in the bibliography for chapter 1.

- thermal noise contribution is not included in the calculations;
- the same sensitivity bandwidth is assumed.

The thermal noise contribution to the total detector sensitivity is also included in calculations. It is proportional to the product $T\phi$, where ϕ is the material loss angle [10]. It can be shown that the condition to have thermal noise negligible or comparable to not eliminable noise due to readout is to have a material such that $T\phi 10^{-9} \div 10^{-8}$. Here the choice of the material for the test mass takes a very crucial role in the sensitivity optimization. The requirement $T\phi \lesssim 10^{-8}K$ looks like a good compromise between high sensitivity (of the order of few $10^{-23}1/\sqrt{Hz}$) and reasonable feasibility in terms of machinability.

Besides, fixed the sensitive wide bandwidth (at present around 1-5 kHz), the material physical properties determine the size of the sensitive test mass of the detector, but commercial feasibility and/or machinability impose a limit in the available size depending on the material properties and the factory production capabilities. At present the maximum size available for the cylindrical topology is about 3m in length and 1m in diameter for infiltrated silicon carbide.

Summing up, in order to optimize the detector sensitivity, we need that material satisfies the following requirements:

- it should maximize the ratio Y^2/ρ;
- its internal dissipation should be such that the product $T\phi \lesssim 10^{-8}$;
- its cost should be not too much expensive to fit the budget;
- it should be feasible in large size to assure an high sensitive mass cross section.

Physical properties of material contribute to the detector sensitivity figure crucially. In order to easily compare each with other sensitivities evaluated for different materials, we usually refer to DUAL detector sensitivity evaluated with the well-known physical properties of Al5056, that is the material traditionally employed for bar detectors.

In Table 1.1 different materials are compared with Al5056. In the second column it is reported the obtainable sensitivity employing the material indicated in the first column, normalized to the obtainable sensitivity with Al5056. The table collects present knowledge on dissipation at low temperature.

Having a look to the table, it appears that silicon carbide could offer a good chance in DUAL sensitivity optimization. Infiltrated SiC

can be machined in objects of large size but on the other hand offers lower sensitivity than a sintered SiC made detector, which, on the contrary, is feasible only in small size. On the other hand, silicon carbide presents the drawback that intrinsic loss is unknown. In the present work, since not available in literature, loss angle measurements as function of temperature (in particular at low temperature) of silicon carbide are reported, with some measurements on infiltrated silicon carbide at ultra-cryogenic temperature down to 200 mK.. Different polytypes of SiC were investigated such as sintered α– and infiltrated C– SiC, and mono-crystalline SiC of types 4H and 6H.

Silicon is another interesting material for the manufacture of the detector test mass. However this material is feasible in large dimensions only by bonding together smaller parts. The possible employment of silicon has to be evaluated taking into account the dissipation due to bonding. Silicon presents a not very high value for $S^{Si}/SAl5056$, but in literature its losses are largely reported as function of temperature. According to measurements reported in literature, silicon should have internal dissipation such that $T\phi < 10^{-8}$ even without employing ultra-cryogenics. Mono-crystalline silicon mechanical losses were measured also, with the purpose to estimate bonding layer contribute in total losses. Measurements were made on cantilevers samples for silicon carbide and, for the first time, on nodal suspended flat plates for silicon, bonded silicon and silicon carbide in the $3 \div 300K$ range of temperature.

Molybdenum offers another possibility but it presents the same disadvantage as silicon, i.e. it is not feasible in large size. Loss angle measurements as function of temperature are still not performed.

All measurements were made at the Legnaro National Laboratories (LNL) Test Facility (TF) of Istituto Nazionale di Fisica Nucleare (INFN). This site, in origin born to measure the thermal noise of gw detector electromechanical transducers at cryogenic and ultra-cryogenic temperature, was especially upgraded for assembling and measuring several samples in a single run. In particular, a specific "comb" capacitor was designed, optimized in sensitivity and realized especially to transduce the sample vibration to an electrical signal for not conductive materials as silicon. It is needed since the ring down method performs the loss angle measurement, acquiring the displacement amplitude exponential decay at resonant frequency. It was employed in all measurements reported in this work on both bulk and bonded silicon in the whole 3÷300 K range.

Chapter 1 is simply an introduction to the work developed in the thesis. It describes the basis elements and the contest in which the

Table 1.1: DUAL detector sensitivity $S_h h$ evaluated for different materials and compared with the sensitivity evaluated for Al5056, the material of bar detectors operating. $S_h h$ is optimized over the same frequency window for all materials.

Material	$\frac{S_{hh}^{mat}}{S_{hh}^{Al5056}}$	ϕ (low temp)	Constraints
Diamond	163	(?)	Very expensive.
Infiltrated SiC	10	$> 10^{-6}$	Feasible in large dimensions.
Sintered SiC	27	$> 10^{-6}$	Not Feasible in large dimensions.
Beryllium	24	10^{-6}	Expensive.
Molybdenum	6.8	10^{-7}	Not machinable in large dimensions. Bonding needed. Available samples at LNL now.
Mono-Crystalline Silicon	4.4	$> 10^{-8}$	Bonding needed.(Max diam. $\sim$350 mm (USA). Mass limit $\sim$ 300-400 Kg.

thesis is developed.

In Chapter 2 an overview on DUAL detector is reported. A number of possible interesting sources are listed and discussed. The expected sensitivity is compared with the one of other future generation detectors, like as interferometers, in the same frequency band. A brief discussion follows on detector's working principle: they are analyzed some fundamental issues like an estimation of the detector thermal noise and the optimization at the Standard Quantum Limit. Finally the case of the single mass DUAL detector is dealt with.

A brief description of the ultra-cryogenic Test Facility at LNL laboratories of INFN is reported in Chapter 3. The facility is described in all its parts.

Chapter 4 is entirely dedicated to design, optimization and calibration of a capacitive displacement sensor for not conductive samples, as for instance silicon wafers or 6H and 4H SiC. Being the device made of an array of rectangular identical electrode pairs, the estimation of capacity is made in the case of a single couple first. Three cases are considered in succession for the electrodes couple: free space, presence of the substrate, and presence of the sample as a mirror in front of the multistrip array. The device sensitivity is evaluated considering the whole array as a number of couples connected in parallel. Then the

device is optimized maximizing the sensitivity over the fixed sensitive area. Two prototypes were realized, with large and small area; the latter calibration on bench is reported in the last section of Chapter 4.

All measurements on both bulk and bonded silicon are collected in Chapter 5. The employed sample is described and its normal modes are analyzed by Finite Element Method (FEM). More details on the elastic model of the sample are reported in the Appendix A. The nodal suspension for thin disks, capacitive and optical readout are described in details. Finally, a number of dissipation sources and their contribution to total losses are described and discussed.

Similarly, Chapter 6 collects all measurements and results about the different polytypes of Silicon Carbide. Many topics are shared with the previous chapter, such as the nodal suspension, readout, measurement process and so on. For this reason these topics are dealt with very briefly. Large space is dedicated to cryogenic and ultra-cryogenic measurements and to a discussion about possible sources of measured losses.

Finally, Chapter 7 is dedicated to conclusions and perspectives. Obtained results are summed up and commented.

Chapter 2

The DUAL Detector.

2.1 Introduction.

Over the last 40 years substantial progresses have been made about instruments and methods to search for gravitational waves from celestial sources. Resonant mass detectors were historically the first to come to continuous operation and have been improved by 4 orders of magnitude in energy sensitivity. Today they can detect energy changes of a 2300 kg bar as little as a few hundred of quanta of vibration at about 1 kHz with a bandwidth of about 100 Hz [1]. During 1999-2000 five and during 2003-2004 four bar detectors worldwide distributed have operated for few years as a network, giving significant upper limits to the yearly rate of high energetic emissions of Gravitational Waves (GW) in the Galaxy [2], [3]. A first generation of long baseline interferometric detectors is now operating or upgrading complemented by upgraded bars, so that together they may well have a chance to give a first detection in the next few years.

The direct detection of GWs remains an important goal in today's experimental physics because this detection will be a very strong experimental verification of Einstein's General Relativity theory. On the other hand the scientific interest is moving toward the possibility of studying the physical and astrophysical features of the gravitational radiation. In fact gravitational waves carry unique information about the coherent bulk matter generating the radiation, revealing features of their sources which are impossible to investigate by electromagnetic, cosmic rays or neutrino experiments. However it is commonly accepted in the scientific community that to enter the *Observatory Phase* and open a new GW astronomy, substantial improvements in detector sensitivity should be achieved. Traditional acoustic detectors are limited

in bandwidth typically at 10% of the resonant frequency. [1] Bandwidth enhancements in a traditional acoustic detector has been obtained introducing a two-modes (mechanical + electrical) resonant readout [4]. But a different approach is needed to fully exploit the potential sensitivity of acoustic detectors and make them complementary to the advanced versions of interferometric detectors.

2.2 Expected sources in high frequency range.

It's now common idea that a complete and wide GW frequency range sensitive observatory will let scientists follow the source system evolution during a time interval long enough to improve signal reconstruction and detection probability. For this reason collaborations are ongoing to set up the *multi-window observation* concept, i.e. the linking between different GW detectors (acoustic detectors, interferometers) and all the other astronomical telescopes and particles detectors. In particular the DUAL detector covers the high frequency band side (at present 1 - 5 kHz) of the GW spectrum. It could contribute to detect the following sources:

Binary systems of coalescing neutron stars or black holes. The system spiral produces a chirping signal from the lowest frequencies of the network up to the range of kHz. The merger event is still not well understood, but at present seems clear that the ringdown should be in the range 1 - 10 kHz for few solar masses binary systems. Such systems should be detectable up to few hundred Mpc. A so large volume of space lets us suppose a reasonable event rate (1/y) detectable.

Newborn magnetars. Magnetars are neutron stars characterized by an high magnetic field ($\geq 10^{15} Gauss$) and an high spin. The resulting force on the superficial shells of the star should deform its shape, oblating it. Hence the star results in a monochromatic GW emitter, where the fading is due to the slowing down in the rotation by emission of energy in GWs. It seems that such GW sources should emit around 1-2 kHz band, with about few/year event rate.

Perturbed relativistic stars. Newborn neutron stars undergo bars instabilities or oscillate in their quasi normal modes (such as f-modes or r-modes), and emit gravitational waves in the kHz range.

[1] This limit is due to the usage of resonant transducers, which is needed to reduce the effect of the final amplifier noise.

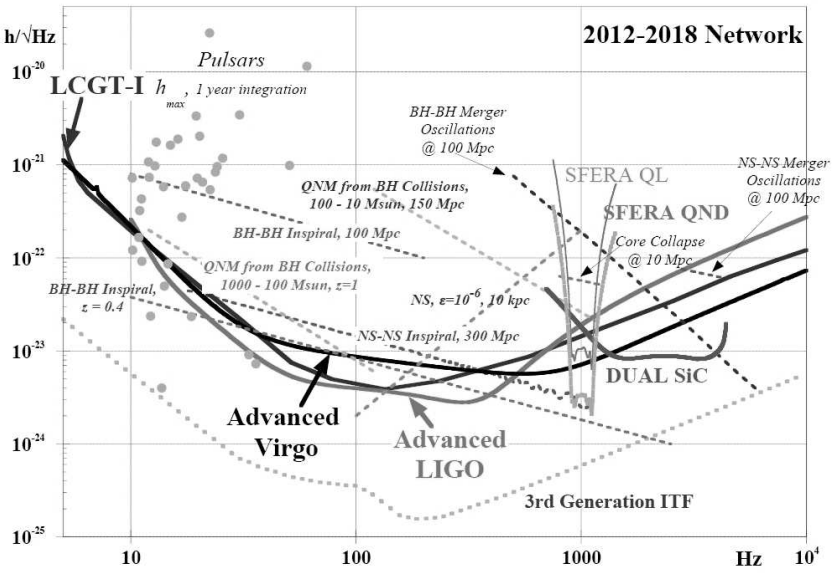

Figure 2.1: Sensitivity of Advanced VIRGO - Advanced LIGO - DUAL SiC at Quantum Limit detectors, with the estimated levels of some GW sources.

The properties of these signals depend crucially on the dynamical properties of the stars and therefore on their structure, composition and equation of state. In particular insight could be made on the precise equation of state of matter at supernuclear density.

Supernovae and GRBs as impulsive sources. This rare events spread the energy transported by the GW in a large frequency band and their detection is optimised by a very broad band network of detectors with different detection methods and frequency ranges.

Low Mass X-Ray Binaries. LMXBs have a constant supply of energy from the accretion. The GW frequency will be twice the spin frequency of the neutron star. The signal will be modified due to Doppler shifting from the neutron star in its orbit as well as possible changes in the neutron star spin due to the accretion. Thus, the signal is "dirty" and may be difficult to extract, but the number of known potential sources is about 100, and the position and frequency are reasonably well known.

In Figure 2.1 we show the sensitivity of DUAL SiC at Quantum Limit compared with Advanced VIRGO and Advanced LIGO. In the same graphic the estimated levels of the previous kind of sources and more others is shown.

2.3 DUAL detector scheme description.

One of the most characteristic properties of GW is their quadrupolar nature; hence a GW detector will reveal only quadrupolar waves. This property offers the possibility to design the detector so that its quadrupolar modes naturally select the signal of a quadrupolar GW impinging on. This idea of selectivity is the main concept of DUAL detector. For what about DUAL final configuration, work is still in progress, so here only the main scheme of the detector will be dealt with, without describing many specific technical details.

A DUAL detector is formed by two nested massive bodies whose quadrupolar modes resonate at different frequencies. Historically, in the first idea of DUAL, the two resonators were two spheres, an inner full one and a hollow outer the other [8]; then a dual cylinder configuration was taken into consideration, where the role of resonators passes from nested spheres to nested cylinders [9]. Recently DUAL collaboration developed a new version of the detector, with all the characteristic of the two nested cylinders but carried out with just one cylindrical sensitive mass [10]. In this case it is so called "single dual" detector. If the dual detector is implemented with two different bodies, the signal is read in the gap between the two masses as their differential deformations; the centers of mass of the two bodies coincide and remain mutually at rest while the masses resonate. In this way the rest frame of the measurement is provided.

In the case of a single dual cylinder detector, the work is still in progress. For what concerns the readout, at present it seems that a mechanical leverage inside the cylinder's hollow can not allow high sensitivity enough, both with optical and capacitive readout [13]. Recently the collaboration is considering the possibility to read the signal outside the hollow cylinder, at the edge of whips suitably designed to maximize the transfer of the energy in the sensitivity bandwidth [12]. The sensitivity of both the dual and the single dual detector is predicted to be of interest in the frequency range between the first two quadrupolar modes. It can be as broad as a few kHz in the kHz range.

The basic detector scheme consists of a test mass and a readout system. The physical observable is namely the average displacement over a sensitive area. Provided that all external noise sources are reduced down to a negligible level, the main ones that cause changing in the test mass dimensions are the external gravitational wave force, the back action force from the readout and the thermal noise force.

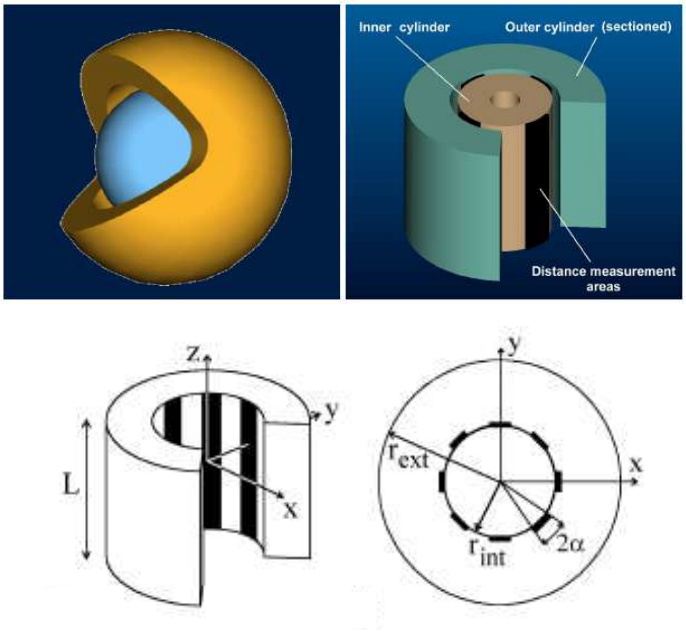

Figure 2.2: Different dual detector configurations. Up left: dual spheres. Up right: dual cylinder. Bottom: single dual cylinder, prospect view (left) and top section (right). (Left) Test mass and readout: here the picture shows the case in which the displacement induced by the impinging GW is measured in 8 regions(in black) spanning the whole cylinder height L. (Right) Section of the detector: the angle α determines the extent of the measuring surfaces.

2.3.1 One dimensional model.

Basically, a dual detector can be schematized as one dimensional system as shown in Figure 2.3(a): x_1 and x_2 are the positions of two different and independent mechanical oscillators, respectively; the external force F_e drives the two oscillators and it is evaluated by the measure of the difference $x_d = x_1 - x_2$. Be ν_s and ν_f the frequencies of the slow and the fast resonator, respectively. For $\nu < \nu_s, \nu_f$, the two resonators are in phase; for $\nu_s < \nu < \nu_f$, F_e drives the slow resonator above its resonant frequency and the fast one below, so that the responses of the two are out of phase by π radians. Therefore the distance x_d results in a signal enhancement with respect to the response of the single oscillators (see Figure 2.3(b)). The transfer function of the whole dual detector $H_{F_e} = x_d/F_e$ reflects this behaviour between the two resonance frequencies (see Figure 2.3(c)).

The back-action noise force drives the two oscillators coherently with opposite directions so that the system response is quite in phase within the sensitive bandwidth; hence the differential displacement consequent to the back action noise is highly depressed and vanishes at a frequency f^{**} as shown by its transfer function $H_{ba} = x_d/F_{ba}$ (see Figure 2.3(c)). The result is a reduction of the back action noise within the sensitivity frequency bandwidth of the detector [13].

2.4 Mode expansion.

In the case of a three-dimensional body, the dynamics of elastic deformations is described as the superposition of the dynamics of an almost infinite number of normal modes of vibration [14]. Let us consider an elastic body of density ρ. Let $\mathbf{u}(\mathbf{r}, t)$ be the displacement field of the elastic body and $L[\mathbf{u}(\mathbf{r}, t)]$ be the operator defined as following:

$$L[\mathbf{u}(\mathbf{r}, t)] \equiv (\lambda + \mu)\nabla(\nabla \cdot \mathbf{u}) + \mu\nabla^2\mathbf{u}, \tag{2.1}$$

where the *Lamè coefficients* λ and μ depend on the Poisson's ratio σ_p and the Young modulus Y of the material, according to the following definitions

$$\lambda \equiv \frac{Y\sigma_p}{(1+\sigma_p)(1-2\sigma_p)} \qquad \mu \equiv \frac{Y}{2(1+\sigma_p)} \tag{2.2}$$

Let the body be forced by a force density $\mathbf{F}(\mathbf{r}, t)$. Then the equations of the motion for the body can be written as

$$\rho \quad \frac{\partial^2\mathbf{u}(\mathbf{r}, t)}{\partial t^2} - L[\mathbf{u}(\mathbf{r}, t)] = \mathbf{F}(\mathbf{r}, t), \tag{2.3}$$

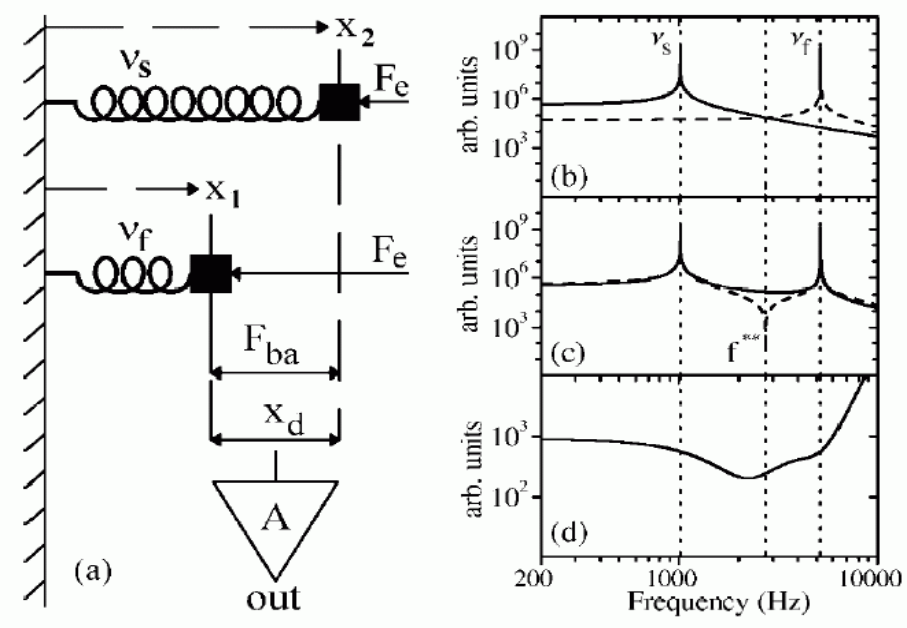

Figure 2.3: (a) One-dimensional "dual" detector. The same force F_e is measured by the relative displacement x_d of two resonators. (b) Transfer functions of the slow resonator (continuous line) and of the fast resonator (dashed line). (c) Dual detector transfer functions. Signal $H_{F_e} = x_d/F_e$ (continuous line), back-action $H_{b_a} = x_d/F_{b_a}$ (dashed line). (d) Wideband optimized noise.

with the properly initial and boundary conditions. The displacement normal modes $\mathbf{w}_n(\mathbf{r})$ are defined as the solutions of the eigenvalues problem as

$$-\rho\omega_n^2\mathbf{w}_n = L\left[\mathbf{w}_n\right]. \tag{2.4}$$

The boundary conditions on $\mathbf{w}_n$ are given requiring that the component of stress vector vanishes when normal to the test mass external surface on this surface itself. The normal modes are a complete orthogonal system and they can be normalized to satisfy the following condition:

$$\int_V \mathbf{w}_n(\mathbf{r})\cdot\mathbf{w}_m(\mathbf{r})dV = M\delta_{nm}, \tag{2.5}$$

where M is the total mass and the volume integral is calculated overall the test mass volume V. The field $\mathbf{u}(\mathbf{r},t)$, as solution of the equations of motion 2.3, can be written as superposition of normal modes as:

$$\mathbf{u}(\mathbf{r},t) = \sum_n \mathbf{w}_n(\mathbf{r})q_n(t). \tag{2.6}$$

The functions $q_n(t)$ represent the time development of the (n)-th mode with initial value given by:

$$q_n(t) = \frac{1}{M}\int_V dV\rho \quad \mathbf{u}(\mathbf{r},0)\mathbf{w}_n(\mathbf{r}). \tag{2.7}$$

If in the driving force the dependence of time t and coordinates $\mathbf{r}$ can be parted, so that the force can be written as

$$F(\mathbf{r},t) = G_t(t)\mathbf{G}_r(\mathbf{r}) \tag{2.8}$$

then the equation (2.3) becomes

$$\rho\sum_n \mathbf{w}_n(\mathbf{r})\frac{\partial^2 q_n(t)}{\partial t^2} - \sum_n q_n(t)L\left[\mathbf{w}_n(\mathbf{r})\right] = G_t(t)\mathbf{G}_r(\mathbf{r}). \tag{2.9}$$

Applying the eigenvalue equation (2.4), multiplying by $\mathbf{w}_n$ and using the orthonormality equation (2.5) we obtain:

$$M\frac{\partial^2 q_m(t)}{\partial t^2} + M\omega_m^2 q_m(t) = G_t(t)\int_V dV\mathbf{G}_r(\mathbf{r})\cdot\mathbf{w}_n(\mathbf{r}). \tag{2.10}$$

We can observe that the time development of the m-th normal mode obeys the equation of a forced harmonic oscillator. Then in the frequency domain we have:

$$\widetilde{q}_m(\omega) = \frac{1}{M}\frac{\widetilde{G}_t(\omega)}{\omega_m^2-\omega^2}\int_V dV\mathbf{G}_r(\mathbf{r})\cdot\mathbf{w}_n(\mathbf{r}). \tag{2.11}$$

In the hypotheses that dissipation is due to the structure of the material, the losses can be described in frequency domain including explicitly a damping term in the functions $\widetilde{q}_m$, describing the evolution in time, like in the following:

$$\widetilde{q}_m(\omega) = \frac{1}{M}\frac{\widetilde{G}_t(\omega)}{\omega_m^2 - \omega^2 + \imath\omega_m^2\phi_m(\omega)}\int_V dV\mathbf{G}_r(\mathbf{r})\cdot\mathbf{w}_n(\mathbf{r}). \tag{2.12}$$

The function $\phi_m(\omega)$ represents the loss angle of the material. It is experimentally found that $\phi_m(\omega)$ is roughly constant and this is usually referred as *structural damping*. For low loss materials it is $\phi_n \ll 1$. It is possible to observe that the normal mode expansion is possible only if the damping term is homogeneous overall the test mass volume. On the contrary, if the material presents inhomogeneities in its structural damping, these cause couplings between different normal modes [16].

2.5 Readout.

In order to detect the external force, we measure the resulting strain on some fixed test mass surface S. The observable physical quantity is the displacement X. In approximation of small displacement, the observable of the system X may be defined as

$$X(t) = \int_S dS\mathbf{P}(\mathbf{r})\cdot\mathbf{u}(\mathbf{r},t). \tag{2.13}$$

Here $\mathbf{P}(\mathbf{r})$ is the weighting function relative to the chosen topology readout. The integral is calculated over the chosen readout surface S of the test mass. The readout surface S is a fraction of the whole external surface of the test mass. We may chose freely the topology of S and the relative weight function determining the output variable $X(t)$. The spatial form of the weight function $\mathbf{P}(\mathbf{r})$ reflects the chosen measurement strategy and detection scheme. For example, in a capacitive readout it is $P(r) = 1/S_0$ on the surface S_0 of the electrodes and $P(r) = 0$ elsewhere (neglecting border effects).

Writing the displacement field $\mathbf{u}$ in series of normal modes in the definition (2.13), the observable physical quantity X takes the following form:

$$X(t) = \sum_n q_n(t)\int_S dS\mathbf{P}(\mathbf{r})\cdot\mathbf{w}_n(\mathbf{r}), \tag{2.14}$$

and in the frequency domain

$$\widetilde{X}(\omega) = \frac{\widetilde{G}_t(\omega)}{M}\sum_n \frac{[\int_V dV\mathbf{G}_r(\mathbf{r})\cdot\mathbf{w}_n(\mathbf{r})][\int_S dS\mathbf{P}_r(\mathbf{r})\cdot\mathbf{w}_n(\mathbf{r})]}{\omega_n^2 - \omega^2 + i\omega_n^2\phi_n(\omega)} \tag{2.15}$$

Given the readout weight function and the analytic form of the driving force, the previous equation returns the motion of the system and then allows to evaluate the transfer function when the detector is driven by gravitational wave, readout back action and thermal noise forces, which are the most relevant ones acting on the test mass.

Gravitational Wave Transfer Function. We consider here the case of a linearly polarized gravitational wave propagating along the z-axis, the longitudinal axes of the cylindrical symmetry of the test mass. Choosing the cylindrical coordinates (r, θ) and according to Misner, Thorne and Wheeler [17], the force density applied on the system may be written as

$$\begin{aligned} G_t(t) &= \frac{1}{2}\rho\ddot{h}(t) \\ \mathbf{G}_r(\mathbf{r}) &\equiv \mathbf{W}(\mathbf{r}) = r\cos(2\theta+\psi)\mathbf{i}_r - r\sin(2\theta+\psi)\mathbf{i}_\theta. \end{aligned} \tag{2.16}$$

Here $h(t)$ is the metric perturbation associated to the GW, ψ is the polarization of the GW ($\psi = 0 \Leftrightarrow +$ polarization, $\psi = \pi/4 \Leftrightarrow \times$ polarization). If we substitute the previous equation (2.16) in the equation (2.15) then it appears that the displacement response of the system to the metric perturbation h is written as

$$\widetilde{X}(\omega) = \widetilde{h}(\omega) H_{GW}(\omega), \tag{2.17}$$

where $H_{GW}(\omega)$ is the detector transfer function:

$$\begin{aligned} H_{GW} &= \frac{1}{2V} \\ &\sum_n \frac{-\omega^2 [\int_V dV \mathbf{W}_r(\mathbf{r}) \cdot \mathbf{w}_n(\mathbf{r})][\int_S dS \mathbf{P}_r(\mathbf{r}) \cdot \mathbf{w}_n(\mathbf{r})]}{\omega_n^2 - \omega^2 + i\omega_n^2 \phi_n(\omega)} \end{aligned} \tag{2.18}$$

Back Action Transfer Function. This force is exerted by the readout and hence it is applied proportionally to the weight function $\mathbf{P}(\mathbf{r})$:

$$\mathbf{F}_{BA}(t, r) = F_{BA}\mathbf{P}(\mathbf{r}). \tag{2.19}$$

Substituting the back action force (2.19) instead of the volume force field $G_t(t)\mathbf{G}_r(\mathbf{r})$ in the equation (2.15) we can evaluate the response of the system in terms of displacement:

$$\widetilde{X}(\omega) = \frac{\widetilde{F}_{BA}(\omega)}{M} \sum_n \frac{\left[\int_S dS \mathbf{P}(\mathbf{r}) \cdot \mathbf{w}_n(\mathbf{r})\right]^2}{\omega_n^2 - \omega^2 + i\omega_n^2 \phi_n(\omega)}. \tag{2.20}$$

Being for definition $\widetilde{X}(\omega) = T_{BA}\widetilde{F}_{BA}(\omega)$, comparing with the previous equation we deduce the expression of the transfer function of the system:

$$T_{BA} = \frac{1}{M}\sum_n \frac{\left[\int_S dS\mathbf{P}(\mathbf{r})\cdot\mathbf{w}_n(\mathbf{r})\right]^2}{\omega_n^2 - \omega^2 + i\omega_n^2\phi_n(\omega)}. \tag{2.21}$$

It is interesting to point out that the displacement response of the detector to the back action force is the coherent sum of the contributions of independent harmonic oscillators, each of them corresponding to a normal mode of the system and forced by the same driving force $F_{BA}(t)$. Different modes can even give a displacement contribute in opposite direction but only the resulting sum is physically observable.

2.6 Thermal Noise.

The so called brownian or thermal noise is due to the fluctuations of the volume of the body as a consequence of the thermal oscillations of atoms inside the molecular lattice.

According to Callen and Welton [18], we consider the case of a system at equilibrium with a bath at temperature T described by a single coordinate p. The force F represents the interaction between the system and the external environment. The fluctuation-dissipation theorem predicts the single sided thermal noise power spectrum of the coordinate p as:

$$S_{pp} = -\frac{4k_BT}{\omega}\Im\left[T_F(\omega)\right]. \tag{2.22}$$

where $T_F(\omega)$ is the transfer function of the system, i.e. a complex admittance associated with $p(t)$: [2]

$$T_F(\omega) = \frac{\widetilde{p}(\omega)}{\widetilde{F}(\omega)}. \tag{2.23}$$

Here the coordinate of the system X, whose p is the generalized conjugate momentum, is a linear combination weighted by the function $\mathbf{P}(\mathbf{r})$ as in equation (2.13). Under these conditions, according to Levin ([10] and therein [19]), the admittance function T_F must be evaluated

[2] Usually the complex admittance is associated with the (generalized) coordinate $x(t)$ and it is defined as $Y \equiv x/F$, so that the fluctuation-dissipation theorem is written as $S_x(\omega) = 4k_BT\Re[Y(\omega)]$. Instead here we consider the admittance associated with the conjugate coordinate $p(t) = \dot{x}(t) = \imath\omega x(t)$. Then we have $T \equiv p/F = \imath\omega x/F = \imath\omega Y$, hence $\Re[Y] = \Re[-\imath T/\omega] = -\frac{1}{\omega}\Re[\imath T] = -\frac{1}{\omega}\Im[T]$.

as the system response to a force like $F(t)\mathbf{P}(\mathbf{r})$ applied to the test mass surface. But the only force of this kind acting on the test mass is the back action one. The thermal noise power spectral density on the output variable is then given by the transfer function $T_{BA}(\omega)$ like in equation (2.21):

$$\begin{aligned} S_{XX}(\omega, T) &= -\frac{4k_B T}{\omega}\Im\left[T_{BA}(\omega)\right] \\ &= -\frac{4k_B T}{\omega}\sum_n -\frac{\omega_n^2\phi_n(\omega)}{M}\frac{|\int_S dS \quad \mathbf{P}(\mathbf{r})\cdot\mathbf{w}_n(\mathbf{r})|^2}{(\omega_n^2-\omega^2)^2+\omega_n^4\phi_n^2(\omega)} \end{aligned} \tag{2.24}$$

We point out that the thermal noise of the system can be reduced reducing the detector temperature T. The thermal noise depends also on the dissipation ϕ which is a proper characteristic of the material used.

2.7 Standard Quantum Limit (SQL).

Let $S_{xx}(\omega)$ and $S_{ff}(\omega)$ be the equivalent displacement and force single sided Power Spectral Density (PSD), respectively. S_{xx} is the additive noise due directly by the readout; S_{ff} is the noise due to the readout that drives the system through the transfer function T_{BA} (equation 2.20). $S_{xx}(\omega)$ and $S_{ff}(\omega)$ define completely the readout noise properties. In fact under the hypotheses of uncorrelated noise sources, the contribution of the readout to the noise on the observable X is

$$S_{XX}(\omega) = S_{xx}(\omega) + |T_{BA}|^2 S_{ff}(\omega). \tag{2.25}$$

For a continuous linear measurement the uncertainty principle requires that it always is:

$$\sqrt{S_{xx}(\omega)S_{ff}(\omega)} \geq \hbar \tag{2.26}$$

and the readout is called *quantum limited* if this lower limit is achieved. Braginsky and Khalili demonstrated [20] that for each ω the SQL for the detector is achieved if the readout noise contribution is minimized, i.e. if the following equations are both satisfied:

$$\begin{aligned} \sqrt{S_{xx}(\omega)S_{ff}(\omega)} &= \hbar \\ \sqrt{S_{xx}(\omega)/S_{ff}(\omega)} &= |T_{BA}(\omega)| \end{aligned} \tag{2.27}$$

Hence we can equivalently say that if the detector is optimised at the SQL, the following equations must hold:

$$\begin{aligned} S_{xx}(\omega) &= \hbar|T_{BA}(\omega)| \\ S_{ff}(\omega) &= \frac{\hbar}{|T_{BA}(\omega)|} \end{aligned} \tag{2.28}$$

These equations make clear that for the achievement of the best detector performances they are essential

- the use of a quantum limited readout;
- the proper matching between the noise and the test mass mechanical impedance T_{BA}.

Furthermore at the SQL the total displacement noise becomes:

$$S_{XX}(\omega) = 2\hbar|T_{BA}(\omega)|, \tag{2.29}$$

and the equivalent input GW PSD can be written starting from this equation through the GW transfer function $H_{GW}(\omega)$ (equation 2.18) as $S_{hh}(\omega) = S_{XX}(\omega)/|H_{GW}(\omega)|^2$, i.e. the *detector sensitivity* to an incident GW at SQL is

$$S_{hh} = 2\hbar\frac{|T_{BA}|}{|H_{GW}(\omega)|^2} \tag{2.30}$$

Taking into account also the thermal noise (equation (2.24)) the *total detector sensitivity* becomes:

$$S_{hh}(\omega, T) = \frac{2\hbar|T_{BA}(\omega)| - \frac{4k_BT}{\omega}\Im[T_{BA}(\omega)]}{|H_{GW}(\omega)|^2} \tag{2.31}$$

Looking at the expression for thermal noise (eq.(2.24)), we can point out that, in the case of structural damping, the thermal noise contribution to $S_{hh}(\omega, T)$ is proportional to the product $T\phi$. Here the choice of the material for the test mass takes a very crucial role in the optimisation of the detector sensitivity. In principle, the mechanical thermal noise can be reduced below the readout noise lowering the detector temperature T.

2.8 The case of the single mass DUAL detector.

Using the results discussed in the previous section, the SQL sensitivity of the detector can be estimated given a specific configuration, naturally after that the eigenvalues problem (eq.(2.4)) for the test mass is

solved. Recently the case of a single cylinder detector has been studied [10], like in the configuration shown in Figure 2.2 (bottom).

One of the main symmetry axis of the system is the z axis, then cited authors limit the evaluation considering a GW propagating along it. The force exerted by the wave on the test mass does not depend on the coordinate z. The response of the system is then well described by plain strain solutions, where the component of the displacement along z-axis vanishes and the displacement is function only of the coordinates x and y. The analytical plain strain solutions are well known ([10] and therein) and they are used to evaluate the detector sensitivity. FEM simulations are used to confirm the results also outside the plain strain approximation when a real three-dimensional test mass is considered. Cited authors show that this *single* test mass detector offers the same advantages of the previously described two nested mass configuration, i.e. the large bandwidth, imposed by the frequency difference between the lowest order GW sensitive modes, and the back action reduction effect, determined by the anti-resonance frequency placed between these modes.

2.8.1 The selective readout.

To fully accomplish all these DUAL detector properties, cited authors consider to implement a pair of selective readouts. These readouts [9] are sensitive to the two independent components of the quadrupolar modes and reject that classes of modes which are not excited by Gws. The selective readouts $R_{\oplus}$ and $R_{\otimes}$ (Figure 2.4) measure the inner diameters of the hollow cylinder and combine them to obtain $X_{\oplus} = d_2 - d_1$ and $X_{\otimes} = d_4 - d_3$. In each diameter evaluation, the test mass inner surface displacement is averaged over two opposite areas all the cylinder length long.

The weight functions corresponding to this detection scheme are the following:

$$\begin{aligned} \mathbf{P}_{\oplus}(\mathbf{r}) &= \delta(r - r_{int}) P_{\theta}(\theta) \mathbf{i}_r \\ \mathbf{P}_{\otimes}(\mathbf{r}) &= \delta(r - r_{int}) P_{\theta}(\theta + \pi/4) \mathbf{i}_r \end{aligned} \tag{2.32}$$

where

$$P_{\theta} = \frac{1}{S_0} \sum_{m=0}^{1} \sum_{n=0}^{4} (-1)^{n+m} \Theta \left[\theta + (-1)^m \alpha - n\pi/2 \right], \tag{2.33}$$

where $\Theta(x)$ is the unit step function and 2α is the angle subtended under each sensing surface like shown in Fig. 2.2(bottom). In this topology $\alpha = 0.2 rad \quad (\sim 11^{\circ}.5)$ and this is a good compromise between the

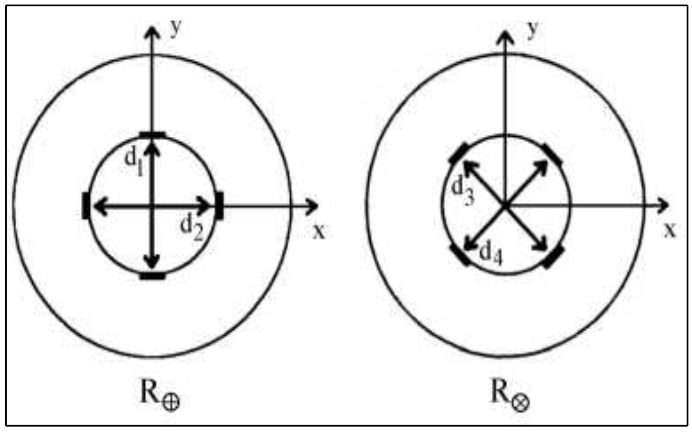

Figure 2.4: Section of the detector showing the details of the readout measurements topology. The measuring surfaces are arranged in two independent readout configurations: the readout $R_\oplus$ measures the difference $X_\oplus = d_2 - d_1$, while $R_\otimes$ does $X_\otimes = d_4 - d_3$. $R_\oplus$ and $R_\otimes$ are sensitive respectively to the + and × components of a GW propagating along the z-axis.

requirements of wide sampling area and the possibility of implementing two selective readouts rotated by $\pi/4$ on the same test mass. The normalization S_0 is the area of each sensing surface ($S_0 \sim 2\alpha r_{int} L$, as shown in Fig. 2.4). The detector sensitivity does not depend on the chosen normalization S_0, according to eq. (2.31).

2.8.2 Plain strain approximation.

Recently analytical solutions to the eigenvalues problem (eq.(2.4) were reported [10] and compared with a numerical solution obtained by FEM analysis. The analytical solutions satisfy the eigenvalues equation in the plain strain approximation whose boundary conditions are:

- the z-component of the displacement field vanishes ($u_z \equiv 0$);
- the first derivative with respect to z of the three components of the displacement field vanishes ($\partial(u_r, u_z, u_\theta)/\partial z \equiv 0$)

This solutions give the plain strain normal modes of the motion of the cylinder in the $x - y$ plane. The plain strain solutions are exact only for an infinite length cylinder. In the case of a finite length cylinder they can be considered exact only if a pressure is applied to the edge surfaces of the cylinder in opposition to the internal stress. According

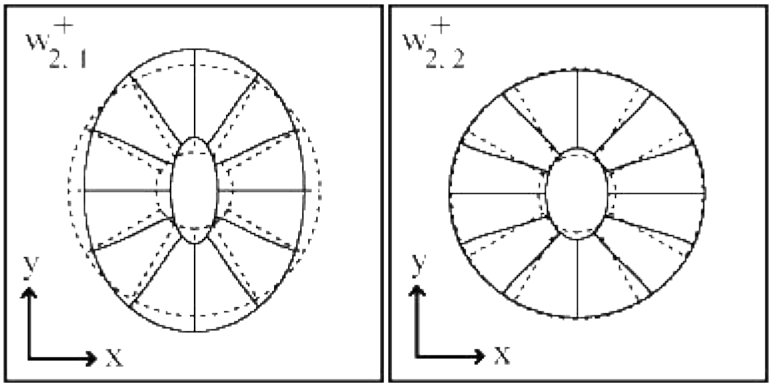

Figure 2.5: **Shape of the first two plain strain quadrupolar modes.** Continuous lines show the deformation of internal and external surfaces and of 12 radial lines ideally traced inside the cylinder section. The shape of the cross section at null deformation is shown with a dashed line. (Left) First quadrupolar mode: both inner and outer surfaces change their shape while the cylinder thickness $r_{ext} - r_{int}$ remains roughly constant (flexural mode). (Right) Second quadrupolar mode: the outer surface essentially does not change. This deformation involves a change of the cylinder thickness (bulk mode).

to the Saint-Venant principle ([10] and therein), the authors infer that the plane strain approximation is satisfactory when the cylinder length is large compared with its diameter. In this case stress and strain inside the body are practically independent of the force distribution on the edge surfaces except for relatively small slices near its ends.

2.8.3 Equivalence between single and dual mass detectors.

In order to point out how single and dual mass detectors can be equivalent, cited authors evaluated the effect on the single resonator of a + polarized GW propagating along the z-axis showing that actually:

- the main contribution to the displacement is given by the first two quadrupolar modes (see Figure 2.5);
- these modes share in deformation with opposite sign;
- for the previous reason, when a GW of frequency ν_{GW} impinges the detector the contribution of the two modes
  - subtracts at low frequencies ($\nu_{GW} < \nu_1, \nu_2$) because they follow in phase the driving gravitational force;

- is enhanced when the GW frequency is between the frequencies of the first two quadrupolar modes ($\nu_1 < \nu_{GW} < \nu_2$) because of the πrad phase lag of the first mode which is driven above its resonant frequency. The frequency range $\nu_1 \div \nu_2$ determines roughly the detector bandwidth;
- subtracts at higher frequencies ($\nu_{GW} > \nu_1, \nu_2$) when both the modes get out of phase because they are driven above their resonant frequency.

In Figure 2.6 the resulting GW transfer function is shown. The two peaks corresponding to the two quadrupolar modes are evident. In Figure 2.6(b) it is shown the back action transfer function T_{BA} evaluated using the readout weight function $\mathbf{P}_{\oplus}(\mathbf{r})$ with $\alpha = 0.2rad$. In the same figure it is also shown the transfer functions resulting from the three dimensional FEM analysis. The 3D FEM evaluation essentially confirmed the resonant modes found in the plain strain approximation but moreover it found other modes that cannot be obtained in the plain strain framework. Thanks to the readout capability of rejecting non GW sensitive modes, the displacement induced by these additional modes is efficiently averaged out and the detector dynamical performances do not differ from that evaluated in the plain strain approximation.

2.8.4 Detector optimization.

A low dissipation material is necessary to enhance the detector sensitivity and to reduce the level of thermal noise. Molybdenum represents an interesting choice because it shows high cross section for GWs and low mechanical losses at low temperature. Duffy [21] reported the value $T\phi < 5 \times 10^{-9}K$ for acoustic modes down to $50mK$.

Defining the *energy resolution* as $\epsilon_0 \equiv \frac{\sqrt{S_{xx}S_{ff}}}{\hbar}$ and the *noise stiffness* as $\kappa_0 \equiv \sqrt{S_{ff}/S_{xx}}$ (both supposed frequency independent), the authors in [10] show that, for the case $r_{int}/r_{ext} = 0.3$ and $\epsilon_0 = 1$ (i.e. SQL conditions), the optimal value of the noise stiffness is $\kappa_0 \simeq 1.7 \times 10^1 1N/m$. [3]

Looking at Figure 2.7 it can be seen that, for the optimal value κ_0, the thermal noise induced by the finite dissipation value $T\phi = 10^{-8}K$ reduces the sensitivity of less than 20%. This choice is a good

[3] Inverting the definitions of noise stiffness and energy resolution we have $S_{xx} = \hbar\epsilon_0/\kappa_0$ and $S_{ff} = \hbar\epsilon_0\kappa_0$. Remembering that the SQL is determined by the *two* equations (2.27), fixed the SQL $\epsilon_0 = 1$, it remains that the noise stiffness must be properly matched to the test mass mechanical impedance T_{BA}.

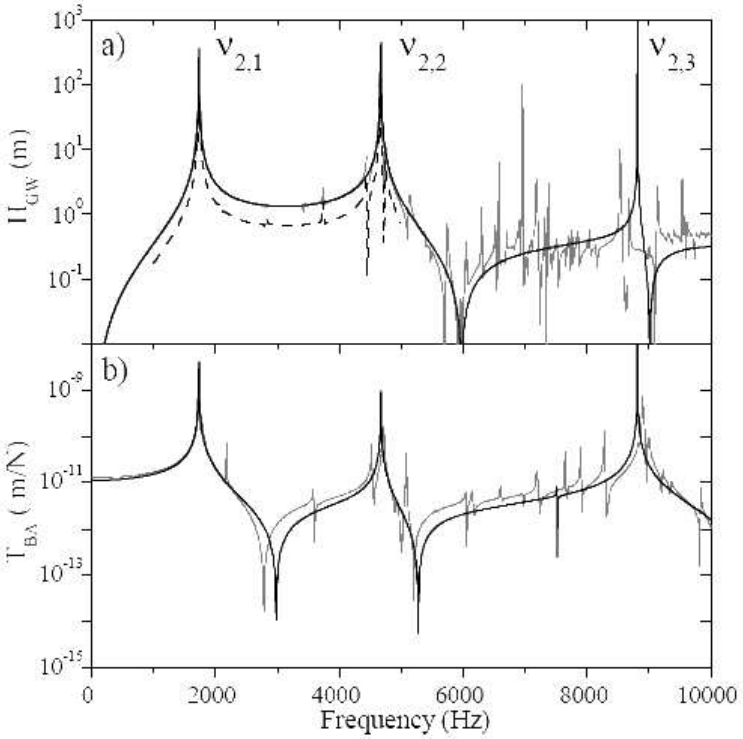

Figure 2.6: The transfer function for the $R_\oplus$ readout with $\alpha = 0.2rad$. The function describes the dynamical response of an hollow cylinder DUAL detector (single mass). Technical data: material molybdenum, outer radius $r_{ext} = 0.5m$, height $L = 3m$, form ratio $r_{int}/r_{ext} = 0.3$. (a) Analytical (continuous line) and FEM (grey line) GW transfer function for a signal propagating along the z-axis. 3D FEM (dashed line) evaluated response under a + polarized GW traveling along the y-axis. (b) Back action transfer function: analytical plain strain evaluation (continuous line) and 3D FEM simulation (grey line).

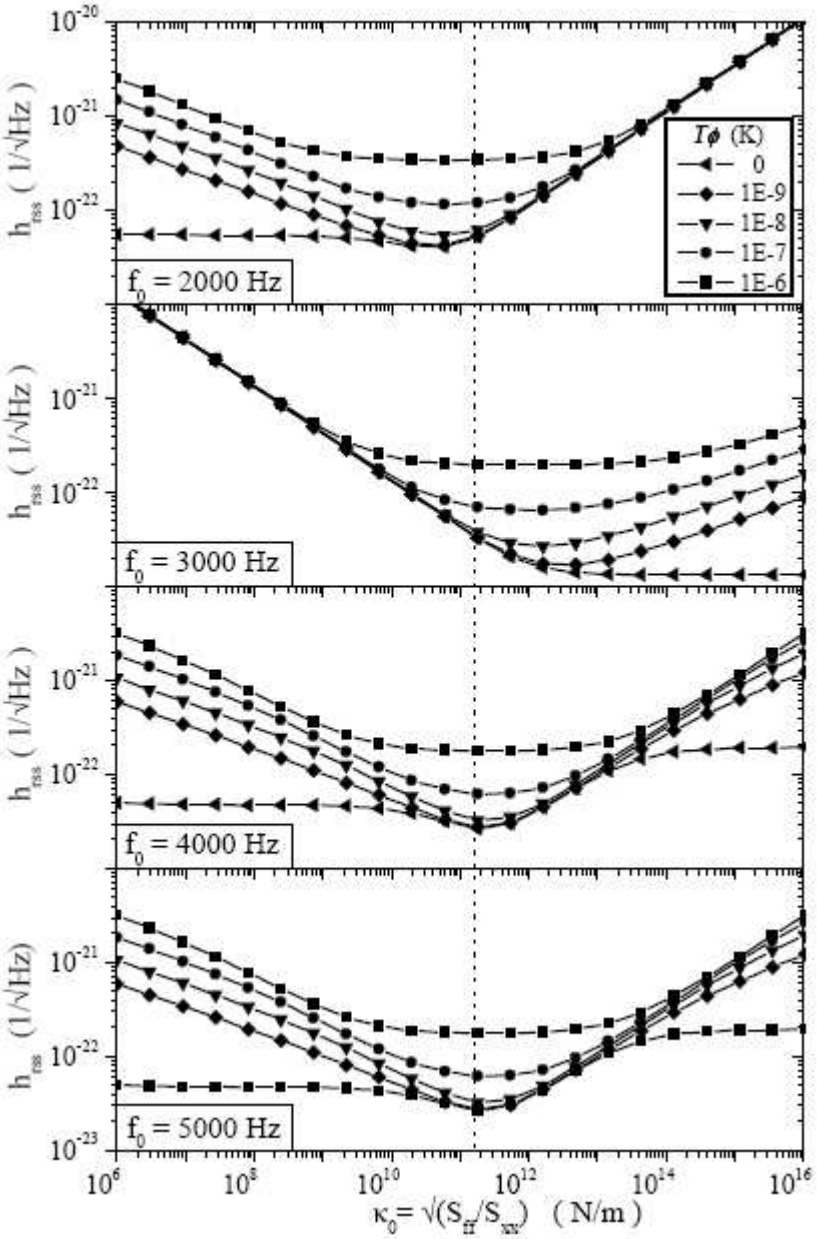

Figure 2.7: Minimum detectable (at SNR=1) root sum square amplitude h_{rss} of a sine-Gaussian test waveform, at 4 different values of the central frequency f_0. The detector form factor is r_{int}/r_{ext}=0.3 and it is equipped with a quantum limit readout ($\epsilon_0 = 1$). The value $\kappa_0 \simeq 1.7 \times 10^{11} N/m$ is indicated by the dot vertical line and gives the best h_{rss} value averaged over the 4 test frequencies. This optimal value for the noise stiffness is independent of the $T\phi$ value and corresponds to a readout displacement power noise of $S_{xx} \simeq 6 \times 10^{-46} m^2/Hz$ and back action force power noise of $S_{ff} \simeq 1.8 \times 10^{-23} N^2/Hz$.

compromise between sensitivity and feasibility and can be assumed as the reference $T\phi$ value for the case $\epsilon_0 = 1$. In general the optimal $T\phi$ value is determined by the readout energy sensitivity ϵ_0. In fact the contribution of the readout to noise is linear in ϵ_0 and it can be found that the value $T\phi < 10^{-8}\epsilon_0 K$ is necessary to limit the thermal noise contribution within the 20% of the readout noise. This reason justifies the loss angle measurements as function of temperature performed in the present work for those candidate materials for which losses are not already measured in literature. On the other hand the optimal value of the noise stiffness κ_0 is mainly determined by the transfer function $T_{BA}(\omega)$ and remains unchanged.

Since the optimization process requires to balance the noise figure, in Figure 2.7 the minimum detectable value of a specific GW signal is evaluated as a function of κ_0. The authors consider the band 2-5 kHz where burst signals are expected form compact stellar objects, hence they consider a sine-Gaussian as test waveform [10]. Furthermore the sensitivity of the detector is evaluated for four different central frequencies of the sine-Gaussian wave. The calculations were also performed as a function of the amount of dissipation ($T\phi$ value) considered in the test mass.

The detector performances were studied as function of the form factor (r_{int}/r_{ext}) at the optimal noise stiffness averaged over the 4 test frequencies and for different values of energy sensitivity (ϵ_0) considered at their corresponding optimal value of dissipation ($T\phi$): the optimization of the noise stiffness was found essentially constant at the value $\kappa_0 \simeq 1.7 \times 10^{11} N/m$. The dependence on the inner radius is not strong but the best sensitivity is obtained for 0.2¡r_{int}/r_{ext}¡0.5. the resonance frequencies of the first two quadrupolar modes are 2 and 5 kHz. The GW sensitivity S_{hh} for this optimized detector (molybdenum, r_{int} = 0.15 m, r_{ext} = 0.5 m, height 3 m) is shown in Figure 2.8.

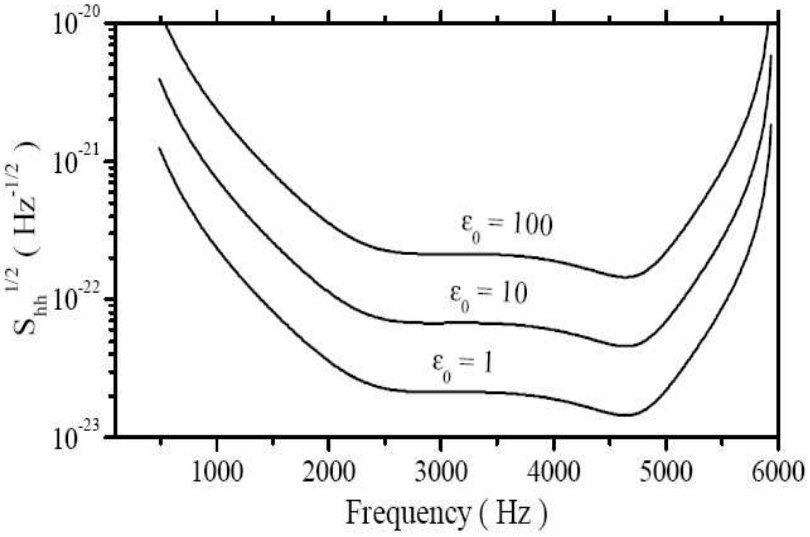

Figure 2.8: Predicted spectral strain sensitivity of the molybdenum DUAL detector: weight 22 ton, outer diameter 1 m, inner diameter 0.3 m and height 3 m. The curves at different values of the readout energy sensitivity ϵ_0 are evaluated with optimal values of noise stiffness $\kappa_0 \simeq 1.7 \times 10^{11} N/m$ and with dissipation $T\phi = 10^{-8}\epsilon_0 K$. The corresponding displacement noise power of the optimal readout is $S_{xx} = 6 \times 10^{-46}\epsilon_0 m^2/Hz$ and back action force power noise of $S_{ff} \simeq 1.8 \times 10^{-23}\epsilon_0 N^2/Hz$. The curve with $\epsilon_0 = 1$ represents the DUAL detector at SQL.

Bibliography

Bibliography for Chapter 1.

[1] L.Baggio *et al.*, *3-Mode Detection for Widening the Bandwidth of Resonant Gravitational Wave Detectors*, Physical Review Letters, **94**, 241101 (2005).

[2] Z.A. Allen *et al.*, Physical Review Letters, **85**, 5046 (2000).

[3] P. Astone *et al.*, Physical Review D **68**, 022001, (2003)

[4] L.Baggio *et al.*, *3-Mode detection for widening the bandwidth of resonant gravitational wave detectors*, Physical Review Letters, 2005

[5] M. Cerdonio *et al.*, Physical Review Letters, **87**, 031101 (2001)

[6] T. Briant, M. Cerdonio *et al.*, Physical Review D **67**, 102005 (2003)

[7] M. Bonaldi, M. Cerdonio *et al.*, Physical Review D **68**, 102004 (2003)

[8] M. Cerdonio, L. Conti, J.A. Lobo, A. Ortolan, L. Taffarello and J.P. Zendri, Phys. Rev. Lett. **87** 031101 (2001)

[9] M. Bonaldi, M. Cerdonio, L. Conti, M. Pinard, G.A. Prodi, L. Taffarello and J.P.Zendri, Phys. Rev. D **68** 102004 (2003)

[10] Bonaldi *et al.*, *Principles of wide bandwidth acoustic detectors and the single-mass DUAL detector*,Phys. Rev. D 74 (2006) 022003 1

[11] M.Bignotto *et al.*, *Dual detectors of gravitational waves*, Proceedings of Astronomical Telescopes and Instrumentation , 21-25 June 2004, Glasgow, Scotland, Proceedings of SPIE – Volume 5500 Gravitational Wave and Particle Astrophysics Detectors, J. Hough, G. H. Sanders, Editors, September 2004, pp. 105-112

[12] Article in preparation.

[13] T. Briant, M. Cerdonio, L. Conti, A. Heidmann, A. Lobo, M. Pinard, Phys. Rev. D 67, 102005 (2003).

[14] Landau, Lifshitz, *Theory of elasticity*, Pergamon Press.

[15] P.R.Saulson, Physical Review D **42**, 2437 (1990)

[16] K. Yamamoto *et al.*, Physics Letters A **321**, 79 (2004)

[17] C.W.Misner, K.S.Thorne, J.A.Wheeler, *Gravitation*, W.H.Freeman and Company, S. Francisco, 1973.

[18] H.B.Callen and T.A.Welton, Physical review D **83**, 34 (1951)

[19] Yu.Levin, Physical Review D, Vol.57, No.2, 659 (1998)

[20] V.B.Braginsky and F.Ya.Khalili, *Quantum Measurement*, Cambridge University Press, Cambridge, 1992.

[21] W.Duffy Jr., Journal of Applied Physics, **72**, 5628 (1992)

Chapter 3

The Ultra-Cryogenic Test Facility.

3.1 Introduction.

In origin the Ultra-Cryogenic Transducer Test Facility was designed in order to test the whole capacitive readout of the AURIGA detector (i.e. capacitive transducer + double stage SQUID amplifier + resonating LC matching line) in the same environment as it will be operating in the main detector. Using this facility, AURIGA collaboration performed the first thermal noise measurement of the complete readout In Figure 3.1 a section of the facility is shown. Recently, within the work of this PhD Thesis, this Test Facility (TF) was upgraded to measure the loss angle of materials within the Research and Develop (R&D) DUAL detector project. The strong points of the TF are its high versatility and very short thermalization time. In fact, with its $\sim$0.04m^3 volume and $\sim$50 kg payload, it allows to measure several samples in the same cryogenic (or ultra-cryogenic) run. The whole site is provided for complete outfit to assemble samples in their holders and to mount them in the experimental room for cryogenic measurements. A clean room (class 10000) belongs to the facility and all samples are made ready for measurements inside it. A pair of days is the time needed to cool down – to 4K or lower – the whole mass (structures + samples).

The TF is equipped with a dilution refrigerator and a temperature controller (Lake Shore 340TC) so that the available temperature range is $\sim$0.02$\div$300 K ($\sim$0.02$\div$3 K using the dilution refrigerator + heater, $\sim$3$\div$70 K using liquid helium bath + heater, $\sim$70$\div$300 using liquid nitrogen bath + heater). Liquid helium consumption is limited to about 22 liters per day (at 4K and with heater off). A chain of cryogenic mechanical suspensions damps the seismic noise allowing

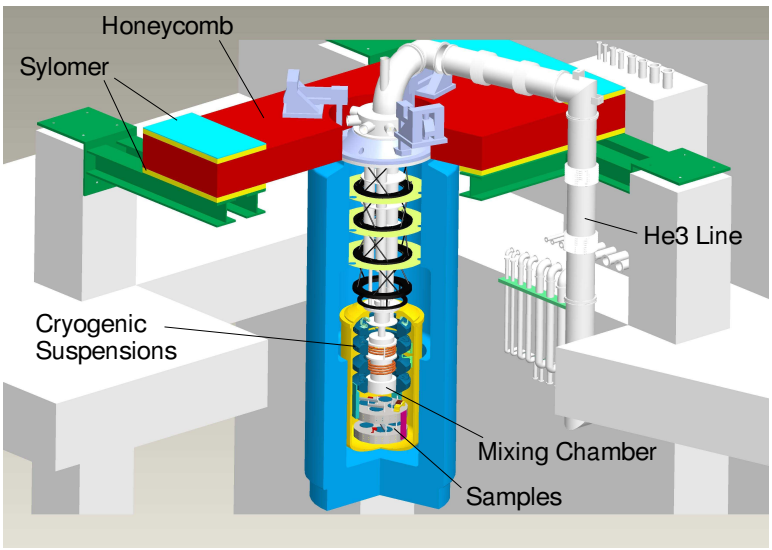

Figure 3.1: **Section of the ultra cryogenic Test Facility (TF).** It is located inside the same AURIGA building at Legnaro National Laboratories (LNL), INFN (Padova, Italy). Four H-shaped steel beams are supported by four reinforced pillars. On the beams a plane with an Al honeycomb structure is placed. Three cantilever arms — providing an attenuation of 20 dB at 1 kHz — hold the outer flange which closes the Dewar. The pumping lines, the cryogenic refilling conduits, the electronic wiring and the dilution refrigerator pipes pass all through this flange which is furthermore provided by an optical window. A light and torsionally rigid structure holds the Internal Vacuum Chamber (IVC). Inside IVC cryogenic suspensions are housed. The higher suspension spring is made of stainless steel to reduce the thermal leak toward the ^4He bath. All the others springs are made of *Ergal 7075* — a high strength Al alloy —. The base holding samples is thermally linked to the cold plate of the dilution refrigerator by a soft connection consisting of annealed OFHC Cu strips (courtesy of M.Bignotto).

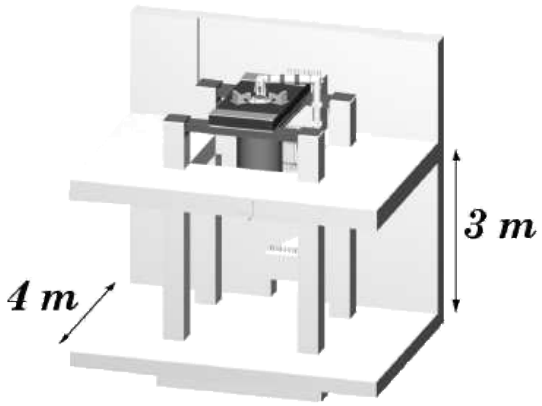

Figure 3.2: A section of the carrying structure housing the TF. The four cement pillars are supports for the lift which moves the Dewar vessel up and down.

sensitive measurements up to the thermal noise level of a high quality factor (exceeding 10^6) mechanical oscillator at low temperature.

3.2 Brief description.

The TF is located inside the same main AURIGA detector building at the INFN Legnaro National Laboratories (LNL) near Padova, Italy. It is arranged along two floors. The weight of the entire facility is hold by a light structure built on top of four reinforced pillars (see the Figure 3.2). The top support is made of four H-shaped beams on which an aluminium honeycomb layer is laid. Between the honeycomb and the beams a layer of Sylomer© is placed. It was chosen for its anti-vibrating properties in the softest G25 yellow type. The honeycomb is 20 cm high and soft enough to have no resonance with quality factor of more than 10^3 above few Hz. In the honeycomb centre a 60 cm diameter hole was dug in order to allow the insertion of the dilution refrigerator pipe connections, cryogenic refilling conduits and electronic wiring.

3.2.1 The top flange at room temperature.

Three L-shaped rods represent the first, room temperature part of the suspensions. They hold the top flange that closes the Dewar and holds the refrigerator. These rods are provided for holding screws which

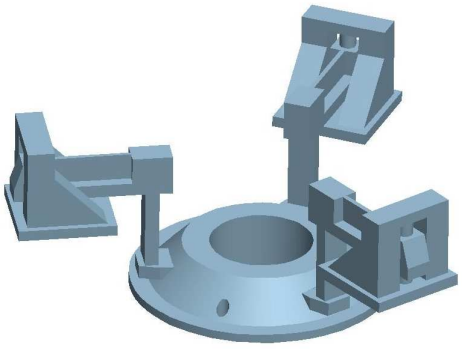

Figure 3.3: **Room temperature TF top flange.** The arms are 120 degrees apart each from other and are fixed with M12 screws to the bottom part of the flange. This flange supports the weight of the whole structure. It was FEM designed to avoid spurious frequencies around 1 kHz.

allow to adjust and set horizontally the top flange. The three rods are identical and their shape is analyzed with Finite Element Method (FEM) to avoid any possible resonance frequency in the band 500 ÷ 1500 Hz. [1] Moreover these rods provides for the first damping stage, being shaped to have the first resonance around few hundred Hz and nothing else up to above 2 kHz. Modal analysis had been successfully performed simulating the load of the room temperature flange to which the rods are attached, showing a -20 dB attenuation [2]. The rods are in stainless steel AISI 316. In Figure 3.3 the room temperature top flange is shown in detail.

The room temperature flange is the connection between the Dewar neck and the refrigerator top flange. Its design was performed considering the constraints deriving originally from the AURIGA transducer thermal noise measurement: to avoid the introduction of spurious resonant modes in the transducer frequency range around 1 kHz. Even though simple in principle, the shape of the flange is carefully adjusted to fit a lot of other parts of the facility. For example it has slots to screw in the external rods, holes for all pipes and wires going toward the IVC and the cryogenic bath, slots to fasten the internal suspension structure, and so on. The real design of this flange is so complex that it was possible to simulate with FEM only a slightly different one. Anyway even on simplified pieces, simulations gave coherent results both with and without features like holes or small slots.

[1] Because in principle the TF was designed to measure the thermal noise of the AURIGA detector readout whose resonant frequency is just about 1 kHz.

Figure 3.4: **Lattice structure.** The TF lattice structure is formed by four stages with cylindrical symmetry. Each stage holds a thermal radiation shield, not shown in the picture.

3.2.2 The lattice.

Looking inside the Dewar (figure 3.1 and 3.4 in more detail), it is shown a light and torsionally rigid structure which is attached to the inferior face of the flange. Its material is stainless steel AISI L 304. The structure holds the IVC and all of the experimental setup and provides for a load bypass for the dilution refrigerator. It was designed with one more function: it serves as a thermal decupling system, being equipped with thermal shields to minimize the radiative thermal input from the room temperature to the liquid He bath inside the Dewar. Moreover, in order to reduce the thermal conduction, the section of the pipes forming this structure is as small as possible. Calculations — considering only metallic thermal conduction — showed that the expected liquid He evaporation rate is about 0.5 l/hour [3]. The observed rate is slightly larger, 0.9 l/hour at 4K with heater off.

3.2.3 The intermediate IVC flange.

The IVC is attached to an intermediate flange which provides both vacuum tightness and rigid suspensions. This flange was designed with ProEngineer© and underwent many modal analyses with ProMechanica© to make sure that its shape was not introducing spurious resonances. The IVC provides an high vacuum environment ($P \lesssim 10^{-6}$ mbar). From a mechanical point of view, this is particularly useful for exam-

ple in loss angle measurements: in fact the capacitive displacement sensor gap is usually very thin ($\lesssim 100\mu$m) and so the gas damping inside the gap can be considerable. Measurements performed in TF show that gas damping affects significatively the loss angle measurement when $P \gtrsim 5 \times 10^{-5} mbar$ on about 100 μm gap. A good vacuum also reduces the thermal link between the samples and the IVC walls; it allows cooling samples below 100 mK even if the IVC walls are at 4.2 K in equilibrium with the liquid helium bath.

3.2.4 The Internal Vacuum Chamber.

The core of the apparatus is the *Internal Vacuum Chamber* (IVC). A vertical section of the IVC is shown in Figure 3.5. It houses the cryogenic mechanical suspensions and all the samples to be measured. There is room to arrange one or more basements each with one or more samples housed on. In the suspensions design phase, a specific FEM software was applied to perform the modal analysis. The overall dimension was designed to be as wide as possible, consistently with the 500 mm diameter of the aperture, and without introducing spurious resonances. For this reason, a thin shell was the design starting point, but subsequent simulations showed that there was no mean to push up the shell resonances without relying on a very thick and heavy structure. So a lighter structure was chosen (10 mm thick and 150 kg heavy) but the shell was provided with threaded holes to place load masses in order to move possible unwanted resonances out of the frequency band of interest.

3.2.5 C steel springs.

Moving inside the IVC, the first elements we find are three C-shaped steel springs, clamped on the one side to the IVC upper flange internal face and on the other side to the first internal suspension stage. These springs are the first effective isolation from the mechanical environmental noise. Their design matched the strength and rigidity requirements coming to a compromise between a light structure, needed to keep the frequencies low enough, and a heavier one necessary to support high stresses and to avoid risks of breaking. The material chosen was stainless steel AISI L 316. The goal attenuation was -30 dB. The first six normal modes are all below 160 Hz and no further modes are measured below 2 kHz.

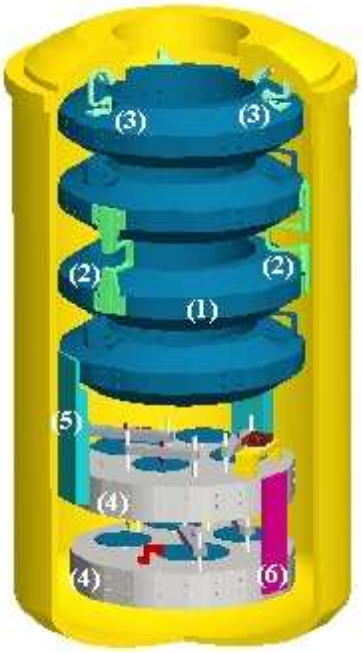

Figure 3.5: **A section of the Internal Vacuum Chamber (IVC)**. The dilution refrigerator is inside the mechanical suspensions. On the bottom there is the payload. The samples under test are mounted with their holders on two floors. A PID controller drives the heater line, doing feedback on the thermometer placed on border side of one of the floors. For much more details about the sample arrangement on basements, see also the following figure 3.7. (1) The cryogenic suspension. (2) "*Omega*" springs. (3) *C* steel springs. (4) Two parallel basement floors on which the samples holders are screwed on. (5) Aluminium hanger. (6) OFHC copper hanger.

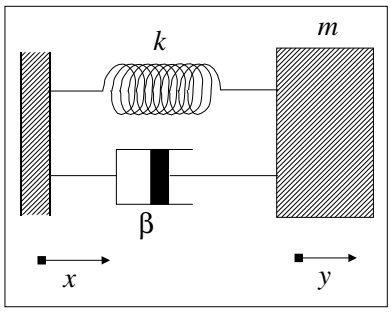

Figure 3.6: A simplified scheme of the seismic and acoustic noise effects on a mass m to be suspended. This is the basic scheme from which the TF cryogenic suspensions work.

3.2.6 Cryogenic suspensions.

The cryogenic suspensions were designed in origin when the main purpose of the TF was the measurement of the thermal noise for mechanical transducers. In fact, to lower the seismic and acoustic noise is indispensable to measure the transducer thermal noise successfully, as well known.

The typical way to attenuate the ambient noise is to insert a spring between the mass to be suspended and the holder where it is clamped (see Figure 3.6). Let x be the holder displacement and y the mass one. The equation of motion is the following:

$$m\ddot{y} + \beta(\dot{y} - \dot{x}) + k(\dot{y} - \dot{x}) = 0 \tag{3.1}$$

or in frequency domain

$$-m\omega^2\tilde{y} + \imath\beta\omega(\tilde{y} - \tilde{x}) + k(\tilde{y} - \tilde{x}) = 0 \tag{3.2}$$

where $\tilde{x}(\omega) = \int x(t)e^{\imath\omega t}dt$ and $\widetilde{F}(\omega) = \int F(t)e^{\imath\omega t}dt$ are the Fourier transform of $x(t)$ and $F(t)$ respectively. From the last equation it follows immediately that:

$$\frac{\tilde{y}}{\tilde{x}} = \frac{\omega_0^2 + \imath\frac{\omega\omega_0}{Q}}{\omega_0^2 - \omega^2 + \imath\frac{\omega\omega_0}{Q}}, \tag{3.3}$$

where $\omega_0 = \sqrt{k/m}$. The equation (3.3) is just the *transfer function* of the system. It describes the mass displacement $\tilde{y}$ as a function of the support displacement $\tilde{x}$, for instance due to the seismic noise. The

modulus of the transfer function is

$$\left|\frac{\tilde{y}}{\tilde{x}}\right| = \sqrt{\frac{\omega_0^4 + \left(\frac{\omega_0\omega}{Q}\right)^2}{\left(\omega_0^2 - \omega^2\right)^2 + \left(\frac{\omega_0\omega}{Q}\right)^2}} \tag{3.4}$$

If the system is in the condition that $\omega_0 \ll \omega$ and $\beta/m \ll \omega_0$ than the equation 3.4 becomes

$$\left|\frac{\tilde{y}}{\tilde{x}}\right| \simeq \left(\frac{\omega_0}{\omega}\right)^2. \tag{3.5}$$

According to the equation 3.5, given the noise displacement $\tilde{x}$ (due to the acoustic and seismic noise) and for all the frequencies much higher than ω_0, the mass displacement $\tilde{y}$ is highly suppressed.

The main suspension system is based on four spring-mass sub-stages placed in cascade one after the other. The overall attenuation is -150 dB. The whole system is divided into two mass-spring-mass monolithic stages connected by *Omega* springs. [2] The transfer function of the various stages was measured in vacuum at room temperature using piezoelectric actuators to excite the suspensions and accelerometers to measure the acceleration before and after each attenuation stage. All measurements show good agreement with the prediction of the FEM model [2].

3.2.7 Experimental setup.

Finally three OFHC Cu stirrups carry the basement with the samples. More than one basement can be placed in cascade one after the other, each carried by its three Cu stirrups. Basements are in Al 5056. The high conductivity copper assures a good thermal link between the two basements. Each one is equipped with threaded holes to screw the samples holders on. Samples can be arranged on two floors; for each basement holders can be screwed both on top and bottom surface. For some detail see the Figure 3.7 and the following picture in Figure 3.8. One rectangular piezoelectric actuator is fixed horizontally to the basement. A 330 gr brass mass is glued on its top to increase its efficiency as force actuator. The piezoelectric ceramic is driven by a high voltage monochromatic signal and it is used to excite normal modes of samples at their proper resonance frequency.

In order to perform measurements at different temperatures, three heater spools are screwed to the edge of the basements, on OFHC rods

[2] The name is due to the characteristic shape of these springs.

connecting the two. They are placed 120 degrees each from other. The heaters are the actuators of a temperature controller (TC) feedback loop that adjusts the current on them by a PID control until the temperature read on the basement thermometer ((5) in Figure 3.7) reaches the value set by user.

3.2.8 The cryostat.

The cryostat is a 800 litres PCS Dewar vessel [3] moving vertically up and down by an elevator (see Figure 3.2). In this way it is possible to arrange the experimental set-up directly in its final position, moving only later the Dewar up and closing it on the flange. This keeps samples clear of the dangerous and useless vibrations due to the elevator movement.

3.3 The dilution refrigerator.

The TF allows for thermal noise measurements at ultra-cryogenic temperature. The necessary cooling power is provided by a 3 mW @ 110 mK dilution refrigerator build by Leiden Cryogenics. [4] The dilution refrigerator extends as far as the height of the apparatus, gets in the IVC and ends just before the basement with the samples. See Figure 3.1 for a sketching view of the whole IVC with the mixing chamber inside. The TF refrigerator was never used for the measurements collected in the current thesis, therefore we will just describe it briefly in principle.

A dilution refrigerator works thanks to the different enthalpy power of two different isotopes of Helium (^{4}He and ^{3}He) in the liquid phase. They show different quantistic properties because ^{4}He is a boson while ^{3}He is a fermion [3]. These two phases don't mix completely (the 6.5% of diluted ^{3}He saturates the ^{4}He phase). It is possible to circulate ^{3}He in the ^{3}He–^{4}He mixed phase, separate it cooling the system and use it again to maintain the cycle. In Figure 3.9 the dilution refrigerator of the TF is shown. In Figure 3.10 a schematic view of the working principle is reported.

The ^{3}He is pumped from the still and filtered through the nitrogen traps where helium is purified from possible traces of other gases. Before entering in the 1K pot, it is cooled by a liquid ^{4}He bath and liquefies in a condenser. After passing through an impedance, it reaches

[3] Precision Cryogenic System, Inc., 7804 Rockville Road, Indianapolis, Indiana 46214, USA

[4] Leiden Cryogenics, Galgewater no.21, 2311 VZ Leiden, The Netherlands.

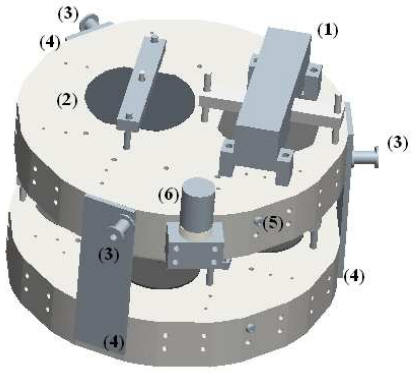

Figure 3.7: **Samples arrangement on two floors.** The drawing shows realistically the samples clamped in their holders and screwed on two basement floors. Even though not shown in the picture, it is possible to arrange samples also on bottom surfaces. In fact, each basement is provided with the same pattern of threaded holes on both top and bottom surfaces. In this case the figure shows a particular arrangement choice with two silicon samples on first and three (partially in sight) silicon carbide disks on second floor. (1) Silicon wafer clamped with nodal suspension described in Chapter 4. The holder houses the large sensitive area "comb" capacitive readout described in Chapter 3. (2) Silicon wafer clamped with nodal suspension and arranged for optical lever readout. The laser beam hits on plate border by the basement centre. The sample is oriented in such the way that laser beam hits where oscillation amplitude is widest for the modes of interest. (3) Three heater spools are placed about 120 degrees each from other. A plait of three, equal length manganine wires is rolled up on each spool and fixed by high conductivity silver glue. The three spools are then connected in series by copper wires with brass screw clamps. The temperature controller (TC) is set to the total resistance of the heater line and it automatically adjusts the current to fit the maximum power as set by user. (4) Three OFHC copper stirrups connect the two basements. The three heater elements (3) are screwed on them to assure a good thermal link. (5) Silicon diode thermometer used by the TC for PID feedback. The basement temperature is controlled and stabilized using this thermometer. In order to make sure that measurements are made under thermal equilibrium conditions, it is possible to acquire the temperatures via GPIB LakeShore© TC 340. A multiplex channel allows to switch between the thermometers. (6) A rectangular piezoelectric actuator (PZT) is fixed to the basement. It is glued horizontally between a lower ceramic disk and an higher brass mass of ∼330 gr, in order to increase its efficiency as force actuator.

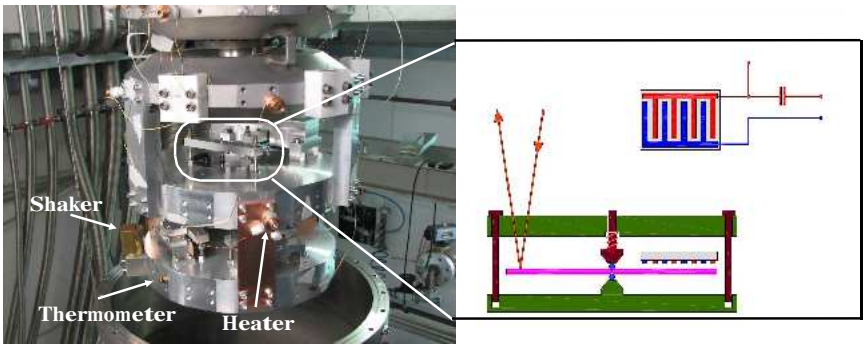

Figure 3.8: **Experimental setup in a picture.** The picture shows the typical experimental setup for loss angle cryogenic measurements in TF. They are labeled some of the components described in the previous Figure 3.7. The samples are arranged on two floors. The upper central place is dedicated to optical lever readout. The setup is provided with three heater spoils driven by a temperature controller; a set of several thermometers to monitor the temperature in different points of the setup; a piezoelectric shaker driven by a monochromatic high voltage signal, used to excite the normal modes of the samples at their proper resonant frequency. This picture shows to the particular sample arrangement adopted for the cryogenic RUN5, nevertheless several are the possibilities to arrange different samples in the TF experimental setup.

Figure 3.9: A view of the TF dilution refrigerator. It spreads through all the TF length: it passes through the honeycomb, the Dewar and the IVC flanges, the radiation shields and the cryogenic suspensions.

the STILL, a vessel where the liquid He is cooled down to about 0.7 K. In the heater exchangers the temperature drops to 100 mK and finally the two phases (^{4}He concentrated and ^{3}He diluted) mixes in the mixing chamber.

The osmosis pressure induced by the pump allows the return path for ^{3}He. Passing through the heater exchangers, the cold liquid ^{3}He gives heat to the hotter ^{3}He coming from the STILL and going to the mixing chamber. The cold liquid ^{3}He evaporates and then the cycle starts again.

3.4 Pumps and thermometers.

The IVC vacuum line is equipped with a molecular turbo pump whose outlet is pumped by a scroll pump. Two manual valves (before and after the turbo pump) allows to isolate the IVC vacuum from pumping or to insert He gas to speed the cooling.

The Dewar bath line is equipped with a membrane oil free pump that allows to pump over the bath and to cool the system (IVC included) few degrees down with respect to the temperature of the cryogenic bath at atmospheric pressure. In the case of He bath, with this

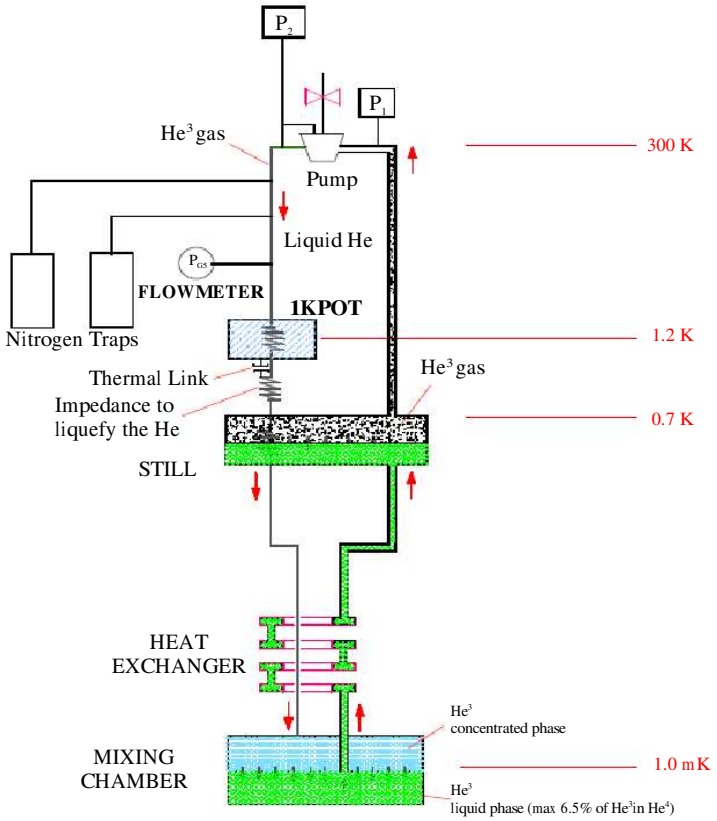

Figure 3.10: Sketching view of a dilution refrigerator operation. Following the ^{3}He path, the ^{3}He gas coming from a still enters in a 1K pot where it cools down and liquefies. Then it passes through the impedance where it cools down again due to the upcoming ^{3}He which takes heat away in the heat exchangers. Afterwards the cooled ^{3}He comes into the mixing chamber. After the mixing, it goes upstream becoming the refrigerant liquid for the ^{3}He coming into the heat exchangers. Once in the STILL, it begins to boil and evaporate. Its flux is removed by the pump and the cycle starts again.

method it is possible to cool the IVC down to about 1.5 K. In the case of LN2 bath, the lowest temperature is about 65 K. Using a proportional valve with a PID controller, it is possible to reach and keep the desired pressure relative to the desired temperature according with the equation of state of the used refrigerator liquid [3]. In the normal 4.2 K operation the dewar is connected to the laboratory He gas recovering system. Under this condition the He evaporation rate is about 0.9 litres/hour.

Also the 1K pot vacuum line is equipped with a piston oil free pump, which allows the filling through two impedances (which can be fine tuned) from the Dewar liquid He bath. A capacitive level meter, read by a capacitive bridge, allows to know the level of the He inside the 1K pot.

The ^{3}He line is sealed and it is equipped with three mechanical pumps, a rotative pump and two roots pumps. This equipment allows to have a ^{3}He flow of about 1 mmol/sec at pressure below 1 mbar.

There are two condensation lines, one with high and the other with low impedance, in order to have more flexibility in the dilution refrigerator operations. The low impedance line can be used to cool down the system quickly, while the high impedance line is used to finely find the optimal operation point.

The IVC is equipped with a temperature PID controller (LakeShore© Model 340TC). The heater resistance consists in three manganine resistive coils connected in series and fixed on the basement with screws. A LakeShore© CERNOX thermometer is placed near one coil; the controller reads it, feedbacks on the coils and maintains the desired temperature. This equipment, together with pumping on cryogenic bath if necessary, allows $\sim 1.5 \div 75$ K temperature range with an external He bath and $\sim 65 \div 300$ K with a LN2 one. In the present set-up the TF is equipped with two basements to hold the samples connected with OFHC copper stirrups. Each basement is equipped with a CERNOX thermometer and the entire set-up allows to measure several samples within the same cryogenic run.

The TF refrigerator is equipped with several thermometers to measure the temperature in different parts of the apparatus. They are placed on the 1K pot, on the STILL, on the mixing chamber, and also on the outer shell of the IVC, one just above and one just below the flange.

Just after installation, the dilution refrigerator was operated with no thermal load and reached a temperature of approximately 15 mK, with a measured cooling power of about 1 mW at 100 mK, well above the estimated thermal leaks at the same temperature [2].

Bibliography

Bibliography for Chapter 3.

[1] M.Bignotto, *La test facility ultracriogenica per trasduttori di spostamento: sospensioni meccaniche e refrigeratore a diluizione* $He^3 - He^4$, Laurea Theses, 1999, University of Padova, Italy.

[2] A.Marin, *Elettromechanical readout for the second run of the gravitational wave detector AURIGA*, PhD Thesis (2002), Padova University.

[3] G.K.White, *Experimental techniques in low-temperature physics*, third edition, Clarredon Press Oxford Science Publications, Oxford (1979)

Chapter 4

A capacitive displacement sensor for dielectrics.

4.1 Introduction.

Usually the measurement of the loss angle is made using the ring down method, which experimentally consists in the acquisition of the exponential amplitude decay of a previously excited normal mode of the sample. Displacement sensors are therefore needed in order to convert the sample displacement in an electrical signal. In continuity with the long AURIGA collaboration's experience in capacitive transducers, we carry out a capacitive displacement sensor to be employed to measure the loss angle with the ring down method. Capacitive readout is fulfilled making a plane capacitor whose the ground plate is the sample itself. This works if the sample is an electric conductor like for example Aluminium or some polytypes of Silicon Carbide, but both conductors and dielectrics (like for example Silicon) appear as possible candidates in carrying out the DUAL sensitive test mass. In order to carry out displacement readout for not conductive materials, we implemented a specific comb capacitor. In such kind of measurements, capacitive readout offers some advantages, for example it is easy to assemble in the IVC, it offers the possibility to measure several samples within the same cryogenic run and the fact that, being passive, it does not heat the sample.

4.2 The sensor.

The sensitive element of the readout consists in a periodic sequence of strips at alternate potentials. The strips form a metallic array of plane electrodes having the form of a bar code and deposited on a dielec-

tric substrate. Because of this geometrical configuration, sometimes in literature the device takes the name of "multistrip" sensor. The working principle is simple. The sample is a dielectric with a plane (and usually in practice also smoothed, of low roughness) surface, which is placed in front of the multistrip sensor, being careful to put sample and multistrip planes as parallel as possible. In the measurement scheme adopted throughout the followings, the gap between the sample and the sensor determines the capacity of the device, so that a variation in the gap induces a variation in the sensor capacity, i.e. a voltage signal on the electrodes.

Therefore, the problem is to find the capacity of the sensor as a function of the gap. Following *Grasso et al.* [1, and therein], we will apply the method of images to solve the problem, being interested in developing the comb capacitor as a displacement sensor. At first we will determine the capacity of a pair of strips in the free space. Then we will use the method of the images to determine the capacity in presence of a dielectric substrate and after in presence of a dielectric sample as a function of the gap. Finally, the whole device consisting of n identical pairs of strips connected in parallel and neglecting border effects, the total capacity will be calculated as n times the capacity of the single pair of strips.

4.3 A pair of identical electrodes in free space.

Let us consider two identical, rectangular shaped and of negligible thickness electrodes, placed side by side on the (y, z) plane of a fixed reference system symmetrically with respect to the origin. Let their longitudinal axes be parallel to the z-axis and transversal ones coincident with y-axis (see Figure 4.1). The distance between longitudinal axes is b. Let be L and a the length and the width, respectively, of both electrodes. The edges of the electrodes intersect the y-axis in the points $A, \ldots, D$ with abscissa

$$y_A = -\frac{b+a}{2}, \quad y_B = \frac{a-b}{2}, \quad y_C = \frac{b-a}{2}, \quad y_D = \frac{b+a}{2} \tag{4.1}$$

Let the potential on the electrodes be fixed and constant to $\pm V_0$, i.e. the electrodes has equal and opposite charge. Let $P(\vec{r}) = (x, y, z)$ be the point in the free space where the potential has to be calculated. The infinitesimal surface element dS contains the electrostatic charge $dQ = \rho(\vec{r}')dS$, where $\rho(\vec{r}')$ is the surface charge density in $\vec{r}' = (0, y', z')$ on a reference electrode with total charge $\pm Q$ and extending from $z \in [-L/2, L/2]$ and $y \in [y_A, y_B] \cup [y_C, y_D]$. The potential $dV(\vec{r})$ at the

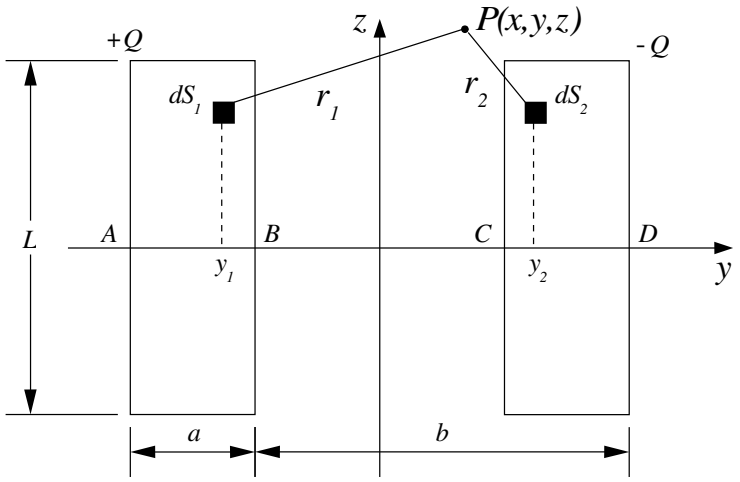

Figure 4.1: A pair of strips in free space. The two metallic electrodes are identically L height and a width and negligible thickness. With respect to the origin, they are symmetrically placed in the fixed reference system (y, z) shown in the figure. The x-axis, not shown, ideally comes out of the sheet towards the reader. The two electrodes have equal but opposite charge $\pm Q$. P is a point in the free space. $dS_{1,2}$ are two surface elements and $r_{1,2}$ are their distances from P, respectively.

point $P(\vec{r})$ due to the charge in the surface element dS is

$$dV(\vec{r}) = \frac{1}{4\pi\varepsilon_0}\rho(\vec{r}')G_{fs}(\vec{r};\vec{r}')dS, \tag{4.2}$$

where ε_0 is the dielectric permittivity of vacuum and the function

$$G_{fs}(\vec{r};\vec{r}') \equiv \frac{1}{|\vec{r}-\vec{r}'|} = \frac{1}{\sqrt{x^2+(y-y')^2+(z-z')^2}} \tag{4.3}$$

is the reciprocal of the distance between P and dS. The latter expression in the previous equation (4.3) makes the function G_{fs} explicit in terms of coordinates within the reference system chosen and shown in Figure 4.1.

The electrostatic potential at the point $P(\vec{r})$ in free space generated by the total charge on the electrodes can be obtained integrating overall the electrodes surface S whose topology is well known and fixed first of all:

$$V(\vec{r}) = \frac{1}{4\pi\varepsilon_0}\int_S \rho(\vec{r}')G_{fs}(\vec{r};\vec{r}')d\vec{r}'. \tag{4.4}$$

The (4.4) is an integral equation where the unknown is the charge density function ρ. An analytical solution of the equation (4.4) is not known neither in the simplest cases. On the other hand, the boundary condition that the potential on the electrodes is fixed to $\pm V_0$ value allows to invert the equation (4.4) by numerical methods to estimate the value of the unknown function $\rho(\vec{r})$ over the electrodes surface. In this way, the charge density can be reconstructed numerically point by point.

At this stage, the capacity of the device can be calculated again integrating numerically the obtained charge density ρ over the surface of the electrodes as:

$$C = \frac{1}{V_0}\int_S \rho(\vec{r}')d\vec{r}' \tag{4.5}$$

Since the whole device consists of N identical metallic strips, neglecting the border effects, [1] the total capacity can be calculated as $N/2$ times the capacity of the single pair of strips at opposite potential, i.e. $C_{tot} = N/2 \times C$.

[1] The more relevant border effects are on the end of the array, where the lines of electric field spreads. Compared to this, the border effect between the electrodes inside the array is negligible, since the presence of the dielectric sample with a short gap prevents the field lines from spreading out.

4.4 A pair of electrodes on a dielectric substrate.

In order to realistically describe the strip sensor, we have to consider the presence of the dielectric substrate of thickness h supporting the metallic strips. Following the cited work of *Grasso et al.*[1], in this case the potential has to be calculated again like in the equation (4.4) but substituting the function G_{fs}, which is correct in the free space case, with the following function G_{sub} valid in presence of the substrate, found using the method of images:

$$G_{sub} = (1 - \gamma_s)\, G_{fs}, \tag{4.6}$$

where ε_s is the relative dielectric constant of the substrate and

$$\gamma_s = \frac{\varepsilon_s - \varepsilon_0}{\varepsilon_s + \varepsilon_0}. \tag{4.7}$$

The equation (4.7) is the approximation at the first term of a rapidly converging series [1].

Therefore from equations (4.4), (4.5), (4.6), the capacity C_{sub} of a pair of strips in presence of a dielectric substrate increases by the factor $(1 - \gamma_s)^{-1}$:

$$C_{sub} = \frac{C_{fs}}{1 - \gamma_s}. \tag{4.8}$$

4.5 Electrodes in the presence of a sample.

Let us consider the case of a sample with a plane and polished surface, faced to the strips like a mirror. In the present treatment, the sample thickness does not enter in calculations. Indicating with d the depth of the gap, the cited authors [1] suggest that, in the presence of the sample, the potential has to be estimated like in the equation (4.4) but substituting the function G_{fs} with the following suitable function G_m:

$$G_m\,(x, y, z; y', z') = (1 - \gamma_s)\left[G'_{fs}(y, z; y', z') - \gamma_m G''_{fs}(2d; y, z; y', z')\right], \tag{4.9}$$

where

$$G'_{fs}(y, z; y', z') = G_{fs}(0, y, z; y', z') = \frac{1}{\sqrt{(y - y')^2 + (z - z')^2}} \tag{4.10}$$

$$G''_{fs}(d; y, z; y', z') = G_{fs}(2d, y, z; y', z') = \frac{1}{\sqrt{4d^2 + (y - y')^2 + (z - z')^2}}$$

$$\gamma_m = \frac{\epsilon_0 - \epsilon_m}{\epsilon_0 + \epsilon_m}$$

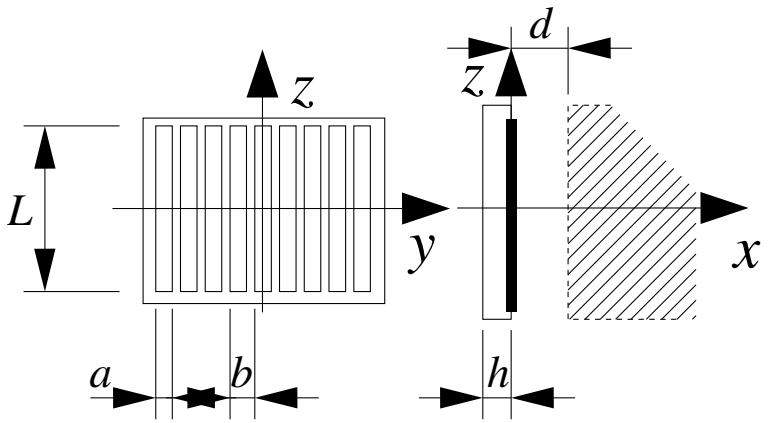

Figure 4.2: Schematic front (left) and side (right) view of the multistrip displacement device. The reference system is (x, y, z), the gap d, the length of the electrodes L, the width a, the semi-period b. The shaded area on the left represents the sample, which is placed in front of the "multistrip sensor like a mirror.

Using the previous definition (4.9) instead of G_{fs} and the boundary condition of fixed potential $\pm V_0$ on the electrodes, we can again invert numerically the equation (4.4) to estimate point by point the charge density function ρ_m as a function of the gap d in the case of the strips on the substrates plus the sample. Then we can again calculate numerically the integral (4.5) substituting the function ρ with ρ_m obtaining the value of the capacity C_m in the case of a pair of strips on a substrate with a dielectric sample in front.

For a sketching view of the complete multistrip device and the convention about the reference system, see the Figure 4.2. The total capacity of the device will then be $C_m^{tot} = N/2 \times C_m$, where N is the number of the electrodes.

4.6 Device sensitivity and optimization.

We are interested in estimating the displacement sensitivity of the multistrip sensor in order to optimize it, for example, to have the best sensitivity with the smallest possible area. This possible but not sole choice is suggested because one of the most relevant non intrinsic dissipation sources is the so-called gas damping: the dissipation is generated by the momentum transfer from the vibrating plate to the surrounding gas due to the collisions between the plate and the molecules of gas. This

dissipation is the more relevant the larger is the sensor surface. We will deal with the gas damping later, describing experimental results on silicon in Chapter 4.

The displacement sensitivity of the sensor can be evaluated as follows. Let Q_0 and C_0 be the rest charge and capacity, respectively. If we consider the total charge Q_0 constant, when the plate vibrates, the dynamical capacity at the first order can be written as

$$C(t) = C_0 + \Delta C(t).$$

with $\Delta C \ll C_0$. Then the potential can be written as follows:

$$V(t) = \frac{Q_0}{C_0 + \Delta C(t)} \simeq V_0 \left(1 - \frac{\Delta C(t)}{C_0}\right) \tag{4.11}$$

where we used the following first order approximation

$$\frac{1}{1+x} \overset{x\to 0}{\simeq} 1 - x.$$

If we denote with d_0 the rest gap corresponding to the rest capacity C_0, and $C'(d_0) \equiv (dC/dx)_{x=d_0}$, then, truncating the Taylor series at the first order, we can write

$$\frac{\Delta C}{C_0} = \frac{1}{C_0} C'(d_0)\Delta x. \tag{4.12}$$

Substituting (4.12) in (4.11) we finally obtain the displacement sensitivity, i.e. the voltage response ΔV to the gap displacement Δx:

$$\frac{\Delta V}{\Delta x} = -\frac{V_0}{C_0} C'(d_0) \tag{4.13}$$

The previous result does not take into account the parasitic capacity (for instance due to wires). If we do, in order to obtain the total sensitivity, we have to multiply the expression in equation 4.13 by the factor $1/(1 + C_{par}/C_0)$, i.e.

$$\left.\frac{\Delta V}{\Delta x}\right|_{tot} = \left.\frac{\Delta V}{\Delta x}\right|_{(3.13)} \frac{1}{1 + C_{par}/C_0} \tag{4.14}$$

Once evaluated numerically the capacity as function of the gap $C(d)$ using the algorithm described in the previous sections, then it is possible to determine the derivative $C(d)$ by numerical differentiation and finally the device sensitivity by the previous equation (4.13). We will predict the displacement sensor sensitivity as a function of the two geometrical parameters a, b, leaving the electrodes length L, the number

of the electrodes N constituting the "multistrip array and the rest gap d_0 constant.

The (a, b) parameter space was spanned looking for the maximum sensitivity. The range of spanned parameters space is $[a \times b] = 600 \times 600\mu m^2$ with a resolution of 13×13 μm^2. The electrodes length L and the gap d_0 are fixed to 10 mm and 50 μm, respectively. The bias operating voltage is chosen to $V_0 = 100$ Volt and remains constant throughout all calculations. The number of the electrodes N is estimated by the values of a and b in order to keep the sensitive area around 1 cm^2. In Figure 4.3 the displacement sensitivity is plotted as function of the parameters a and b. The maximum obtainable displacement sensitivity is $\sim$340 μV/nm for a=0.5mm and b=0.7mm. The array is formed by 14 identical electrodes for a total sensitive area of $\sim$1 cm^2.

4.7 Multistrip array fulfillment and bench test.

Within the DUAL R&D scientific activity, two different prototypes of the comb capacitor has been realized, tested on bench and employed as displacement sensors in low mechanical dissipation measures of Silicon samples both at room and at cryogenic temperature (2$\div$300 K). Both sensors are tested on bench at room temperature using flat P-doped 0.5 mm thick silicon disk as dielectric sample. The gap between mirror and electrodes is measured by a micrometer and varies in the interval 0$\div$3 mm with 0.2 mm resolution. The device capacity is measured in air as a function of the gap by a commercial precision meter (HP© 4284 A).

The first realized "multistrip sensor is formed by 84 electrodes having sizes $a = 0.4$ mm, $b = 0.6$ mm, $L = 10$ mm (see Figure4.2 for a description of the parameters). The whole device is obtained cutting out the array by a commercial circuit board plotter from a commercial copper layer ($\sim$ 10μm thick), deposited on a $h = 1.6$ mm thickness vetronite substrate. The total sensitive area is $\simeq$500 mm^2. The electrode array capacity in air in this case is $C_m = 25$ pF. In Figure 4.4 the device is shown in a picture.

Another sensor with smaller area has been realized in a second time applying the optimization process previously described to look for a peculiar arrangement of the parameters in order to have the maximum sensitivity with the smallest possible sensitive area. The fixed parameters are the rest gap $d_0 = 50\mu$m, the bias voltage $V_0 = 100$ Volt and the total sensitive area $\sim$ 1cm^2. Both substrate and electrodes are made with the same materials and manufactured with the same procedure. In Figure 4.5 a picture of the device is reported.

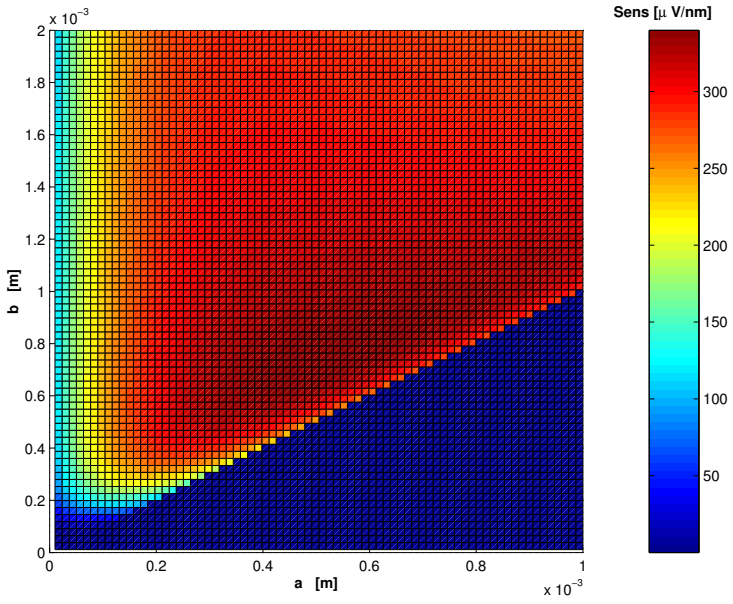

Figure 4.3: **Displacement sensitivity.** The displacement sensitivity is reported as function of the strip width a and the semi-period b. The other parameters are all fixed: gap d =50μm, electrodes length L =10mm, voltage bias V_0=100Volt, total sensitive area $\sim 1cm^2$. The blue area is the region of the parameters space where $a > b$: this is physically senseless, so the sensitivity is put arbitrarily to zero. The colour bar on the right reports the sensitivity scale in $[\mu V/nm]$. The maximum sensitivity results to be $\sim 340\mu V/nm$ with a=0.5mm and b=0.7mm. The region of parameters space swept is $[a, b] = [10, 1000] \times [10, 2000]\mu m$ with 13 μm resolution. The second manufactured multistrip array is carried out with these values for geometrical parameters, for which it should have the maximum sensitivity.

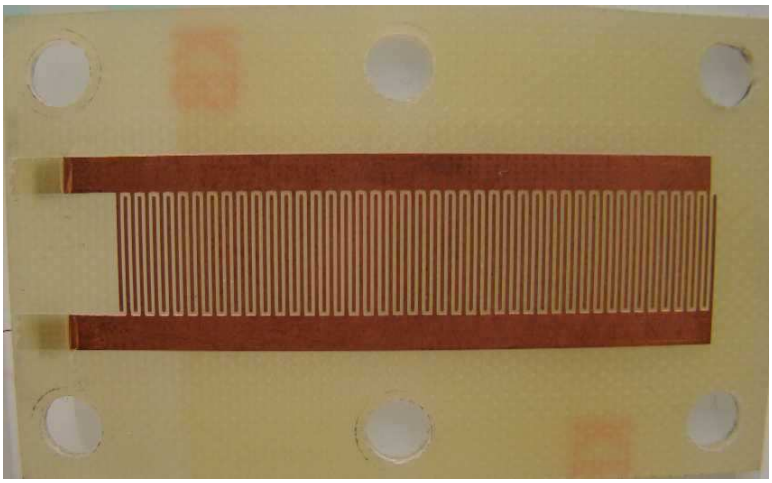

Figure 4.4: **Large area multistrip array.** The realized large area capacitive displacement sensor is shown in this picture. It is formed by 84 rectangular electrodes, each 0.4 mm large (a) and 10 mm long (L). (*See 4.2 for a description of the parameters.*) The distance between two consecutive ones is 0.6 mm (b). They are connected together alternatively, forming two fine-tooth combs each inside other. The array was cut out from a commercial copper layer ($\sim 10\mu$m thick, in gold in the picture) deposited on a 1.6 mm thickness vetronite substrate ($\epsilon_r = 4.5$, green in the picture). The comb array capacity in air is $C_m \sim$25 pF.

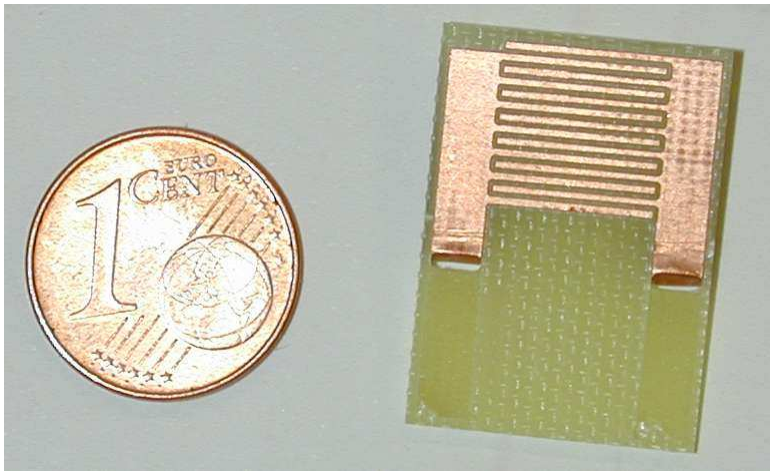

Figure 4.5: **Small area multistrip array.** The realized small area capacitive displacement sensor is shown in a picture. The topology and the manufacturing procedure is the same of the previous large area array presented. This one is formed by 14 rectangular electrodes, each of width a ∼0.4 mm and length L ∼9.8 mm, with hollow space between each other $(b - a)$ ∼0.3 mm, measured under a microscope comparator. Nominal values as resulting from optimization in figure were a=0.5 mm, b=0.7 mm and L=10 mm.

In the Figure 4.6 the bench measures are shown and compared with the prediction of the model. The agreement is rather good even if some measurement missing, maybe mainly due to the fact that some misalignment remains between the electrodes plane and the sample surface, probably due to holding. This most likely is the main cause, since this misalignment gives rise to an uncertainty in the measure of the zero on the micrometer scale, and then to an uncertainty in the measure of the gap.

The described and employed method provides an approximated solution for the charge density distribution over the electrodes, and, as a consequence, for the capacity of the array. It is possible to find an analytical solution for the density taking in account the contribute of all electrodes. However we realized that in practice the array capacity evaluated in this way does not differ appreciably from the one calculated as n times the capacity of the single pair of strips, where n is the total number of pairs. Furthermore, in this way, the computation results rather slower, and the game is not worth the candle.

The charge density function - that is the first fundamental step to evaluate the capacity of the whole array - is evaluated numerically point by point on a mesh on the electrodes. All results reported in this

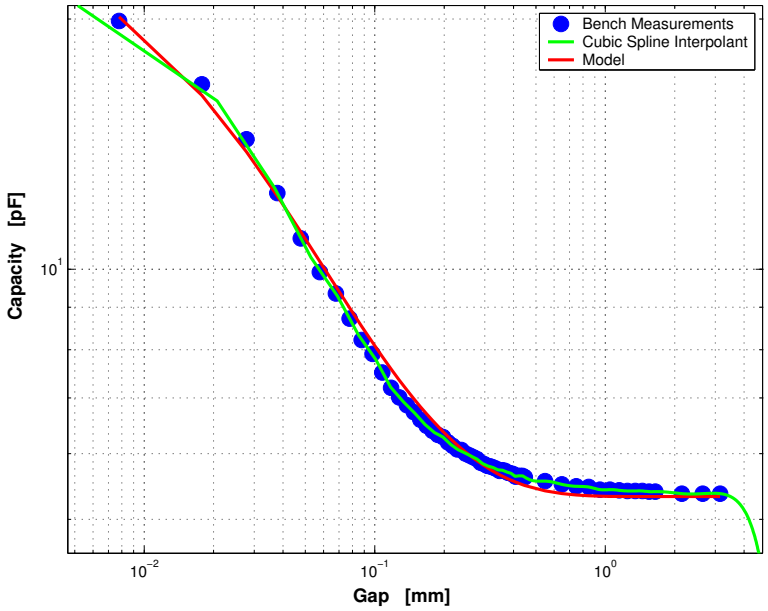

Figure 4.6: **Bench measurement of the capacity as function of the gap.** The measures are plotted in blue dots. The continuous red line is the model prediction obtained applying the algorithm described in the text. The charge density is numerically evaluated on a mesh of the surface electrodes, and then the multistrip array capacity is evaluated integrating numerically the density. All calculations and simulations are performed by original and *ad hoc* software written in commercial MalLab© code. The magenta continuous line is a cubic spline interpolant. The error bars on the experimental data points are not reported explicitly since they clash with the marker' size.

chapter are performed in saturation condition, i.e. the employed mesh is such that another finer one will produce the same value in the total capacity of the array.

In the Figure 4.7 the numerical derivative $C(d)$ of the model and the cubic interpolant spline are compared with good agreement, also considering all the approximations described above in the text. Therefore, the numerical evaluated capacity $C(d)$ and its numerical derivative $C(d)$ (as function of the gap) are inserted in equation (4.13) to evaluate the device displacement sensitivity numerically. Fixing the bias potential V_0, the device displacement sensitivity can be evaluated as a function of the gap, i.e. the capacitive readout can be calibrated.

In Figure 4.8 the readout displacement calibration is shown. The displacement sensitivity is reported for different values of the bias voltage V_0 as a function of the gap, as indicated on the graph. It is in-

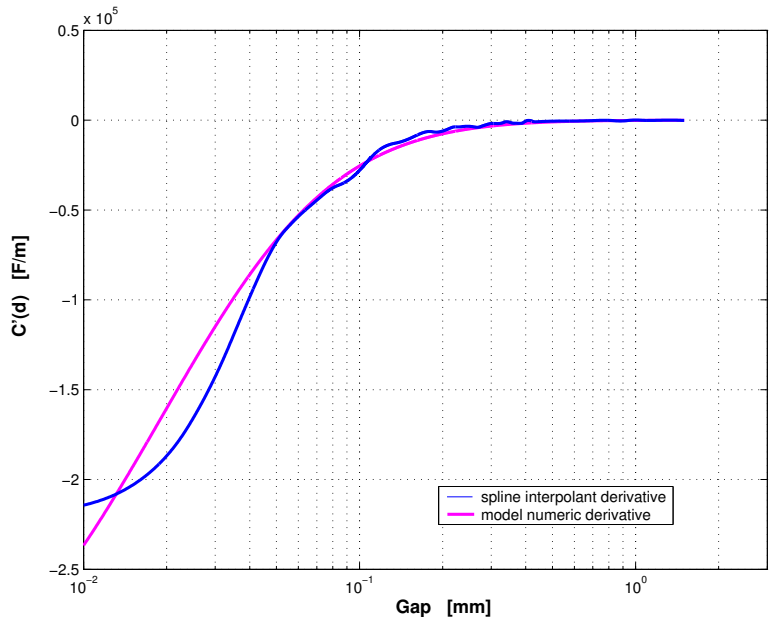

Figure 4.7: **Comparison between model and cubic spline interpolant numerical derivative.** The magenta line plots the numerical derivative evaluated by the model prediction reported in the previous figure (red line there). The blue line is the numerical derivative of the interpolant cubic spline fitting the experimental data and reported in the previous figure (green line there).

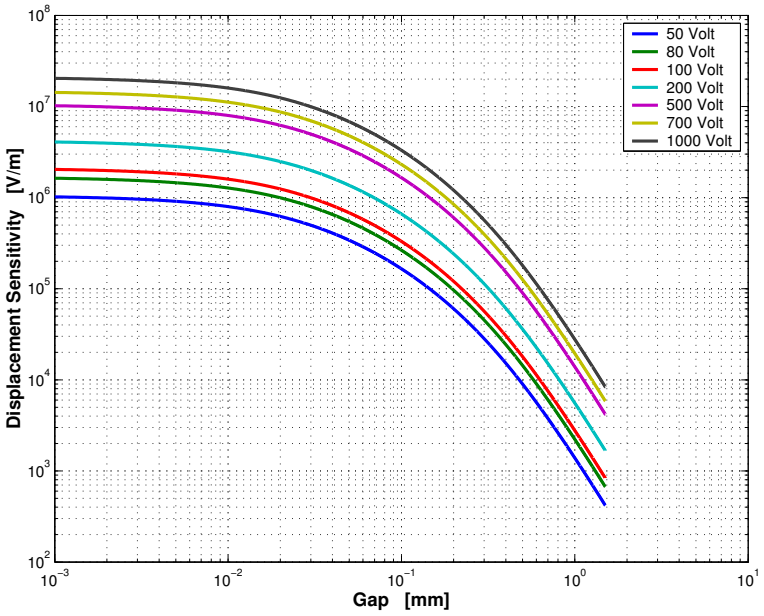

Figure 4.8: **Small area displacement sensor calibration.** The small area comb capacitor was tested and calibrated on bench. In the figure the calibration is shown. The displacement sensitivity is plotted as a function of the gap for different values of the charge voltage. Usual operative values (during the measurements reported later in chapter 4) are gap $\sim$50$\div$80 μm, V_0=100 Volt corresponding to an expected sensitivity of $\sim 6\times10^5$ Volt/m, against 1.5×10^6 Volt/m maximum available sensitivity in saturation for 100 Volt bias charge. Real sensitivity in experimental conditions should be about 10 times lower, since it can be estimated that $1/(1+C_{par}/C_0) \sim 1/10$, where C_{par} is the parasitic capacitance mainly due to the connecting wires.

teresting to observe that the displacement sensitivity is linear in the bias charge but saturates as the gap reduces toward zero. Therefore, in order to increase the device sensitivity (keeping the geometrical parameters of the array constant at their values), it is more convenient to increase the voltage rather than reduce the gap below 10$\div$20 μm. In the experimental measurements the expected sensitivity should be reduced by the parasitic capacitances, as described by the equation 4.14. In the case of the TF experimental setup, the real sensitivity should be 0.1 times the ideal one (eq. (4.13) since it is estimated that $1/(1+C_{par}/C_0) \sim 1/10$, where C_{par} is the parasitic capacitance mainly due to the connecting wires.

The multistrip array prototype was employed in cryogenic quality factor measurements. The maximum quality factor measured was

$Q_{max} \simeq 4 \times 10^7$ at $\simeq 4$ K on a 9 cm diameter and 0.5 mm thick Silicon flat plate (for more details see the Chapter 4).

Bibliography

Bibliography of chapter 4.

[1] S.Grasso *et al.*, Electrostatic systems for fine control of mirror orientation in interferometric GW antennas, Physycs Letters A, **244**, (1998) 360-370

[2] A.Cadez, A.Abramovici, J. Phys. **E 21** (1988) 453

[3] J.B.Jackson, Classical Electrodynamics (Ed. Wiley, New York, 1962)

Chapter 5

Silicon.

5.1 Introduction.

The measurements on Silicon reported in the present PhD thesis have the purpose to estimate the contribute of silicon wafer bonding technique to the mechanical losses in the acoustic frequency range (100 Hz $\div$ 10 kHz) at cryogenic temperature. As discussed in the Chapter I, the interest in the dissipation of bonding layers in materials arises from the need of developing very large masses [1] with extremely low mechanical losses for the sensitive mass of gravitational waves detector DUAL.

Different silicon wafer bonding techniques have been developed for purposes different than that expounded here, for example to obtain vacuum sealing or, in basic research, to realize monolithic objects with high stability and mechanical strength at room temperature. In the field of gravitational wave experiments, stable platforms and quasi-monolithic suspensions are made by hydroxyl-catalyzed bonding, so called "silicate bonding" [4]. In origin it seems that this technique was developed to join fused-silica parts together to make the star-tracking telescope of the Gravity Probe B space mission. This same technique is today applied successfully to other materials than silicon, as for example sapphire.

Silicon shows very low mechanical loss angle ($\phi \sim 10^{-8} \div 10^{-9}$) both at room [1] and at cryogenic [3] temperature but short informations are available about the contribute in losses due to bonding methods at cryogenic temperatures. However some information is available at higher temperatures as investigations are being continued since several years.

The measured loss, ϕ_m, is the sum of dissipation arising from a

[1] In general of the order from several to about ten or more, according to the chosen material. For example, in the case of silicon, the mass is $\sim$10 tons.

number of sources, which can be grouped in a possible way as

- *intrinsic* losses, ϕ_{int}, whose source is to be searched inside the material itself as, for example, loss resulting from thermoelastic damping (ϕ_{TE}), the bulk (or volume) loss of the material (ϕ_b), the loss associated with the surface layer (ϕ_s), and so on;
- *extrinsic* (or *external*) losses, ϕ_{ext}, whose source is in the coupling between the material and the external environment during the measurement as, for example, the loss associated with the clamping structure (ϕ_{clamp}), the loss due to damping from residual gas molecules (ϕ_{gas}), and so on.

It is important to underline that the intrinsic losses can be again grouped in two categories: losses due to materials imperfections (for example doping or surface imperfections) and fundamental losses, distinctive of even perfect materials (for example thermoelastic losses even for materials with perfect crystal lattices). Thus the total losses can be expressed as the sum

$$\phi_m = \phi_{int} + \phi_{ext}, \tag{5.1}$$

keeping in mind that each term can be expressed again as a more detailed sum, when the single dissipation sources are known and/or modelled. External losses ϕ_{ext} often limit low-loss measurement. The present work deals with isolating the sample under measurements from the external loss sources in order to minimize ϕ_{ext}. On the other hand, it tries to understand the different contributions that sum up in the measured losses. The experimental setup is characterized in the $2 \div 300$ K temperature range and is suited also to characterize additive losses contributed by other processes on silicon, as for example surface coatings and other post-production treatments.

5.2 The sample.

The adopted geometry for silicon samples is thin circular disk (so called "wafers"). This simple geometry is the standard in semi-conductor devices fabrication, such as integrated circuits, and therefore it is largely available. The tested samples are single crystal of n-type silicon wafers, polished on both sides, with a radius of 100.2 ± 0.1 mm and a thickness of 500 ± 15 μm. The silicon was doped with phosphor to an impurity concentration of $10^{14} \div 10^{15}$ atoms/cm^3. The resistivity is $\sim 9 \div 24 \Omega$ cm. The lattice orientation of the wafer, defined by the plane of its top surface, is (100). According to production standards, each wafer

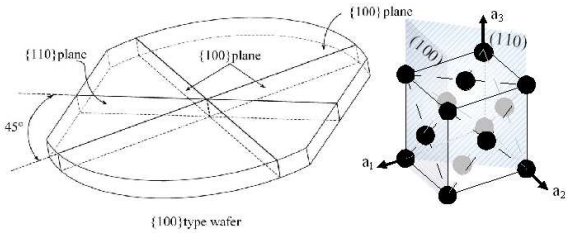

Figure 5.1: **Silicon Wafer.** (Left) Sketching view of the silicon wafer sample employed in low temperature loss measurements in TF. The central hole is not shown. The crystallographic planes of interest are reported. (Right) The silicon face centered cubic (fcc) lattice at the side of the sample. The planes (100) and (110) are in evidence. The wafer dimensions are the followings: diameter: 100.2±0.1 mm; thickness: 500±15μm; distance between the cuts: 94.8±0.1 mm.

was shaped with a flat cut perpendicular to the (110) crystallographic plane. But this cut moves the centre of the oscillations away from the centre of mass, preventing from realizing a nodal suspension (which will be dealt with in details in the next section). In order to make the geometry symmetric and the centre of the wafer circumference to coincide with the mass centre of the oscillations, a second, identical and specular cut was made parallel to the first one. The second cut was made using a diamond saw blade. The distance between the cuts was measured to be (94.8 ± 0.1)mm. In Figure 5.1 they are shown a sketching view of the silicon wafer employed in TF cryogenic measurements and a detail of the face centred cubic (fcc) lattice with the (100) and (110) planes in evidence.

FEM analysis on the cut disks showed that the wafers exhibit a number of resonant modes in the acoustic frequency range of our interest. The results are summarized in Table 5.1.

The silicon crystal is anisotropic with cubic symmetry, so its Young modulus varies in the material along different directions with respect to the crystal orientation. In the crystal axis coordinate system, silicon elastic properties can be described by a 6×6 symmetric stiffness matrix C_{ij} with only 3 independent entries [7]: $C_{11} = C_{22} = C_{33} = 167.5$ GPa, $C_{12} = C_{23} = 65$ GPa, $C_{44} = C_{55} = C_{66} = 80.1$ GPa. These values determines the following values for Young modulus in the plane of our (100) wafer:

- parallel to flat: $E^{+} = 169$ GPa,
- 45 degree diagonal to flat: $E^{\times} = 130$ GPa.

Mode	ν_{FEM}	ν_{TH}	ν_{DH}	(a, n, s)
—	[Hz]	[Hz]	[Hz]	
1	71.3	—	—	ort1
2	73.7	—	—	ort1
3	275.4	275.3	275.3	(0, 0, 0)
4	386.0	380.1	383.0	(2, 0, ×)
5	483.0	489.3	484.6	(2, 0, +)
6	984.0	972.9	975.7	(3, 0, ×)
7	997.0	985.0	989.0	(3, 0, +)
8	1518.0	1478.0	—	ort3
9	1543.0	—	—	(1, 0, ×)
10	1607.0	—	—	(1, 0, +)
11	1733.0	1721,0	1720.0	(4, 0, ×)
12	1766.0	1784.0	1772.0	(4, 0, +)
13	2539.0	2500.0	2515.0	(2, 1, ×)
14	2649.0	2633.0	2629.0	(5, 0, ×)
15	2663.0	2636.0	2638.0	(5, 0, +)
16	2805.0	2846.0	2814.0	(2, 1, +)
17	3744.0	3701.0	3702.0	(6, 1, ×)
18	3744.0	3703.0	3712.0	(6, 1, +)
19	3950.0	3924.0	3923.0	(3, 1, ×)
20	3995.0	—	—	(3, 1, +)

Table 5.1: **FEM results.** Resonant frequency of the first 20 acoustic modes of the wafer with the two symmetric cuts. ν_{FEM} is the FEM estimation for the resonant frequency of the corresponding normal mode. ν_{TH} and ν_{DH} are the room temperature experimental measure of the frequency for the sample with Through Hole (TH) and Dead Holes (DH), respectively. The 5th column gives identification for the symmetry in normal modes motion. More details about an elastic model of the samples and FEM analysis results are collected in Appendix A.

The thermal conductivity of n-type silicon as function of temperature below 100 K was reported by Thompson and Younglove [6]. Almost all other thermomechanical properties of silicon, used as inputs in numerical analysys discussed in the followings, can be found in the database [5].

5.3 Nodal suspension.

The term "nodal suspension" means that the sample is clamped in a nodal point, i.e. a point that remains at rest during the oscillations of the sample. In this way the reaction force applied by the holder is highly suppressed and its contribution to mechanical loss is minimized. In fact, since the holder is an elastic body, it can apply its constraining reaction force only changing its dimensions, according to its stress-strain reactions, and if the holder participates in the motion then it can dissipate part of the sample motion energy increasing the total losses. In principle the nodal suspension should completely cancel the holder contribution in losses as the nodal point is perfectly at rest. In practice the experimental implementation of a nodal clamping is obviously approximated and hence a residual contribute to total losses from the clamping is expected.

Two crucial points in assembling operations are the followings:

- to clamp the sample in its centre as precisely as possible and over the smaller possible area; this is the only way to minimize the residual contribute to total losses from the nodal clamping itself;
- to avoid misalignments between the two clamping spheres; in fact, such a misalignment would apply a torsional moment on the sample, making it tilt and drop during assembling operation or, at the worst, during measurements in vacuum.

For these reasons, a reference mark is needed on the sample centre where put the clamping spheres during assembling operations. Two different solutions are adopted on different samples:

- a through hole (0.5 mm in diameter) was drilled at the centre of the wafer using a dental cutter. This manufacturing was done after the cut described in the previous section, at the mechanical workshop of LNL;
- two notches was excavated at the centre of both sides of the wafer via chemical wet etching. This manufacturing was done before the flat cut described in the previous section was made. Since it

follows the (111) crystal plane, the chemical etching ends up in pyramidal cuts (see Figure 5.2). In our case, the cut is 175 μm deep and with a square section having a side of 0.5 mm at the surface.
The hole is obtained using the Micro Electro Mechanical Systems (MEMS) technology available at "*Fondazione Bruno Kessler*"– IRST, Trento, Italy. In short, the process is the following. Initially, a 500 nm thick thermal silicon oxide layer and a 100 nm thick Low Pressure Chemical Vapor (LPCV) silicon nitride layer are respectively grown and deposited on both wafer sides. Then a central hole is opened in the oxide-nitride layers via photolithography followed by a plasma dry etching that stops selectively at the silicon surface. The silicon is then etched with wet Tetramethylammonium Hydroxide (TMAH) 25% 90 solution for several hours on each side. TMAH is highly selective with respect to the oxide-nitride mask. Once the wafer central hole (one per side) have reached the desired size, the mask layers are removed.

The nodal holder was implemented both on silicon wafers and on silicon carbide disks. Here the case of silicon is discussed while the silicon carbide will be dealt with in the next chapter. A sketching view is shown in Figure 5.2, to which we will refer throughout the followings describing each component. The silicon wafer is kept horizontally. Two spheres (9) realize the contact between the holders and the wafer, similarly as done by *Numata et al*[2]. The spheres are 1 mm diameter in sapphire, very low loss material. The low loss property is required to avoid losses on clamping. The holder is based on an aluminium circular plate ((1) in Figure 5.2) on which the lower support (2) is screwed. It is realized in OFHC (Oxygen Free High Conductivity) copper. At the centre of its top surface a small notch (0.3 mm diameter) houses the lower sapphire sphere.

The upper sapphire sphere (9) is housed in the hollow on the top surface of the disk. The upper holder (7) exerts a pressure on the sphere below assuring the clamping of the wafer. The pressure is assured thanks to the steel spring (8) with elastic constant $\sim$0.75 N/mm. Acting on the two screws (5), one can adjust the position of the upper beam (6) and hence the compression of the spring, adjusting at last the exerted pressure. Usually the top beam is lowered by $\sim 2 \div 3$ mm, so the spring is calibrated to exert max $\sim$2N on the top sphere. This should prevent sample breaking during assembling operations, on the other hand assures enough pressure to keep the plate horizontally.

In Figure 5.2 the capacitive "multistrip" readout (4) is shown. The optical lever readout (red arrow) is shown too but it will be briefly

described in section 5.

5.4 Capacitive readout.

In order to minimize the sensor contribution to mechanical losses, a contact-less displacement sensor was employed. It is a capacitive readout developed to be sensitive to displacement of dielectric samples; it was dealt with in details in Chapter 3. The sensor was made in two different versions, large and small sensitive area, and they were employed with different samples. The array used for most of all the measurements reported here is the first type and it shown in Figure 4.4 in the previous chapter. The small area sensor shows slightly higher sensitivity and it is used in preference with samples of small dimensions but not only. However, in Tables 5.2 and 5.3 the comb capacitor employment as displacement sensor is summarized.

The large area one consists in an array of $N = 84$ plane, rectangular electrodes having the form of a bar code of semiperiod $b = 0.6$ mm. The strips have width $a = 0.4$ mm and length $L = 10$ mm. The total length of the array is then $\sim$50 mm. The whole device is obtained cutting out the array by a commercial circuit board plotter from a commercial copper layer ($\sim 10\mu$m thick), deposited on a $h = 1.6$ mm thickness vetronite substrate. A scheme with the used nomenclature is reported in Figure 5.4.

The device (both in large and small area version) is glued by commercial Stycast© 2850 on the bottom plane of an aluminium support which in turn is screwed on the same aluminium basement supporting the silicon wafer. A particular of the assembled device is shown in Figure 5.3.

The multistrip array is placed near the surface of the silicon wafer with the plane of the electrodes parallel to the wafer surface. The estimate gap is $\sim$75 μm. The array is radial oriented with its longitudinal axis approximately parallel to the cuts of the wafer.

Electrical scheme of the sensor is shown in Figure 5.4. The electrodes are alternatively at potential V_0 and ground. The V_0 potential is supplied by a high-voltage generator. More often than not during measurements with both the large and small area sensors, bias voltage is set to 80$\div$100 Volt. Half of the electrodes are connected to a decoupling low-loss high-voltage capacitor ($C_d \sim 200nF$) and the signal is read between ground and the positive pole of the multistrip array which is connected to the decoupling capacitor. During charge operations, both the switches in Figure 5.4 are closed and the charge line is connected to a high voltage generator providing the bias voltage.

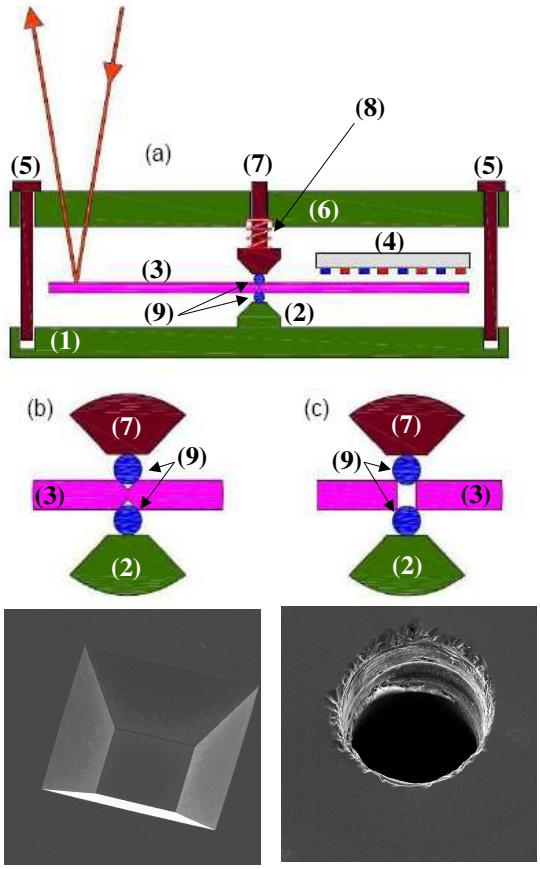

Figure 5.2: **Nodal suspension.** Up: (a) the sample with its nodal clamping is shown. The draw is not to scale. Both optical lever and "comb" capacitive displacement sensors are shown. (1) Aluminum basement plate; (2) lower copper support screwed on the aluminum basement (1); (3) sample silicon flat plate (the same clamping system is used for silicon carbide too, see Chapter 5); (4) "comb" capacitive readout; (5) threaded rods with nuts: the rods are screwed directly on the basement (1) and acting on the nuts it is possible to move the horizontal beam (6), setting the spring (8) compression and hence setting the pressure on the nodal clamping point; (6) horizontal beam: it houses the rods (5), the upper holder (7) and the steel spring (8); (7) upper steel holder: on its lower surface it is made a notch to house the upper sapphire sphere (9); (8) steel spring; (9) upper and lower sapphire spheres. Middle: nodal points details (b) in the case of two cuts made at the center of both sides of the wafer via chemical wet etching; (c) in the case of through hole drilled at the center of the wafer by a dental cutter. Bottom: scanning electron microscope photographs of the silicon sample central nodal points (b) in the case of chemical wet etching notch; (c) in the case of through hole.

Material	Sample	h [mm]	L or d [mm]	Clamping	Hole	RUN
Sintered SiC	Cantilever	0.3	50	by edge	—	2-4
		0.5	100			
Infiltrated SiC	Cantilever	5	70	by edge	—	2-4
(C-SiC)		3	90			
Silicon	Disk	0.5	100	nodal	Through	7
		0.9	100		Blind	

Table 5.2: **Large area comb capacitor usage.** The table collects the occurrences when the large area multistrip array was employed in cryogenic loss angle measurements. The columns list, respectively, the material under investigation; the kind of sample used; its thickness; its length (L for cantilevers) or diameter (d, for disks); the clamping kind adopted; the hole type (if present, otherwise "glued" indicates that the clamping sphere is simply glued in the centre over the polished surface); finally the cryogenic TF run id-number. In the table also the silicon carbide is reported even if the measurements on it will be reported in the next chapter.

Material	Sample	h [mm]	L or d [mm]	Clamping	Hole	RUN
Silicon	Disk	0.5	100	nodal	glued blind hole	6
Silicate bonding	Disk	0.9	100	nodal	glued blind hole	7
Mono-crystalline SiC 4HN	Disk	0.3	50	nodal	glued no hole	7
Mono-crystalline SiC 6HN	Disk	0.3	50	nodal	glued no hole	7

Table 5.3: **Small area comb capacitor usage.** The table collects the occurrences when the small area multistrip array was employed in cryogenic loss angle measurements. The columns content is the same as the previous Table 5.2.

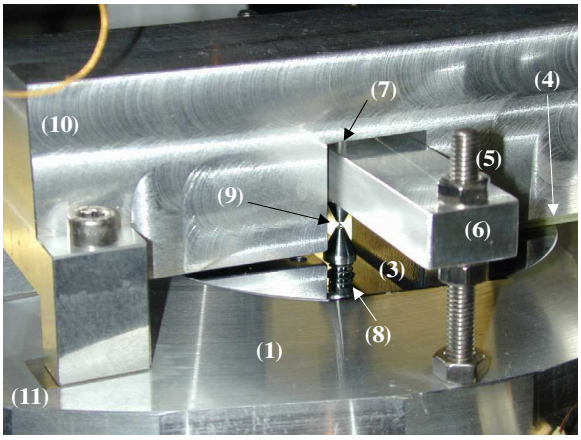

Figure 5.3: **Silicon wafer on nodal clamping.** Silicon wafer housed in its holder with nodal suspension and capacitive readout. The indices lower than (10) refers as in the previous Figure 5.2. (10) Aluminum support. On its bottom surface the comb capacitor (4) is glued. The only way to adjust the gap between the sensor and the electrodes is to insert flat washers (11) between the base and the array support. The steel spring (8) is visible in an image reflected by the mirror surface of the silicon sample. Upper sapphire sphere (9) is visible at the nodal centre of the sample.

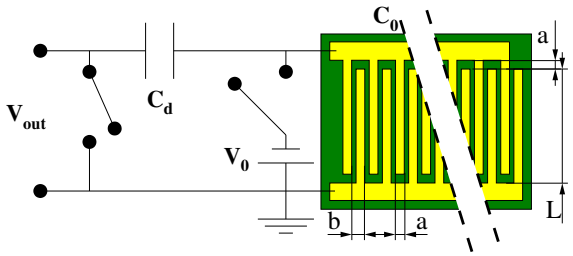

Figure 5.4: **Electrical scheme of the strip sensor.** C_0 represents the multistrip array capacitor, C_d the decoupling capacitor and V_0 the bias voltage. During charging operations, both switches are closed. The output signal is read at the V_{out} terminals after that both switches are open.

When the decoupling capacitor C_d is charged, the generator is disconnected and the switch on the sensor is open, leaving a constant charge on the electrodes. The total charge remains constant, so that the relative movement between the sample and the sensor makes the charge distribution change on the electrodes surface: the signal is finally read as AC coupled voltage at the multistrip terminals.

Most of measurements on silicon wafers are performed using the large area multistrip. For this sensor the calibration is not reported, however its displacement sensitivity can be evaluated all the same following the procedure as exposed in Chapter 3 using in input the nominal geometrical parameters of the device. Putting the gap $d \sim 100nm$ and bias voltage $V_0 = 80Volt$, it results $C_0 \sim 45pF$, $C'(d) \sim 17fF/m$ and a sensitivity of $dV/dx \sim 30\mu V/nm$ is expected. In the experiment this number is reduced by a factor ~ 10 due to wire parasitic capacitances and by a further factor ~ 2 due to the fact that a fraction (about half) of the sensitive area gets out of the sample. Usually loss angle measurements are performed in the range $1 \div 10\mu V$ (lockin demodulated signal amplitude). Hence, with the considerations reported above, the typical displacement of the silicon wafer results to be of the order of the nanometer.

5.5 Optical readout.

The TF is provided with an optical window to allow loss angle measurements with a beam deflection sensor. This readout consists in monitoring the deflection of a laser beam by a displaced reflecting surface with a split photo-detector. This technique works for any material but it is better suited for highly reflective ones for two main reasons: the sample under measurement is not heated by absorption of the incident laser beam or of scattered light, and laser power can be limited, minimizing the heating of the sample under measurement. The optical bench is housed at room temperature over a 370×250 mm aluminium plate placed horizontally in air on the top of the TF. It supports a 100mW cw Nd:YAG laser, focusing optics and a split photodiode (not shown in Figure 3.1 in Chapter 2). The light path is folded twice on optical bench before entering a beam-splitter with 25% reflectivity. The transmitted beam is sent downwards to a 1" vacuum seal optical window, after that reaches the sample about 2 m below. The beam is then reflected upward by the sample through the same optical window. The beam transmitted by the beam-splitter is directed to a quadrant photodiode (EG&G 30845). The resulting 4 photocurrents are combined so to measure the changes in the optical density between the photodiode

sections. Therefore a transverse deflection or vibration is converted into a difference of electrical signals of top/bottom or left/right photodiode sections. The laser spot size at the sample is estimated to be about 0.2 mm. At 1 kHz the sensor is estimated to be sensitive to about 1 nm of wafer reflecting surface vertical displacement.

The laser beam deflection method is widely employed mainly for its simple experimental setup and the easy optical beam alignment. In the case of TF, its employment gets complicated because of the whole facility configuration. In particular, the beam must propagate on the same 40 mm diameter tube in both downward and upward directions and pass through the same 1" diameter optical window. The distance between the sample and the nearest optics is about 2 m and for most of the distance there is no access to the beam to monitor its propagation. This makes difficult the optics alignment. Moreover it is not possible to perform measurements on different oscillators during the same run since only one laser beam is available with fixed path.

However some measurements was performed with optical readout all the same and will be reported in the following sections. In particular, during a scientific run dedicated to temperature calibration, a silicon wafer (0.5 mm diameter) was lighted up by laser beam for several hours at 4.2 K without a significant temperature increase. This fact seems to confirm that the sample heating due to the impinging laser beam is negligible at 4.2 K, as expected from the high reflectivity of silicon in the band of the laser employed.

5.6 Measurement process.

For each available sample, the aim is to measure loss as a function of temperature via mechanical oscillations. From this point of view our silicon wafer is a mechanical oscillator characterized by a series of normal modes, each of them with its proper resonant frequency. The analytical solution is known in the case of a isotropic thin circular flat plate. Unfortunately, we have to do with cut non isotropic disks and in this case an analytical solution is unknown. So Finite Element Method (FEM) is applied to understand frequency and shape for each normal mode. As a result of FEM analysis, about the first twenty modes of our silicon wafer resonate below 4 kHz (see Table 5.1). Besides, for a few of them the external losses dominate and this means that they cannot be considered to estimate the intrinsic losses of the material. These modes are selected by shape characteristics and measured loss angle at higher temperatures at the beginning of the run and discarded from further measurements.

The loss angle is measured for each normal mode at the fixed temperature T by the so called "ring down" method, i.e. the measure of the normal mode resonant frequency ν and decay time τ by the acquisition of the amplitude decay of the mode itself. For each normal mode, the oscillation is excited making a piezoelectric (PZT) vibrate at the same frequency and high energy. The PZT is fixed to the base (see Figure 3.7 in Chapter 2). The excitation is a constant amplitude monochromatic sinusoid generated by a high stability frequency synthesizer (HP3325B), sent to a custom high voltage amplifier and finally to the PZT actuator. A lock-in amplifier demodulates the signal output of the displacement sensor; its reference is the same frequency of the signal sent to the PZT. Once excited, the voltage to PZT is removed and the mode starts decaying at its proper resonance frequency. The reference frequency then can be fine tuned on the synthesizer to make the phase constant on lock-in. The amplitude of lock-in demodulated output signal decays as the vibration amplitude of the sample; both amplitude and phase signal is acquired directly from lock-in SR830 output via GPIB and stored in a pc hard disk. The mechanical vibration follows an exponentially damped decay whose envelope amplitude law is

$$u(t) = u_0 \exp\left(-\frac{t}{\tau}\right) \tag{5.2}$$

so that the decay time τ is evaluated fitting data with the model given in the previous eq. 5.2. Identifying the normal mode resonant frequency ν with the fine tuned lock-in reference, the mechanical loss angle is estimated by the following relation:

$$\phi(\nu) = \frac{1}{\pi\nu\tau} \tag{5.3}$$

For most of all the measurements reported, the data are fitted over at least 2 decay times. [2]

The lowest loss angles was measured at about 7 K for the 0.5 mm thickness silicon wafer for the modes (4), (11) and (13) reported on Table 5.1. The measured values are 1.1×10^{-7}, 1.3×10^{-8} and 1.1×10^{-7}, respectively. A loss estimation was made, for what concerns thermoelastic losses, via FEM analysis; the results are shown more exhaustively in the next section together with experimental results. It can be anticipated here that the agreement between numerical thermoelastic predictions and experimental data is good. This seems an indication that thermoelastic loss dominates, at least at higher temperature.

[2] For example, at a typical frequency of ∼1000 Hz and with loss of $\phi \sim 10^{-7}$, the measurement takes a time of the order of $\gtrsim$ 2 hours.

5.7 Intrinsic losses.

Extremely low mechanical loss was measured on bulk silicon both at room [1] and cryogenic temperature (4K) [3]. On the contrary surface losses might be a limiting dissipation source, even if it is still not clear. In order to estimate the losses from this source, we compare our oscillator to other silicon ones, all characterized by different volume-to-surface ratios.

Authors in [15] collect data of room temperature losses for single-crystal silicon samples of different dimensions, which have not been annealed and for which reactive-ion etching has been involved, similarly to the wafer subject of this work. In Figure 5 [15] they summarize all such information and evidence a dependence of $1/\phi$ VS size of such samples. Considering the thickness of 500 μm, from this data trend we infer that surface losses at room temperature should be $\phi_s \leq 10^{-5}$. This value is more or less experimentally confirmed in our sample for the modes with lowest losses. Thus, for these modes, surface loss should contribute in some amount to total dissipation at room temperature, even though the dominant dissipation mechanism should be the thermoelastic (see Figure 5.6 and relative discussion). In fact, at room temperature the measured loss is consistent with the predicted thermoelastic damping and other contributes are barely appreciable.

We collected measured loss angle for a number of silicon samples of different shapes found in reference [3] and in references from [14] to [21]. In Figure 5.5 loss angle is plotted against the smallest oscillator dimension. All measurements are taken in the $1 \div 15$ K temperature range. For each group of researchers (i.e. for each oscillator design) the smallest reported loss angle is quoted. The measured loss depends clearly on size (or, equivalently, on volume-to-surface ratio) and this suggests that a relevant damping mechanism lies on the sample surface. Our measurement of mode (11) is reported in Figure 5.5 and it does not depart significantly from this trend. This suggests that surface losses explain at least part of the total losses for the mode (11) at liquid helium temperature.

5.8 Fundamental loss contribution.

In insulating solids such as silicon there are two main mechanism that set the lower limit to the total mechanism losses: the thermoelastic effect and the phonon-phonon interaction.

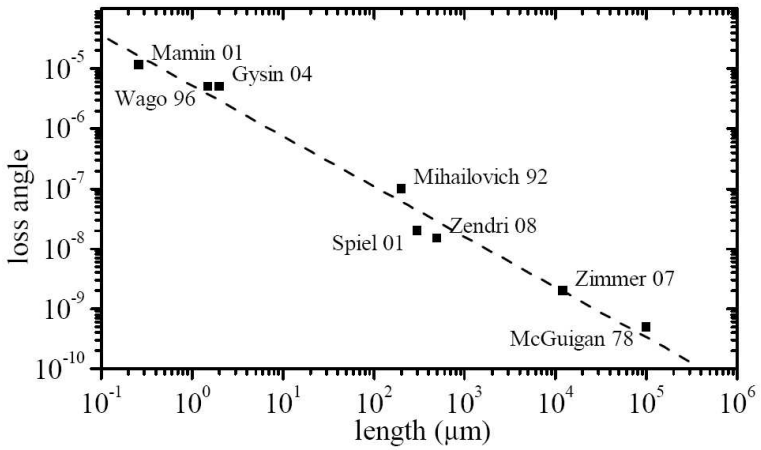

Figure 5.5: **Loss angle as a function of sample size.** Measured loss angle is plotted against the smallest sample dimension. Measurements are collected for a number of silicon samples which have not been annealed and for which reactive-ion etching has been involved, similarly to the wafer subject of this work, in the 1÷15K range of temperature. Points label indicates the first author of the corresponding paper and the publication year. Data are collected from reference [3] and in references from [14] to [21]. The measurement of the mode (11) of our sample is labelled as "*Zendri08*".

5.8.1 Thermoelastic damping.

It is known that an acoustic mode, such as a normal mode of vibration of an elastic resonator of finite geometry, experiences damping due to its non-linear interaction with a surrounding bath of *thermally excited* elastic modes, or phonons. A very elegant treatment is exposed by Lifshitz and Roukes [8] and it is reported here in its main principles. If the mean free path of these thermal phonons is much smaller than the wavelength of the acoustic mode, then sufficient thermalization occurs on the scale of interest. It is then possible to define a temperature locally, even when the system is not in a state of equilibrium. Conversely, if the relaxation rate of the phonon distribution to a local Bose-Einstein distribution is much faster than the frequency of the acoustic mode, then the temperature field can be well-defined, and there is no need to treat thermal phonons as individual excitations. In this regime the thermal phonons are said to be "diffusive". Just a single macroscopic parameter captures the complicated interaction between the acoustic mode and the thermal phonon bath (in an *isotropic* body), the material's *thermal expansion coefficient*

$$\alpha = \frac{1}{L}\frac{\partial L}{\partial T}, \tag{5.4}$$

where L stands for length and T is the temperature, since it couples changes of length with changes of temperature. [3]

When an elastic body is set in motion, it is carried out of its equilibrium, since it gets an excess of kinetic and potential energy. In the case of an isothermal and perfectly linear elastic body, this state of non-equilibrium motion can persist forever. But in a *thermoelastic* matter, the coupling of the strain field with the temperature one provides an energy dissipation mechanism that allows the system to relax back to the equilibrium. The *thermoelastic damping* is a fundamental process of energy dissipation according to which relaxation of thermoelastic solids occurs because of an irreversible flow of heat is driven by local temperature gradients throughout the coupled strain field. Here α plays as a coupling constant; as it is nonzero, thermoelastic damping introduces an upper limit to the quality factor of even the most perfectly designed and manufactured resonator.

The first to investigate the thermoelastic effect was Zener [9], who first realized that thermoelastic relaxation may be a significant source of damping in mechanical resonators. Zener treated the case of can-

[3] Here and in the followings, the *linear* thermal expansion will be used. Its value is one third of the volumetric coefficient of thermal expansion.

tilevers' pure flexures, for which the expected loss is

$$\phi_{th}(\omega) = \frac{Y\alpha^2 T}{\rho C_V} \frac{\omega\tau_{th}}{1+\omega^2\tau_{th}^2} \tag{5.5}$$

where Y is the Young's modulus, ρ the density, C_V the specific heat per unit volume of the material; $\omega = 2\pi\nu$ is the angular frequency and T is the temperature of the oscillating sample. The *relaxation time* τ_{th} is defined in the following equation (5.6).

In the frequency domain, the dissipation exhibits a Lorenzian behaviour as a function of $\omega\tau_{th}$ with its maximum value of $Y\alpha^2 T/2\rho C_V$ when $\omega\tau_{th} = 1$. Dissipation peaks of this form are generally called "Debye peaks", but they occur for many different relaxation mechanisms such as, for example, point-defect relaxation ("Snoek peaks"), defect pair reorientation ("Zener peaks"), dislocation relaxation ("Bordoni peaks"), grain-boundary relaxation and thermal relaxation (see [8] and the detailed review cited therein [10]). In some cases there is not just one single relaxation time and therefore multiple or broadened Debye peaks can be seen. [4]

Why there is a peak in dissipation for $\omega\tau = 1$ can be understood intuitively as suggested by Lifshitz and Roukes [8] in the following way. If the frequency of vibration is much smaller than the effective relaxation rate ($\omega \ll 1/\tau$), then the system remains essentially in equilibrium and very little energy is dissipated. If the vibration frequency is much larger than the effective relaxation rate ($\omega \gg 1/\tau$), the system has no time to relax and again very little energy is dissipated. An appreciable dissipation can occur only when the vibration frequency is on the order of the system's effective relaxation rate. However all can be much more complicated in the cases in which τ itself depends on ω.

The dissipation due to thermoelastic effect depends on the oscillator size through the relaxation time τ_{th}:

$$\tau_{th} = \frac{h^2 \rho C_V}{\pi^2 \kappa} \tag{5.6}$$

where h is the oscillator thickness and κ the thermal conductivity. As said above, the previous equation (5.5) is valid for cantilever's pure flexures. Ferreirinho [11, Ch. 6 and therein] gave the thermoelastic internal friction for the flexural modes of a thin circular disk:

$$\phi_{td}(\omega) = A_n \frac{1+\sigma}{1-\sigma} \phi_{th} \tag{5.7}$$

[4] Anyway, in all the measurements presented in this thesis, they are considered only acoustic waves of angular frequency ω such that $\omega\tau_{th} \ll 1$. So these peaks are never observed in measurements presented here.

where $A_n \leq 1$ is a dimensionless numerical constant characteristic of the nth flexural mode and $A_n = 1$ corresponds to plane bending [11, and therein]; σ is the (constant) applied strain. It is worth to remark that the thermoelastic internal friction in the two cases of equations (5.5) and (5.7) are proportional by a constant dimensionless factor $C_n \equiv A_n(1+\sigma)/(1-\sigma)$.

In the case of our sample, its shape is not exactly circular because of the two symmetric cuts. So the previous expression (5.7) cannot be properly applied. In order to estimate as precisely as possible the thermoelastic damping of all modes involved in experimental measurements, a FEM analysis is performed using commercial software [12]. The algorithm performing calculation takes into account both the material anisotropy and the mixture of flexural and torsional strain. Furthermore it performs a structural-thermal harmonic analysis forcing one mode at a time. The model is built using the coupled-field thermoelastic analysis options of a three-dimensional 20-node solid element. The results convergence is checked against the cut sample mesh density.

This FEM analysis was performed at room temperature and the results are compared with measurements in Figure 5.6. The two graphs refers to the two kinds of central hole investigated on two identical samples (see section 4.2); through (H1) and blind (H2) hole. The agreement is within 10% for most of all modes. These measurements confirm that thermoelastic damping is the main dissipative mechanism at room temperature in the investigated samples.

The thermoelastic dissipation is evaluated using the equation (5.7) and compared with the measured loss angle as a function of temperature in Figure 5.7. [5]

Measurements sweep in the temperature range between 3 and 300 K. To perform the calculations, the appropriate thermo-mechanical properties of silicon are used as in ([5], [6]). For the estimation of silicon specific heat as a function of temperature, the Debye model is used ($T_\theta = 625K$). The modes identified by numbers (4), (11) and (13) (see Table 5.1) are considered in this analysis; they are the ones with the

[5] Here and in the next figures, the temperature shown in abscissa is the inferred sample temperature as a function of the basement temperature, as resulting from experimental measurements of a special cryogenic run, purposely dedicated to thermometers calibration. To this it was used the same silicon wafer (the one with the blind central hole, 0.5 mm thick) used for loss angle cryogenic measurements. A thermometer (LakeShore©, model CX-1050) is fixed close to the edge of the wafer by high conductivity silver glue. An identical thermometer was fixed on the basement close to the wafer holder. The readings of the two thermometers were recorded in the temperature range of interest. Basement temperature was set by a temperature controller with feedback on a thermometer on the edge of basement (see Figure 3.7 in Chapter 2). All sample temperature shown in figures are inferred by this calibration from the reading of the basement temperature.

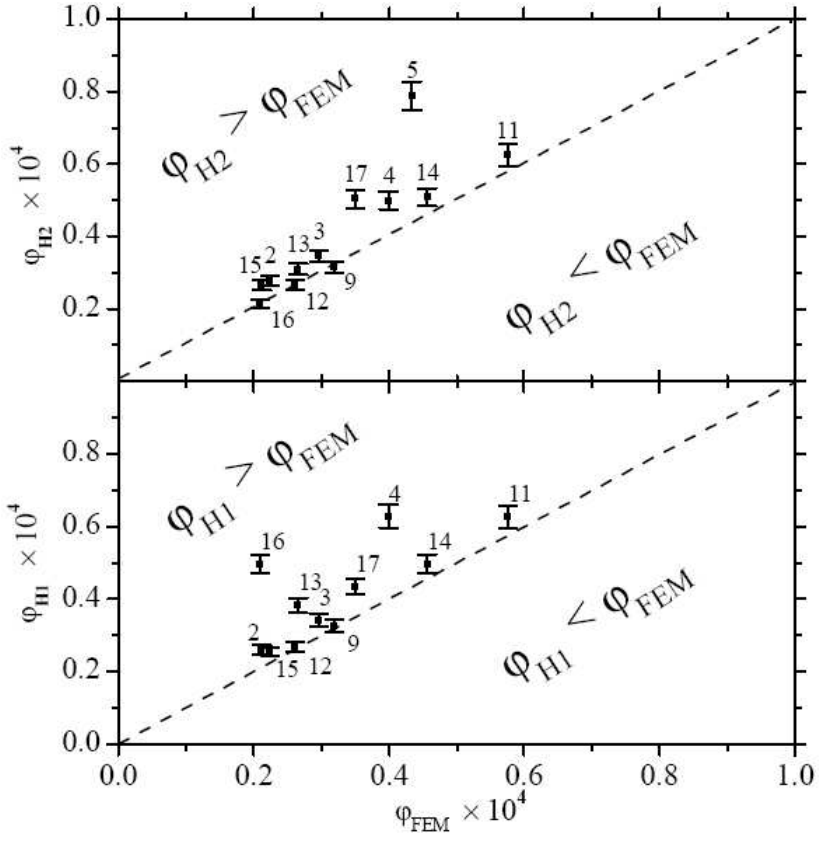

Figure 5.6: **FEM analysis results and experimental measurements comparison.** FEM dissipation predictions are compared with experimental loss angle measurements. ϕ_{H1} and ϕ_{H2} in abscissa are loss angles measured on two silicon wafers (both of thickness 0.5 mm) at room temperature in the two cases of through (H1) and blind (H2) central hole. For the details about the nodal through and blind holes on the wafer see Figure 5.2 (c) and (b), respectively. Loss angle measurements are performed for several different normal modes of the two wafers. The point labels refers to the mode number as listed in Table 5.1. ϕ_{FEM} in ordinate is the dissipation predicted by FEM structural-thermal harmonic analysis described in the text. The dashed lines are the points such that $\phi_{H1,H2} = \phi_{FEM}$. Since the FEM dissipation prediction ϕ_{FEM} is just the thermoelastic damping, measurements below these lines cannot subsist. Measurements on these lines represent pure thermoelastic dissipation.

ID	f [Hz]	C_n
(4)	383	0.32±0.09
(11)	1720	0.47±0.02
(13)	2515	0.99±0.03

Table 5.4: **Thermoelastic estimation.** The constant dimensionless coefficient C_n is the proportionality factor between the thermoelastic damping expression for a cantilever [9] and a thin disk [11, Ch. 6 and therein], as it appears in equation (5.7). C_n here is estimated fitting mode by mode experimental data at high temperature ($T > 180K$); values and errors in the table derive from the best least squares fit. The frequency values refer to room temperature. ID number in the first column refers to complete list of modes in Table 5.1.

smallest measured dissipation. The three wide lines associated with experimental points represent the expected thermoelastic contribution to losses, even if the equation (5.7) is for a thin circular flat plate while the sample under measurements is not. The dimensionless scale factor C_n is evaluated fitting data points at high temperature, where thermoelastic dissipation mechanism dominates over all the others. The results are reported in the following Table 5.4. Model prediction and experimental data agree very well at high temperature (above 120 K), indicating that thermoelastic damping seems the dominant loss mechanism in this temperature range.

The fact that below 120 K the measured loss is larger than those expected from thermoelastic damping, can be due both to the fact that the model itself is inadequate (being valid for circular thin plates, while the samples under measurements are not) and that a different dissipation mechanism dominates at low temperature.

It is worth to remark that at about 120 K the silicon linear expansion coefficient vanishes and so does the thermoelastic damping; hence the local minimum in loss experimental data at this temperature has to be due to other than thermoelastic damping dissipation mechanism. The losses of mode (11) and (13) show similar dependence on temperature, indicating a similar sources for the dominant dissipation mechanism. On the other hand losses of mode (4) show a smoother dependence on temperature, suggesting that this mode is dominated by damping mechanisms different from those of modes (11) and (13).

Lately [12] also FEM model was applied to estimate the thermoelastic damping at a given temperature using the appropriate thermomechanical properties of silicon reported in ([5], [6]) for the same temperature range as above. In Figure 5.8 computed thermoelastic dissi-

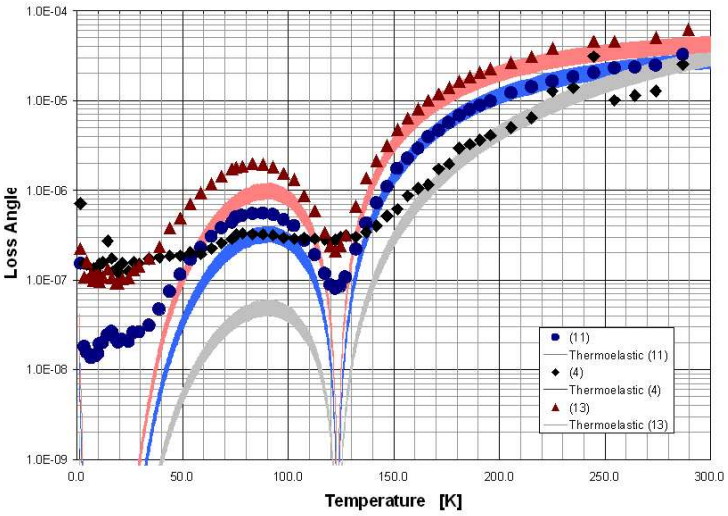

Figure 5.7: **Loss angle measurements.** Measured losses as a function of temperature for modes (4), (11) and (13) (see Table 5.1). The experimental errors are not shown since they are smaller than markers' size. The wide lines associated to experimental points are the dissipation predictions due to thermoelastic damping; the estimation is made using the equation (5.7), even if it is valid for a circular flat plate. The lines thickness accounts for the uncertainty in the prediction coming from uncertainty in the thermal conductivity. All measurements are performed on the silicon wafer with the blind hole (see Figure 5.2).

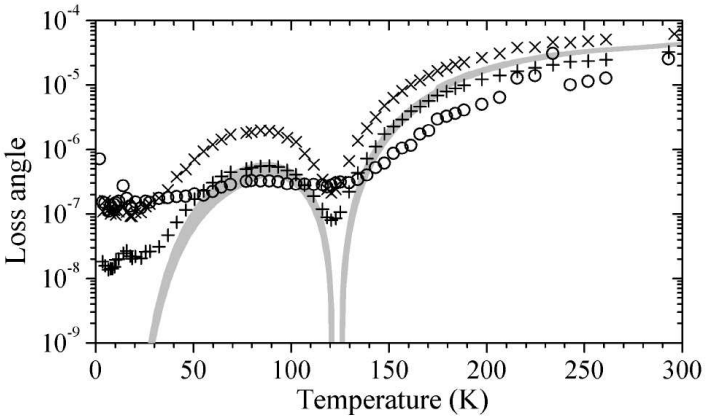

Figure 5.8: **FEM losses prediction.** The loss angle of modes n.4(o), n.11(+) and n.13(×) are displayed as a function of temperature for the sample with blind hole. The experimental errors are not shown since they are smaller than the dimension of the points. In gray the thermoelastic damping FEM predictions are shown for the losses of mode n.9; the line thickness accounts for the uncertainty in this predictions due mainly to uncertainty in the thermal conductivity.

pation is compared with measured loss. The grey line represents the computed thermoelastic loss for mode (11) via FEM analysis. The line thickness accounts for uncertainties in estimations, mainly due to variations in thermal conductivity. Experimental points refers to (4), (11) and (13) modes as labelled in Table 5.1. Overall FEM prediction agrees very well with experimental data above 40K; this seems to indicate that the thermoelastic damping is the dominant loss mechanism above 40 K. Similarly as exposed above, below 40 K the measured loss of mode (11) are larger than those expected from the FEM evaluated thermoelastic damping, indicating again a different dominant dissipation mechanism.

Recently another version of nodal suspension was tested in a cryogenic loss measurement run. We clamped the disk usually by nodal suspension but gluing the bottom sapphire ball in its central hole housing instead of keep the sample between two spheres. The sample used for this experiment was the 0.5 mm thick silicon wafer manufactured with the blind hole described in Figure 5.2 in Chapter 2. A sketching view of the glued suspension and a picture are reported in Figure 5.10.

The sample was read by small area capacitive transducer. The loss angle was measured in the range 5÷120 K; no measurement was possible at higher temperatures because of a breaking occurred during elevator operations. The used glue is commercial Stycast 2850. Glued

nodal suspension should offer some advantages compared to spring one.

- It is less invasive on the sample since it needs only one or even no one hole on the sample.
- No pressure is exerted on sample, at least the one exerted by glue itself when congealed.
- One face of the sample is always free; this is useful for instance if one have to measure the loss of coating layers.
- Thermal conductivity should result increased compared to spring nodal suspension because the glue on the sapphire sphere increases the contact surface on sample.

In Figure 5.9 the results of measurements are reported. Glued and spring nodal suspension measured loss are compared. All measurements are performed with the capacitive readout described in the Chapter 3. It seems that the glue does not increase the loss with respect to spring.

5.8.2 Bonding dissipation.

According to the main goal of the present work, we tried to measure the contribution to silicon losses coming from layers of silicon-onto-silicon bonds. The sample is obtained bonding together three identical cut mono-crystalline silicon wafers. Cut geometry is the same described in the previous section 4.2. The employed technique is the so called "*direct bonding*" and the manufacturing procedure consists in the following steps:

- polish and place the wafers one over the other in vacuum ($P < 10^{-3} mbar$);
- warm up the temperature to 500 C;
- 4 bar pressure applied to substrates for 1h30m;
- post process annealing for 1h30m at 1100 C.

Each single disk has thickness of 0.5 mm and diameter of 4 inch. The sample been under measurement is shown in a picture in Figure 5.11. The three layers are visible on the edge of the sample. It was clamped by glued nodal suspension (described in the previous subsection). This time no hole is manufactured on the wafer surface that appears mirror-polished in both sides. OFHC copper sample holder

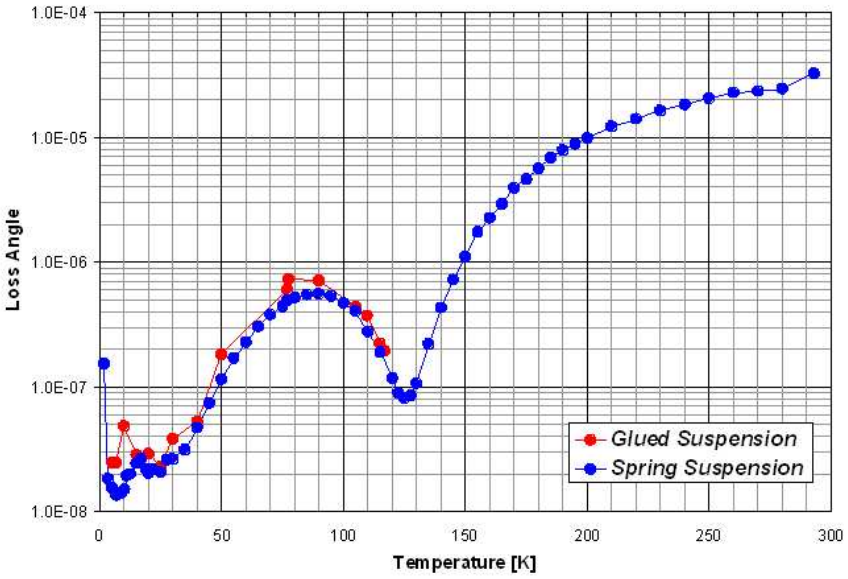

Figure 5.9: **Glued nodal suspension.** Loss is measured as a function of temperature. (Red data) Loss measured on 0.5 mm silicon wafer manufactured with blind squared central hole, and clamped with spring nodal suspension described in section 4.2. (Blue data) Loss measured on the same sample but clamped with glued nodal suspension described in the text (see Figure 5.10 for a picture). Results seem to indicate roughly that glue does not increase mechanical dissipation significatively.

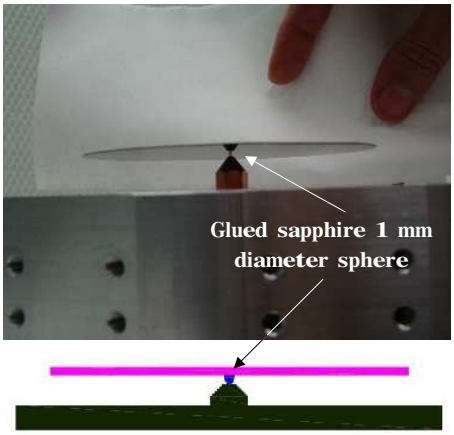

Figure 5.10: **Silicon wafer clamped with glued nodal suspension.** (Above) The silicon wafer is arranged in its location on the aluminium basement. Sample holder with glued sapphire sphere is visible. (Bottom) A sketching view of glued nodal suspension.

was screwed directly on basement. Loss angle was measured over the whole cryogenic temperature range 4÷300 K. Capacitive "multistrip" small area array was employed as readout. In Figure 5.12 measurement results are shown. Measured loss angle is the sum of all loss contributions. A way to infer the contribution to total dissipation due to bond layers is the following.

Bond loss depends on the ratio between the energy E_{bond} stored in the bond layer and the total energy E_{tot} in the body. Let ϕ_{bulk} be the loss of the bulk (non bonded) sample and ϕ_{meas} the measured one (that can also be considered as *total*) of the bonded sample. In the case of a sample bonded by two samples, if the two samples have identical size and if only intrinsic dissipation mechanism be considered, then the total loss ϕ_{meas} can be written as:

$$\phi_{meas} = \phi_{bulk} + \frac{E_{bond}}{E_{tot}}\phi_{bond} \tag{5.8}$$

In the case of multi-layer bonding, let h be the total thickness, t and d the bond layer thickness and its mean distance from the middle plane, respectively (see Figure 5.13 for details about notation). Moreover in equation 5.8, one term $\frac{E_{bond}}{E_{tot}}\phi_{bond}$ should be added to ϕ_{bulk} for each bonding layer in the sample. In the case of samples under measurements, if the bonding layer is thin, if the bulk and the bond material

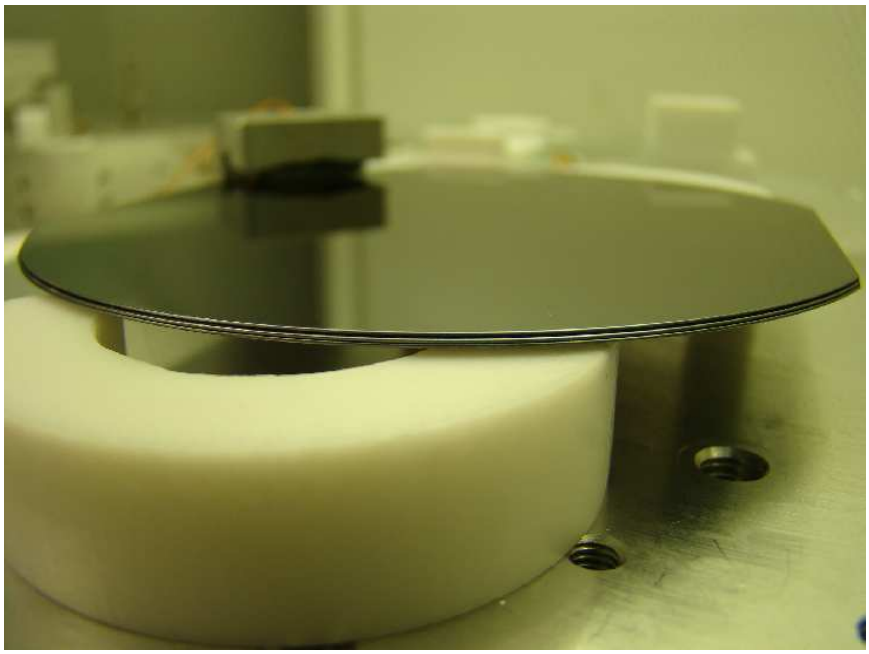

Figure 5.11: **Three direct bonded silicon wafers.** Sample used to measure the contribution of silicon bonding layers to total dissipation. The sample is obtained bonding together three silicon disks with the so called "*direct bonding*" technique. Glued nodal suspension is used. The small area capacitive "multistrip" array is visible blurred in the background.

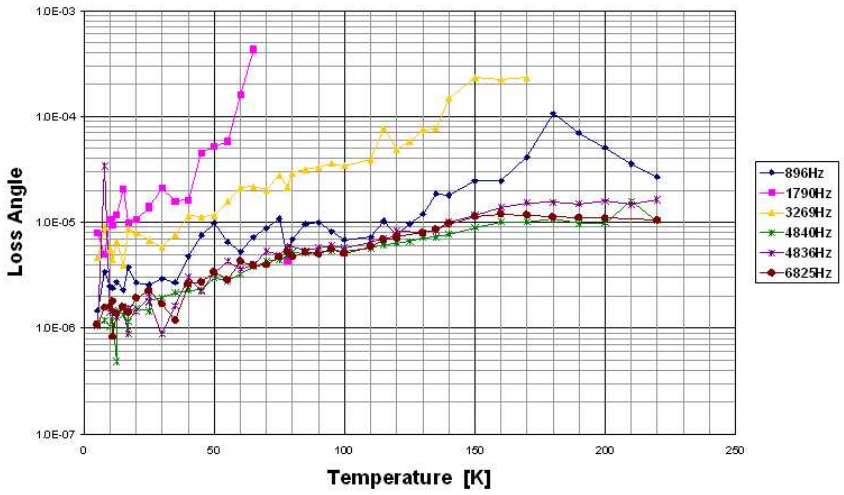

Figure 5.12: **Measurements on bonded wafer.** The figure collects all measurements performed on a bonded silicon wafers. Different modes are identified by resonant frequency.

have both isotropic physical properties and if they have both the same Poisson ratio, then the energy ratio can be written as [12]

$$\frac{E_{bond}}{E_{tot}} \simeq \frac{6}{h^3}\frac{Y^{bond}}{Y^{bulk}}\left(d^2t + \frac{t^3}{12}\right) \simeq 6\frac{Y^{bond}}{Y^{bulk}}\frac{d^2t}{h^3}. \tag{5.9}$$

The last approximation is due to the fact that typically it is $t \sim 100$nm and $d \sim 100\mu$m. A rough evaluation of the ratio (5.9) can be made assuming that

- $\phi_{bulk}(\omega) \ll \frac{E_{bond}}{E_{tot}}\phi_{bond}(\omega), \quad \forall\omega$;
- $Y_{bond} = Y_{bulk}$;
- $t \approx 80nm$ (this values comes from experimental measurements in [13]).

In the case of the sample under measurement, we have $d = 0.15$ mm and $h = 0.9$ mm. Then the ratio (5.9) results in

$$\frac{E_{bond}}{E_{tot}} \simeq \frac{6}{h^3}\left(d^2t + \frac{t^3}{12}\right) \simeq 6 \times 10^{-5}. \tag{5.10}$$

This means that approximately we have $\phi_{bond} \approx 1.7 \times 10^4 \phi_{meas}$. Starting from data collected in Figure 5.12, one can rescale values mode by

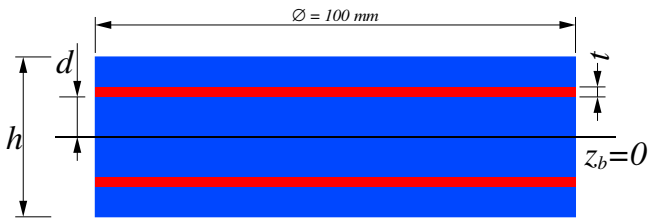

Figure 5.13: **Bonding layers scheme.** In the figure it is shown the notation used in the text about the case of two bonding layers. The bulk material is coloured in blue while the two bonding layers in red. Both the layers have thickness t. Total sample thickness is h, diameter $\phi = 100mm$. Diameter value does not account for the two symmetric cuts but refers to the disk circumference. In the middle the neutral plane is showed as a continuous line. d is the mean distance between the bond layer and the middle plane. In the case of our sample, dimensions are the following: $h = 900$ μm, $t \sim 80$ nm, $\phi = 100$ mm, $d = 0.15$ mm.

mode to obtain roughly estimated loss contribution of the two bonding layers to total dissipation. In Figure 5.14 experimetal data of Figure 5.12 are rescaled in such this way and reported as a function of temperature.

The Equation (5.9) can be used to estimate the minimum ϕ_{bond} that the experimental apparatus is sensitive to. The minimum sensitive loss is here computed as the minimum difference in the total losses that can be observed comparing bulk and bonded samples, both with the same overall dimensions, provided that the whole difference is due to bonding layers dissipation. Let $\sigma(\omega, T)$ be the standard deviation of loss measurement at the temperature T for a given normal mode. Then, in order to be measurable with a confidence level of 99.73%, the minimum detectable bond loss – the second term in right hand side of eq. (5.8) – cannot be larger than $\sigma(\omega, T)$. Hence the minimum detectable bond loss can be written as

$$\phi_{bond}(\omega, T) \gtrsim \frac{E_{tot}}{E_{bond}} 3\sigma(\omega, T). \tag{5.11}$$

In our case, the bonded sample is composed by three identical slices in stack. This means that $d \sim \pm h/6$. On the other hand the bonding layer is very thin, so it is $t \ll h$. Expressing energy ratio using the eq. (5.9), the minimum loss of previous eq. (5.11) can be written as

$$\phi_{bond}(\omega, T) \gtrsim 4.5 \frac{Y_{bulk}}{Y_{bond}} \frac{h}{t} \sigma(\omega, T). \tag{5.12}$$

Estimation of loss measurement standard deviation is a ticklish question we deal with in the followings. Some information on σ was experimentally checked out for mode (11) (see Table 5.1).

- Measurements are well reproducible (within 10%) at room temperature and at 77K, where the dominating dissipation mechanism is the thermoelastic damping. This reproducibility accounts for the case that the sample is removed and replaced back in its set-up, and even the case that measurements are repeated over a full thermal cycle to 4K. Measurements indicate that the loss angle standard deviation for mode (11) is
  - $\sigma(2\pi\nu, 300K) = 1 \times 10^{-6}$, $\nu = 1721$ Hz, room temperature;
  - $\sigma(2\pi\nu, 77K) = 5 \times 10^{-8}$, $\nu = 1729$ Hz, liquid nitrogen temperature.
- At liquid helium temperature (4K) measurements are less reproducible. The standard deviation results to be $\sigma(2\pi\nu, 4K) = 1 \times 10^{-8}$. Again this reproducibility accounts for both the cases of removing and replacing back the sample and of a full thermal cycle.

Spiel and collaborators [14] found that reproducibility in dissipation measurements is associated with clamping losses. In our case, clamping loss should be one of the dominant dissipation mechanisms at 4K for the mode (11).

It is worth to remark that the reproducibility σ reported here is larger than the error deriving from the exponential decay fit of experimental data, usually reported in literature as the error in measured losses. Furthermore reproducibility of measured loss, if estimated simply as the standard deviation of consecutive repeated measurements at a fixed temperature, results smaller than σ estimated in the sense described above.

The experimental apparatus sensitivity can be evaluated considering mode by mode the reproducibility σ in the case of the specific sample under measurement, whose the geometry is displayed in Figure 5.13. For the mode n. (11) considered above, it results that our set-up is sensitive to:

- $\phi_{bond,T_{amb}} \gtrsim 5 \times 10^{-1}$ at room temperature (300K);
- $\phi_{bond,77K} \gtrsim 3 \times 10^{-2}$ at liquid Nitrogen temperature;
- $\phi_{bond,4K} \gtrsim 5 \times 10^{-3}$ at liquid Helium temperature.

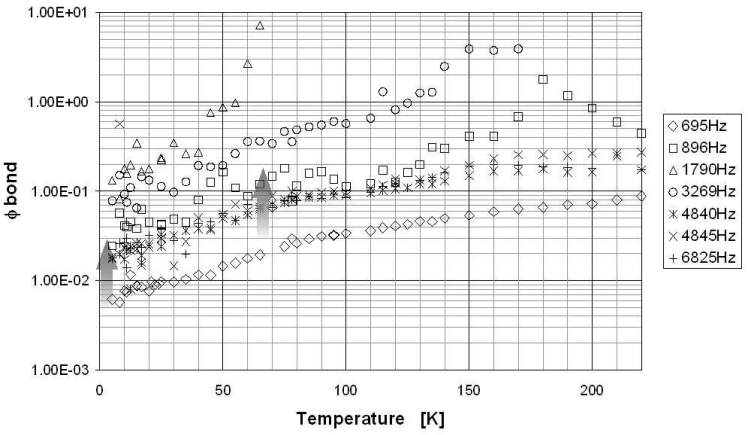

Figure 5.14: **Bonding dissipation as a function of temperature.** Bonding losses are reported mode by mode as a function of temperature. The loss values are inferred from the total loss measured (shown in Figure 5.12) using the equation 5.10 and the dimensions of the bonded sample as described in the text. The two grey arrows display the experimental set-up sensitivity to bonding loss as estimated in the text for T = 4K and T = 77K. The set-up sensitivity is indicated by the bottom of each arrows, so that the arrows bodies indicate the region of the graph where our experimental set-up is sensitive.

Bonding losses reported in Figure 5.14 are inferred from the total loss measured (see figure 5.12) using the eq. (5.10). Almost all the values resulting are compatible with the above estimated apparatus sensitivity at the corresponding temperature, provided that the reproducibility of all modes were roughly similar to that of the mode (11). If not the case, data should be checked mode by mode evaluating reproducibility and sensitivity over the whole temperature range of measurements. Anyway the loss angle measurements reported in Figure 5.14 stand for an upper limit for losses of bonding.

5.9 External losses.

5.9.1 Gas damping.

The residual gas present in the experimental vacuum chamber that houses the samples constitutes an external source of losses. All loss angle measurements presented in this thesis are performed in free-molecules regime (measured pressure $P \leq 10^{-6}$ mbar almost always).

In this regime, the momentum transfer from the vibrating plate to the surrounding gas due to the collisions between the plate and the molecules of the gas generates the dissipation. Christian's models [21] assumes a Maxwell-Boltzmann distribution for the gas velocity and predicts a limit to the measured loss angle given by:

$$\phi_{GD} = \left(\frac{2}{\pi}\right)^{3/2} \frac{1}{\rho h \nu_m} \sqrt{\frac{M_g}{RT}} P \propto \frac{P_{[mbar]}}{\nu_{[Hz]}\sqrt{T_{[K]}}} \tag{5.13}$$

where R is the gas constant, M_g the molar mass of the residual gas, P the pressure in mbar, ν_m the oscillation frequency in Hz, T the temperature in K, ρ the density, h the sample thickness. Length and mass units of ρ, h, R and M_g must agree. In order to estimate the gas damping at 4K, let consider helium to be the largest component of the residual gas since liquid helium is employed for the TF thermal bath. For $T = 4.2$K, $P = 10^{-6}$ mbar it results $\phi_{gas} = 1 \times 10^{-9}$ for mode (4) and $\phi_{gas} = 3 \times 10^{-10}$ for mode (11).

Christian's model [21] assumes that the sample is placed in an infinitely large volume. But if the distance d between the walls and the sample becomes smaller than the typical dimension L of the oscillating body, then a larger number of collision should be expected and hence the damping mechanism should be more efficient. This condition is the case of the so called "*squeezed-film*" regime. Bao *et al.* [22] found that for a rectangular plate in this regime, the damping can be expressed as:

$$\phi_{SGD} = \phi_{GD} \frac{L}{16\pi d} \tag{5.14}$$

the effective loss due to this damping mechanism can be evaluated in the case of the sample measured by capacitive readout. Considering the case of large area multistrip sensor, putting $d \sim 0.08$ mm (the gap between the electrodes and the sample) and $L \sim 25$ mm [6] (the effective length of the sensor) we calculate $\phi_{SGD} \sim 6.2\phi_{GD}$. Considering the case of small area multistrip sensor, the only parameter that changes is $L \sim$ 10 mm, and we obtain $\phi_{SGD} \sim 2.5\phi_{SG}$. For thermal conditions of T = 4.2K and $P = 10^{-6}$ mbar, expected losses are summarized in Table 5.5.

The estimates of the damping from the residual gas at 4K for modes (4) and (11) are about a factor 10 smaller than experimental measurements (see for instance Figure 5.7). This fact suggests a negligible contribute from gas damping to total measured loss. On the other hand, it should be noted that the above estimates should be refined

[6] We consider just half the whole length of the array because, due to practical experimental reasons, about half of the electrodes were effectively faced to the sample.

	Christian model	Bao model	
mode	ϕ_{GD}	Large Area	Small Area
(4)	1×10^{-9}	6×10^{-9}	3×10^{-9}
(11)	3×10^{-10}	2×10^{-9}	8×10^{-9}

Table 5.5: **Gas damping prediction.** Table summarizes the predictions on gas damping loss angle according Christian's [21] and Bao's [22] model. Note that Christian's model does not account for sensor dimensions and gap, while Bao's does. Bao's model is evaluated both for large and small area capacitive readout. Predicted loss angle is evaluated for the modes (4) and (11).

taking into account for some more parameter, for example the real geometry of readout and sample, the different modal shapes and the surface outgassing. Moreover, the measured IVC residual gas pressure could be underestimated because the pressure sensor is placed high on TF top at room temperature near the turbo molecular pump; as a consequence, being proportional to the pressure, the estimation of gas damping dissipation can be affected by a systematic error.

We performed loss angle measurements at 77 K on the silicon wafer with through hole (thickness 0.5 mm) as a function of pressure in the IVC chamber for the modes (4), (11) and (18) in Table 5.1. Measurements are reported in Figure 5.15. Modes (11) and (18) follow a linear trend in loss angle as function of pressure as predicted in equation (5.14); on the contrary, mode (4) does not. This seems to suggest that at 77K the gas damping is negligible below 10^{-4}mbar for frequencies $\geq$1.7KhZ (modes (11) and (18)). Mode (4), resonating at lower frequency, shows a non linear dependence of the loss angle on the residual pressure even in the 10^{-6}mbar range, where most of the performed measurements are. Mode (4) data seem to follow a power law trend.

We also repeated the measurements at 77K of the loss angle of the mode (4) as a function of pressure in the range $0.006 \div 0.03$ mbar and at 10^{-6} mbar, but on the sample with the blind central hole read by the laser beam deflection sensor. Since no small gap is present on the sample, this readout should not suffer from the squeezed-film damping. Above 6×10^{-3}mbar the losses measured with the optical readout are about a factor 0.2 smaller than the isobar measurements taken with the capacitive readout. This seems to suggest in the latter a significant contribution from the squeezed-film dissipation mechanism. On the other hand, at 77K the mode (4) loss angles measured at 10^{-6} mbar with both sensors (and on two identical samples except for the central hole) differ by less than 30% and amount to about 2.5×10^{-7}.

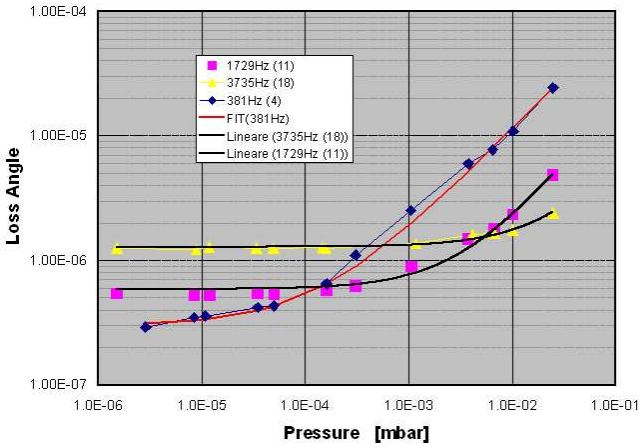

Figure 5.15: **Loss angle as a function of pressure.** Loss angle is measured as a function of the residual gas pressure for the modes (4), (11) and (18). The measurements are performed at 77K with the capacitive multistrip displacement sensor.

As a consequence of this observation we can rule out the squeezed-film damping as the dominant contribution even for the mode (4). To establish surely the size of the gas damping effect at 4K too, a similar experimental campaign should be repeated at that temperature. However on the basis of the above estimates we expect not a larger effect.

5.9.2 Clamping losses

A rough estimation of the interaction between each acoustic mode and the holder can be quantified considering the elastic energy dissipated by the holder in its moving. The holder displacement can be induced by a not perfect nodal suspension or by a change in the thickness h of the wafer where it is in contact with the sapphire ball. A reliable FE model of the complete system cannot be developed, due to the presence of pressed contacts and springs. Then for each mode the quality of the nodal suspension can be estimated by the evaluation of the maximum thickness change during one period induced when only one face of the disk is constrained in its clamped central area. In the FE model, the surface of the wafer is constrained on one side over a circular area of diameter 0.3 mm. The displacement of the points along the wafer symmetry axis is constrained along the z-axis, in order to avoid rocking movements. The convergence of the results was checked

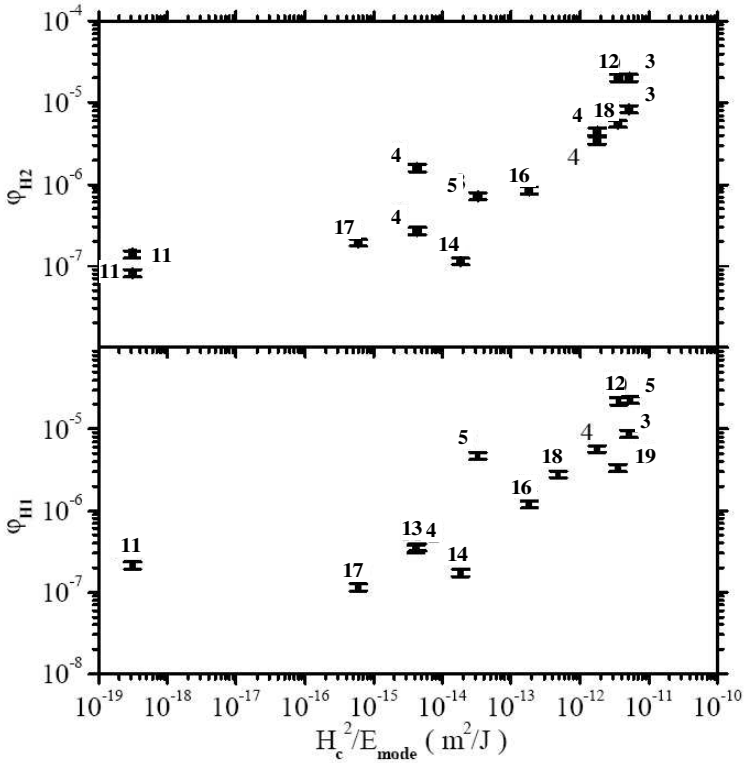

Figure 5.16: Loss angle at the temperature of 121K as a function of the normalized squared thickness change at the center of the wafer, H_c^2/E_{mode}. The experimental data refer to the sample with through hole (bottom plot, H1) and blind hole (top plot, H2). Since thermoelastic loss is negligible at this temperature, the effect of the holder dissipation is seen as a monotone trend with respect to H_c^2/E_{mode}. The label close to the points refer to the mode labels reported in Table 5.1.

against the mesh density. In order to catch reliably second order effects, the clamped central area of the disk is thickened with 2000 elements, against total 16500 elements the whole mesh consists of.

With this model a number of harmonic analysis were performed, forcing one mode at a time and measuring the *rms* value H_c of the displacement of the 0.3 mm diameter central circular area on the free side of the plate (where the clamping sapphire sphere is placed in the real experimental configuration).

In Figure 5.16 measured mode losses are plotted against the square of computed thickness change normalized to the mode energy E_{mode}. This quantity represents an estimation of the interaction between the

wafer and the holder. The loss measurements were performed for both samples with through (H1) and blind (H2) holes at 121K. At this temperature the coefficient of linear expansion vanishes, as a consequence the thermoelastic damping is negligible and it is possible to estimate clamping loss arising from the dominant loss contribution. As expected, lower losses are measured for the modes that induce little thickness variation in correspondence of the holder. The trend in the plot seems to suggest that holder loss dominate at this temperature except for the lowest loss mode (mode 11 in Table 5.1). For few modes two different measurements are shown. They are taken on the same oscillator with the two different readout available (optical and capacitive), in two different runs, after that the samples were removed and replaced back in the experimental apparatus. This can be considered as a test of reproducibility of the measurements at a frequency where the thermoelastic damping is negligible. Figure 5.16 also shows that no differences are measured in the losses between the samples with different clamping holes.

The FEM analysis of the two modes (4,0,+) and (4,0,×) shows some details about the deformation in the central area where the sample in clamped. This clamping area results much more deformed by the mode motion in the mode 12 than in the mode 11. This seems to indicate that the former is more subject to clamping loss then the latter. This agrees with the large difference in their loss angles observed at 121K, respectively 2.0×10^{-5} and 8.2×10^{-8}.

It is interesting to remark also that clamping loss is temperature dependent. This is shown by the variation of the measured loss angle with temperature of the mode 12, which is dominated by clamping loss. In fact for this mode it was measured $\phi = 1.5 \times 10^{-4}$ at 300K and $\phi = 2.0 \times 10^{-5}$ at 121K.

Bibliography

Bibliography for Charter 5.

[1] K.Numata, G.B.Bianc, M.Tanaka, S.Otsuka, K.Kawabe, M.Ando and K.Tsubono, Phys. Lett. A 284, **162** (2001)

[2] K.Numata *et al.*, Phys. Lett. A **276** (2000), p.37-46

[3] D.F.McGuigan *et al.*, J. Low Temp. Phys. 30 **621** (1978)

[4] D.H.Gwo, *Ultra-precision and reliable bonding methods*, U.S. patent 6284085 (2001)

[5] Material Properties Database (MPDB), http://www.jahm.com

[6] J.C.Thompson, B.A.Younglove, J. Phys. Chem. Solids **20**, 146 (1961)

[7] J.J.Wortman and R.A. Evans, J. Appl. Phys. **36**, 153 (1965)

[8] Ron Lifshitz and M.L.Roukes, *Thermoelastic damping in micro- and nano-mechanical systems*, Phys. Rev. B, Vol. 61, N. 8, 5600-5609 (2000)

[9] C. Zener, Phys. Rev. **52**, 230 (1937); **53**, 90 (1938); C. Zener, W. Otis and R. Nuckolls, *ibid.*, **53**, 100 (1938)

[10] A.S.Nowick and B.S.Berry, *Anelastic relaxation in crystalline solids*, Academic Press, New York, 1972.

[11] D.G.Blair, *The detection of gravitational waves*, 1988

[12] M.Bonaldi *et al.*, *Loss budget of a setup for measuring mechanical dissipations of silicon wafers between 300K and 4K*, article in preparation.

[13] J.Hough *et al.*, Class. Quant. Grav. **20**, 5025 (2003)

[14] C.L.Spiel, R.O.Phol and A.T.Zehnder, Sev. Sci. Instrum. **72**, 1482 (2001)

[15] X.Liu, J.F.Vignola, H.J.Simpson, B.R.Lemon, B.H.Houston and D.M. Photiadis, J. Appl. Phys. **97**, 023524 (2005)

[16] H.J.Mamin and D.Rugar, Appl. Phys. Lett. **79**, 3358 (2001)

[17] U.Gysin *et al.*, Phys. Rev. B **69**, 045403 (2004)

[18] K.Wago *et al.*, J. Vac. Sci. Technol. B **14**, 1197 (1996)

[19] R.E.Mihailovich and J.M.Parpia, Phys. Rev. Lett. **68**, 3052 (1992)

[20] A.Zimmer, R.Nawrodt *et al.*, arXiv:0709.2124v1

[21] R.G.Christian, Vacuum **16**, 175 (1966)

[22] M.Bao *et al.*, J. Micromech. And Microeng., **12**, 341 (2002)

Chapter 6

Silicon Carbide.

6.1 Introduction.

Silicon Carbide (SiC) is today largely employed in industrial processes and in space technology. Inside gravitational wave (gw) physics research field, it is employed for instance to manufacture mirror supports for gw interferometers. As candidate material for the test mass of DUAL detector (and more in general for next generation acoustic detectors of gravitational waves), SiC shows some interesting physical properties.

SiC is characterized by high cross section towards an impinging gw, since it has an high value of the ratio Y^2/ρ, Y being the Young's modulus and ρ the density. In Table 1.1 a number of different materials are considered and relative detector sensitivities are compared. It is worth to note as the sensitivity of a SiC detector is the second after diamond.

In particular infiltrated SiC offers the possibility to be manufactured in bodies of large size. That is crucial to achieve high sensitivity and wide bandwidth, fulfilling the expected curve showed in Chapter 1.

SiC shows a value of thermal conductivity high enough to allow cryogenic cooling without problems. This property could become very important in the case that detector needs to operate at cryogenic temperature.

Finally, the cost is reasonably acceptable to machine a resonator of large size.

Many kinds of SiC are available and their respective physical properties spread between each other. For instance, always referring to table 1.1, the value 10 refers to infiltrate while 27 to sintered SiC. SiC physical properties vary also with different employed production and postproduction processes.

Table 6.1: Cell parameters for some polytypes of SiC.

	Cell parameters (A)	
polytype	a	c
3C	4.36	–
2H	3.08	5.05
4H	3.07	10.05
6H	3.08	15.12
15R	12.691	

In this Chapter, after a brief overview on the crystalline structure, different poly-types and production processes, measurements on infiltrated, sintered and mono-crystalline SiC mechanical losses are reported over 3÷300 K range, in order to evaluate the possibility of a SiC made DUAL detector.

6.2 Silicon Carbide.

Silicon Carbide has chemical formula SiC, with 70% of Silicon and 30% of Carbon in mass ratio. SiC molecule is part of covalent compounds; C atom binds Si atoms with covalent bounds like as in diamond. SiC crystal however differs from diamond because of its lower hardness, due to silicon atomic radius (1.11 A) longer than carbon one (0.77 A). The primitive cell of mono-crystal SiC structure is a tetrahedron with four silicon atoms and a single carbon atom in centre. Each carbon atom is bound to four silicon ones. The distance between two silicon atoms (labelled a) is about 3.08 A, while the one between the central carbon and the silicon atom (labelled c) is about 1.89 A. this values are indicative because several poli-types of SiC exist. In Table 6.1 distance values for some SiC types are collected.

6.2.1 SiC polytypism.

There are an infinite number of ways to arrange identical spheres in a regular array maximizing the packing fraction. In the case of SiC, one is the hexagonal close-packed structure (hcp) [1]. Atoms are arranged in layers labelled with capital letters $A, B, C, \ldots$. In the first layer A, spheres are closest-packed by placing each one in contact with six others (see Figure 6.1). This layer may serve as either the basal plane of an hcp structure or the (111) plane of the face cubic centred (fcc) structure. A second similar layer B may be added placing each sphere of B in contact with three spheres of bottom layer A. A third layer

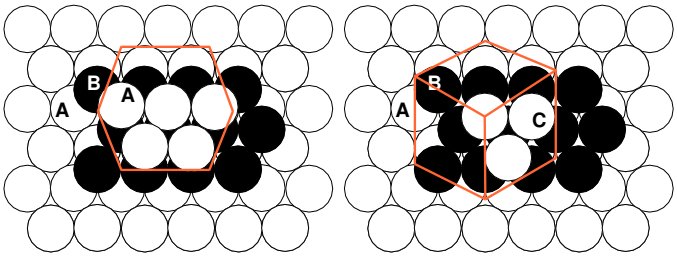

Figure 6.1: **Polytypism.** Figure shows two examples of ways to arrange atoms in layers maximizing the packing fraction. Left: the sequence $ABAABA\ldots$ gives origin to hexagonal structure. Right: the sequence $ABCABC\ldots$ generates the fcc structure.

C may be added in two ways. If the spheres of the third layer are added over the holes of the first layer A left free by the spheres of B, then the fcc structure results (see Figure 6.1, right). The hcp structure results instead when the spheres in the third layer are placed directly over the centres of the spheres in the first layer A (see Figure 6.1, left). Structures differ in the stacking sequence of the planes. For instance, fcc has the sequence $ABCABC\ldots$ and hcp $ABABAB\ldots$.

Polytypism is characterized by a stacking sequence with a long repeat unit along the stacking axis. SiC is a good example with more than 170 stacking sequences of the close-packed layers. Within the notation adopted in the followings, capital letters indicate the type of structure (for instance C states for cubic, H for hexagonal and so on) and the number before tells how many layers the repeat unit is made of. In Figure 6.2 (right) the structure of 6H-SiC is shown as an example. Letters h and k state for two non-equivalent Si-C layers which differ from the relative arrangement. It is possible, for instance, to end a surface with Si or C atoms; this determines different reaction properties in the surface.

There are 4 main polytypes of SiC. The 4H and 6H SiC are also called α-SiC. The two polytypes 3C(I) and 3C(II) are also named β-SiC. Polytypes of SiC considered in the present work are 4H, 6H, 3C.

6.3 SiC production processes.

Several processes are been developed for SiC production, mainly in industry. In the followings, some of them are briefly described.

Chemical Vapour Deposition (CVD). A gas (called "precursor") reacts with a heated surface of a solid that acts as a condensing

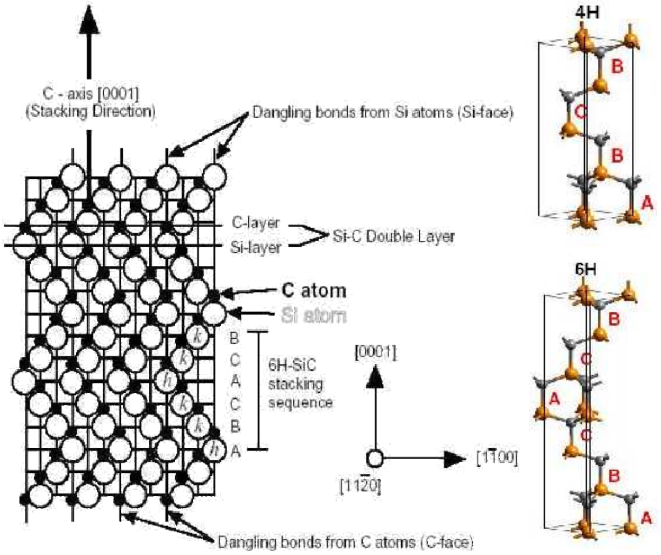

Figure 6.2: (Left) Sketching view of 6H-SiC section along the stacking direction. (Right) 4H-SiC (top) and 6H-SiC (bottom) cell structure.

core, and settles forming a SiC conglomerate. The seed on which SiC settles often is graphite, but may also be silicon, silicon oxide or silicon carbide itself. The choice of seed-solid is very important because the settling material tends to preserve its crystalline structure; this property allows inducing the desired crystalline structure within the process. Since the production of 3C-SiC is energetically favourite, it is common to have the presence of 3C inside a 4H or 6H -SiC crystal as the result of impurities in the seed or gradients in the deposition temperature [2]. By CVD process only samples of small size are available, as for instance 5 cm diameter wafer. Final conglomerates may be mono-crystalline, poli-crystalline or amorphous, depending on the employed temperature and specific process [3]. CVD technique allows obtaining final conglomerates with 99.9995% of purity in mass, better than by other techniques, for instance sintered. Unfortunately, today is still impossible obtaining objects of size large enough to build the resonator mass for a gw detector.

Chemical Vapour Reaction (CVR) This method is similar to CVD. Active Silicon gas is employed as reactant at high temperatur with a carbon spongy body. the final sintered SiC results free of non-bound carbon, differently from CVD in which the seed-solid

remains unchanged. Silicon carbide produced using this technique is also called "foamed" SiC.

Sintered SiC. Silicon Carbide produced by this process is also called (S)SiC. The technique consists in an isostatic pressing at low temperature of SiC particles with diameter less than 1 micron, giving rise to a condensate. Afterwards it is annealed up to 2000÷2500 °C and the sintering occurs. Boron or carbon ban be added to the SiC powder in order to increase the sintered density. The so obtained sintered SiC density is about 98% of the theoretical density of mono-crystalline SiC. Density can be increased filling the porosities by the CVD SiC technique described above. Usually this is done to manufacture mirrors, because in this way optical properties are enhanced.

Reaction Bonded SiC. Reaction bonding is a particular sintering technique. First a mixture is made of SiC powders, water and binding agents. Then the pulp so obtained is put in a mould and, via a lyophilising process, water is dried out. This sintering process gives rise to a α-SiC porous solid body. Porosities are filled with fused silicon in a second time by another process at high temperature. Reaction bonded SiC finally obtained is characterized by full density (100%). However non-bound silicon is often present from 10% to 30%.

Hot pressing SiC. In this process, SiC powders undergo high temperature and pressure, giving rise to a monolithic body. The result is a sintered SiC characterized by high density, similar to the single crystal one. Possible residual porosities can be filled by CVD process.

Infiltrated SiC (or C/SiC). This process starts from a body made of isotropically oriented short carbon fibres. Within high-pressure environment, phenol glue is added to the body. Then the glue dries within a high temperature environment. The resulting solid is commonly called "green body". It is easy to be machined in the desired shape. The shape of the green body will be the shape of the final SiC object. In fact, the green body is placed in a vacuum oven with silicon; as the temperature reaches the silicon melting point, liquid silicon fills the porosities of the green body, reacts with its fibres and gives rise to SiC. With this technique, the inner part of the carbon fibre does not react with silicon; on the contrary, outside the fibres, we found free silicon, i.e. non-bound to carbon. Hence a stoichiometric ratio between silicon and

carbon can be defined only on the fibre's surface. The notation C/SiC stands for the fact that the transformation of silicon and carbon in SiC is not complete. Maybe the main advantage of this process is that objects of various and complex shape can be carried out, and, first of all, also objects of very large size. Large size in the final SiC object is assured by bonding processes on the green body. Limits in size are imposed just by the size of the oven.

6.4 Samples.

The loss angle measurements presented in this work were performed on SiC samples different each from other in material production process, composition and shape. Different investigated samples of SiC were

- sintered SiC, α phase, beam shape, produced in Italy by Bettini;
- infiltrated SiC (or C/SiC), both beam and disk shape, produced in Germany by ECM and patented as *Cesic*©. All disks are flat and circular, without cuts.
- two mono-crystalline SiC, β phase, disk shape, produced in USA by CREE in two different polytypes 4H and 6H. Both disks present two symmetric cuts, quite identical to those of silicon plates already described in Chapter 4.

In Table 6.2 the characteristics of all SiC samples measured are reported.

6.5 Suspensions.

All the beam samples (identified as Cant 1,...,4) are clamped by an edge. A sketching view of the cantilever suspension is shown in Figure 6.3. An edge of the cantilever is clamped by a 4 screws clamping-block. Typically screws are fixed with $1 \div 3$ Nm (from thinner to thicker width). The other edge is free to vibrate and is equipped with the readout, which can be optical or capacitive and will be described in the next section.

All the SiC disks are clamped by the same nodal suspension described previously in chapter 4, in the case of silicon plates. Disks 1, 2 and 3 are suspended by the system with the steel spring. The sample is clamped on its centre with steel and sapphire spheres, respectively on top and bottom plane. Two notches (about 0.5 mm in diameter) are

Table 6.2: **SiC Samples.** Silicon carbide characteristics for all samples are reported. Columns: (h) thickness [mm]; (L/R) Length for cantileves and radius for disks [mm]; (W) Width, for cantilevers only [mm]; (ν) resonance frequency for investigated modes [Hz]. In the case of cantilever 1, its section is larger on one edge in order to be clamped there: the reported length refers to the oscillating part only. No many frequencies are reported for disk 3 because unfortunately a trouble in its signal line makes any measurement impossible.

Sample	h	L/R	W	ν	Material
Cant 1	0.3	50	10	2392(a)	Sintered Bettini SiC
Cant 2	0.5	85	10		Sintered Bettini SiC
Cant 3	3.0	65	10	1545(a)	Infiltrated Cesic SiC
Cant 4	5.0	85	10	1011	Infiltrated Cesic SiC
Disk 1	1.0	26.2	–	2067	Infiltrated Cesic SiC
				2070	
				7947	
				7950	
Disk 2	2.0	26.2	–	3470	Infiltrated Cesic SiC
				3473	
				7947	
				7950	
Disk 3	3.0	26.2	–	5237	Infiltrated Cesic SiC
Disk 4	0.3	50.0	–	4980	Mono-Crystalline CREE 4H SiC
Disk 5	0.3	50.0	–	5210	Mono-Crystalline CREE 6H SiC

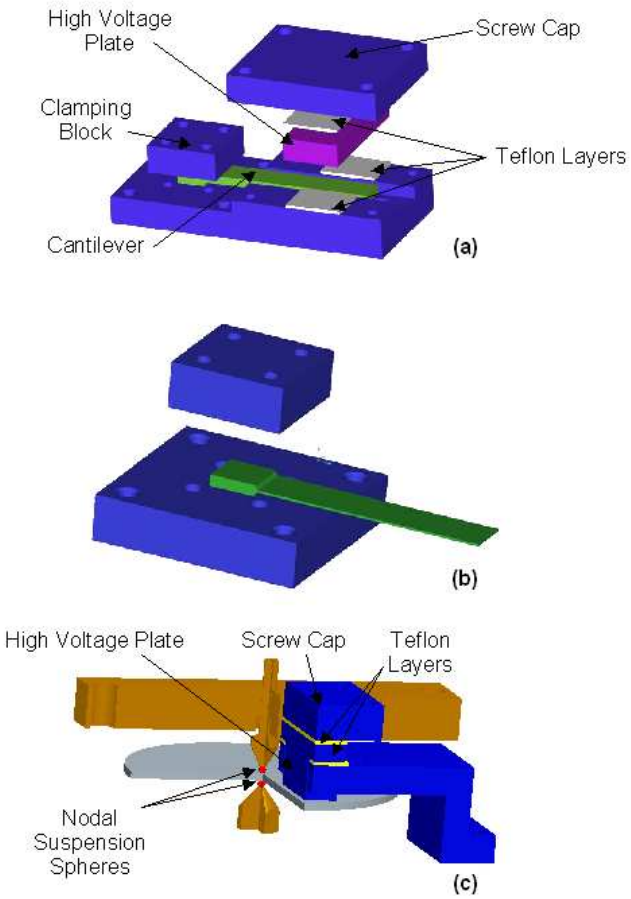

Figure 6.3: **Employed suspensions assembled on respective samples**. (a) Suspension for cantilever with the capacitive readout. (b) Suspension for cantilever to be readout by optical lever. (c) Nodal suspension for disks. The capacitive readout for conductors is shown. Nodal suspension spheres are visible.

dug on the central point on both disks surfaces where the steel spheres are housed in. Steel spheres are needed in order to ground the sample and to read its displacement by capacitive readout, since SiC is a good electric conductor. In the first performed run, no glue is employed in nodal suspension. In a second run, disk 1 (with a larger carbon matrix) is clamped by glued nodal suspension.

Instead disks 4 and 5 are clamped by nodal suspension without spring but gluing the sapphire sphere directly on the central nodal point on the bottom surface of the disks. No notches are digged on the disks 4 and 5 on the contact point with the suspension sphere. On the other side, the sapphire ball is glued also on the lower holder, in its turn screwed directly on the basement. Employed glue is commercial Stycast©. Some details are shown in Figure 6.13.

6.6 Readouts.

All cantilevers and the disks 1, 2 and 3 are equipped by a "classical" capacitive displacement readout, since both sintered and infiltrated SiC are electrical conductors. In this scheme, the sample is the grounded plate of a plain capacitor; the signal is generated by the variation in the gap between it and a high voltage plate. Typically gap values span within $50 \div 100$ μm. The electrical scheme employed for these samples is identical to that reported in Chapter 4 in the case of silicon plates, provided that the "multistrip" array is to be substituted by the plain capacitor described here. In Figure 6.3 a scheme of the device is reported for cantilevers and disk.

Disks 4 and 5 are instead equipped with the small area "multistrip" capacitive readout, previously described in Chapter 3 and, in the case of silicon plates, in Chapter 4. In fact, both 4H and 6H SiC are dielectrics. The electrical scheme is again the same as that described in Chapter 4. The gap is about 75μm for both samples. The whole sensitive area of the array is faced to the sample.

An optical readout was employed too on Cantilever 1 and 2. The readout is based on the optical lever principle and it was yet described in Chapter 4 in the case of silicon.

6.7 Sintered SiC measurement results.

We measured losses of sintered silicon carbide only on cantilevers 1 and 2 (see Table 6.2 for details). Samples are provided for the Bettini company, from Italy. All measurements reported here and in the followings

are performed by the ring down method already described in the previous Chapter 4. Measurements were repeated after that the samples underwent two annealing processes. The first one was at about 1200 C and was carried out inside the facility at Legnaro National Laboratories, in a commercial oven, in argon atmosphere. The second one was at about 1900 C and was performed at Engineering Department of University of Trento, Mesiano, Italy, since the oven at LNL does not allow this temperature. The whole process took about 24 hours for both samples.

Experimental measurements of loss angle are reported in Figure 6.4 as a function of temperature. According to [4], annealing should improve the quality factor of the material in a double way. On one hand annealing should tidy up the disordered structure of infiltrated SiC, on the other it makes a fraction of total free silicon and carbon atoms react and bond together. Since a certain amount of dissipation is due to the free atoms, annealing should improve the quality factor. Having a look to the Figure 6.4, it seems that the improvement is less than a factor 2.

Again in Figure 6.4, a marked peak points out around 4K. The source of this dissipation is not known but the same loss behaviour appears also in other measurements in literature as for instance [4]. Measurement roughly agree with [4] in spite of the difference in the sample (in [4] SiC is made by reaction-bonding), both measurements show a minimum in loss angle at about 40K, with a subsequent raise up.

6.8 Infiltrated SiC measurement results.

Loss angle measurements of infiltrated SiC were performed both on cantilevers and disks. Differences in the samples are in size and carbon matrices. More details are reported in the followings subsections.

6.8.1 Measurements on cantilevers.

Loss angle measurements are performed on two cantilevers (3 and 4 in Table 6.2) of different length and thickness. Both samples are provided for Cesic Company, Germany. They differ also in carbon matrix size, but the company does not make public more information. All measurements were performed employing the capacitive readout for conductors, previously described in this chapter. Measurements were repeated after the cantilever 3 underwent annealing at 1900 C, in order to observe possible improvements in the quality factor.

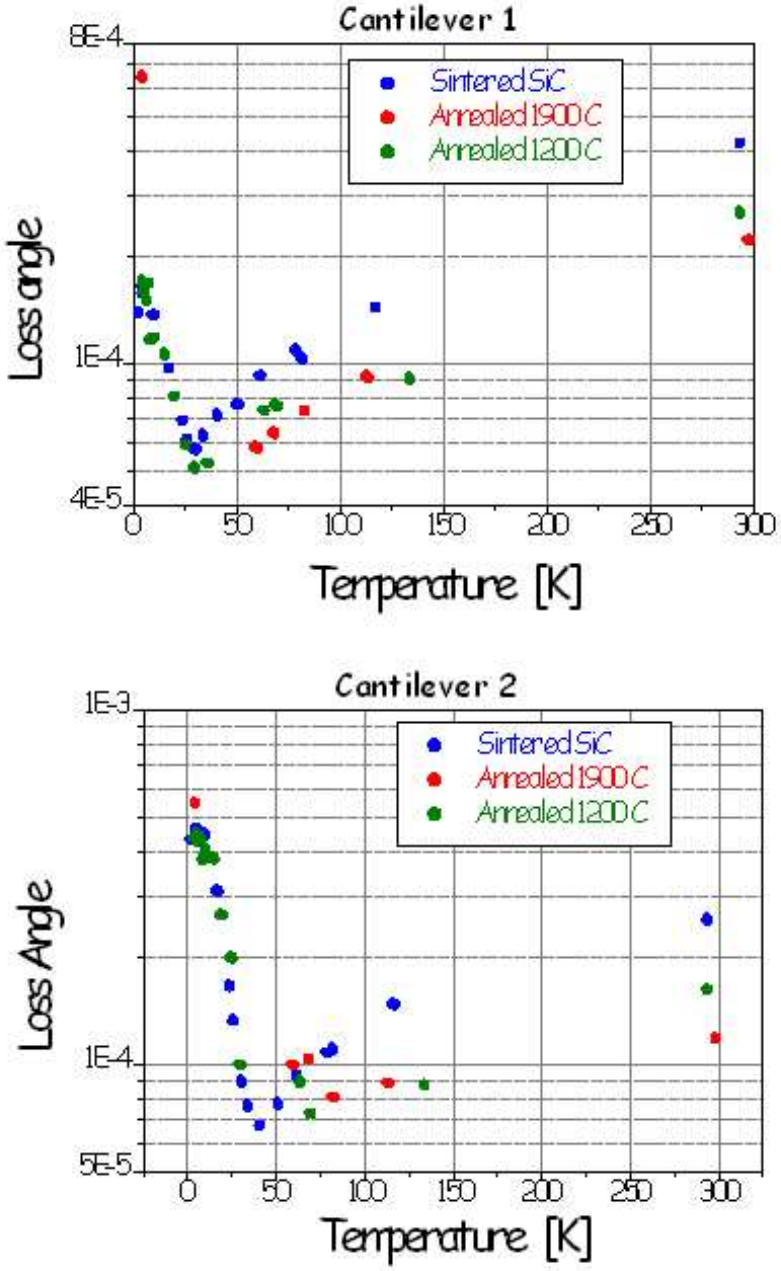

Figure 6.4: Loss angle measurements on Cantilevers 1 (top) and 2 (bottom) as a function of temperature. Measurements on SiC (blue), 1200 C (green) and 1900 C (red) annealed are reported.

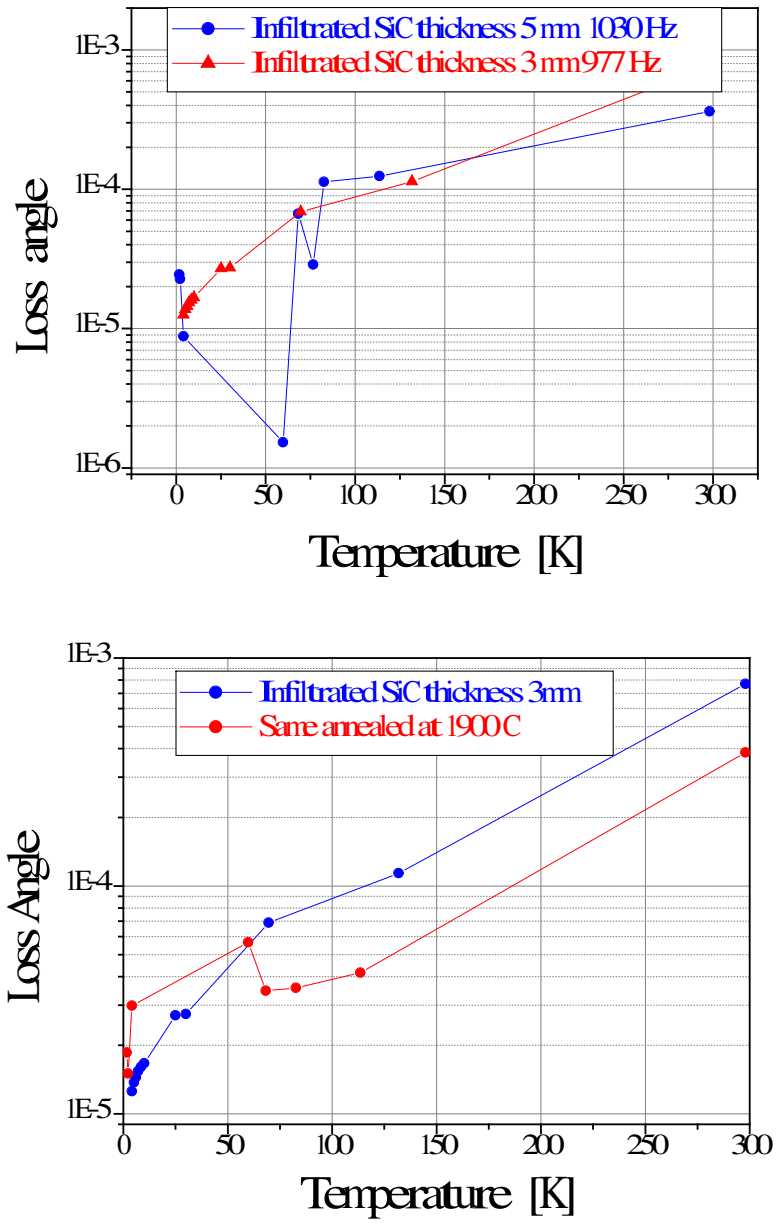

Figure 6.5: **Loss angle measurements on cantilevers 3 and 4.** (Up) Experimental result for infiltrated SiC loss angle as function of temperature on cantilevers 3 and 4. Samples differ in the carbon matrix. The measure at 60K scatters from the general trend and it should be repeated. (Down) Loss angle as function of temperature for cantilever 3 before and after annealing at 1900 C.

Figure 6.6: Sintered silicon carbide before (up) and after (down) annealing at 1900 C. The upper is cantilever 4, the lower cantilever 3.

In Figure 6.6, sintered SiC before and after annealing is shown. The superficial difference in grain size is visible. Data seems to indicate a moderate improving in the value of quality factor after the annealing, and a moderate dependence on the carbon matrix. In particular, the finer matrix shows slightly lower losses, probably due to more uniformity in the material.

6.8.2 Measurements on disks.

Loss angle measurements of infiltrated SiC were performed also on three disks (Disks 1, 2 and 3 in Table 6.2). Carbon matrix of disks differs each from others. The matrix of disk 1 is larger than that of disk 2. For each disk, two normal modes are investigated (see Figure 6.7). Frequencies vary according to different thickness. Really the modes shown in the picture are all doublets, whose frequencies are reported in Table 6.2. Unfortunately, signal line of Disk 3 broke during operations and loss measurements were impossible for that sample.

All loss measurements on disks 1 and 2 were collected and are reported in Figure 6.8. There is no evidence of a dependence of loss angle on temperature: this seems to indicate that the thermoelastic dissipation is not dominant. Furthermore there is no evidence of a dependence of loss angle on disk thickness: this fact could be interpreted inferring that the surface dissipation is not dominant.

Measurements give also some information on the dependence of in-

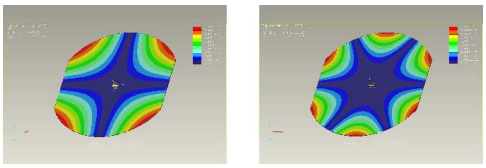

Figure 6.7: Normal modes of SiC disks under investigation. Frequencies vary according to the different thickness. Frequencies and other details are reported in Table 6.2.

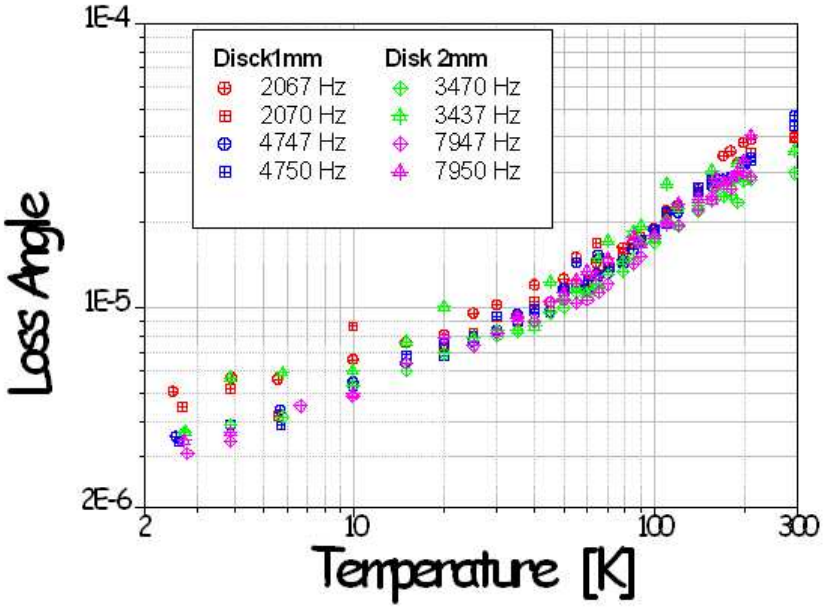

Figure 6.8: All loss angle measurements on disks 1 and 2 are collected as a function of temperature.

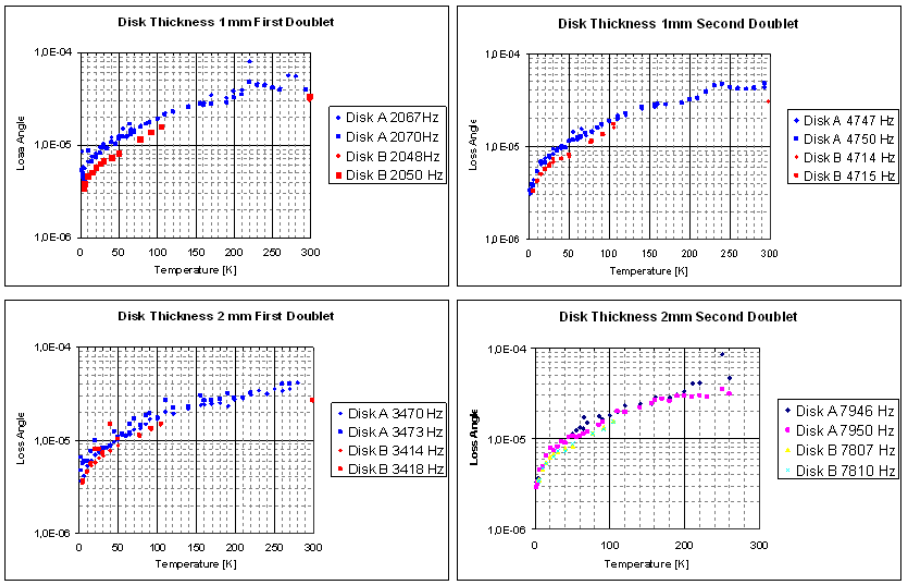

Figure 6.9: **C/SiC carbon matrix size effect.** Corresponding doublets losses are compared as function of temperature for disks 1 and 2. Losses dependence on carbon matrix size seems to be weak.

filtrated SiC losses on the carbon matrix size, having disks 1 and 2 two different ones. A weak evidence of dependence of measured loss angle on matrix size can be pointed out comparing measurements for corresponding doublets, as shown in Figure 6.9.

6.8.3 Losses measurements at ultra-cryiogenic temperature.

It can be pointed out as the dependence of loss angle on temperature becomes weak at low temperatures. For instance see Figure 6.8 for $T \lesssim 10K$. In the same range of temperature, also a weak logarithmic dependence of frequency shift on temperature can be pointed out (see Figure 6.10). Both these indications could not exclude the effect of quantum tunnelling at ultra-low temperature. In fact, the dissipation model of quantum tunnelling predicts such behaviour. An example can be found in [6] for amorphous solids. If losses are dominated by quantum tunnelling effect, losses should scale as T^{-3} below a crossover temperature (typically in the range $0.1 \div 0.5$ K).

In order to investigate this possibility, DUAL collaboration decided to start an ultra-cryogenic run. Measurements were performed at Low Temperature Laboratories, Physics Department, University of Trento, Italy, because in the meantime the LNL dilution refrigerator was under

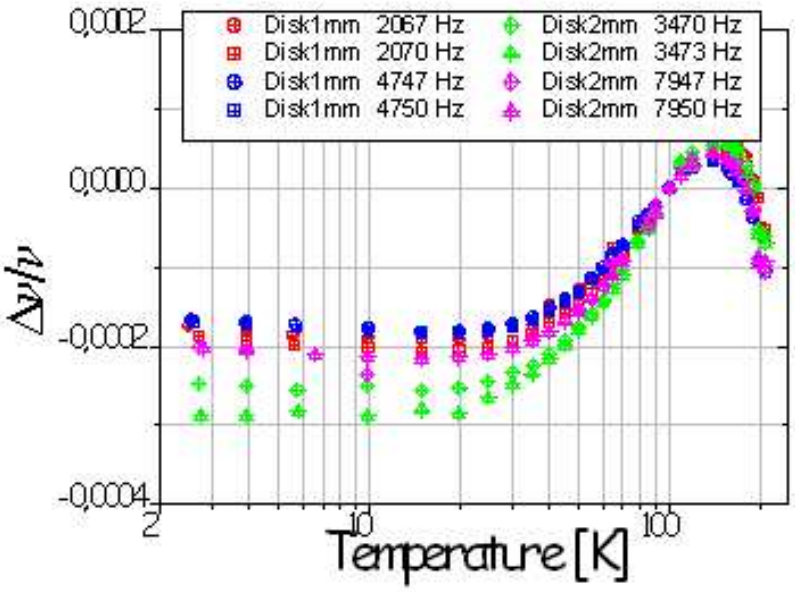

Figure 6.10: **C/SiC carbon matrix size effect.** Corresponding doublets losses are compared as function of temperature for disks 1 and 2. Losses dependence on carbon matrix size seems to be weak.

upgrading for the next (2008) ultra-cryogenic run. Trento facility is provided with an Oxford dilution refrigerator to perform ~ 50 mK as minimum temperature.

The experimental set-up is shown in Figure 6.11 in a picture. The set-up is arranged on two floors and houses two disks. In order to check the thermalization of the sample, upper floor houses disk 2 with a thermometer glued on its surface. No measurements are made on this sample. Lower basement houses disk 1 equipped with the capacitive readout previously described. Both disks are clamped by nodal suspension. All mechanical components except samples had been rearranged to fit the sizes of the Trento Facility. The whole OHFC copper frame shown in Figure 6.11 was assembled inside the LNL facility clean room and then carried to Trento where it was put inside the IVC of the cryogenic facility.

Losses measurements are shown in Figure 6.12. It results that loss angle decays slowly with temperature. The predicted trend $\phi \sim T^{-3}$ seems not confirmed by experimental data. Also frequency shift does not show the predicted logarithmic trend. One possible reason is the fact that the sample was not in thermal equilibrium with the mixing chamber, maybe due to the not good vacuum ($P > 10^{-5}$mbar). It is possible that the sample was systematically hotter than the mixing chamber. If this was the case, measurement has to be repeated improving the thermalization of the sample within the experimental apparatus.

6.9 Syngle Crystal SiC measurement results.

Loss angle measurements had been performed on Single Crystal SiC too, on the disks 4 and 5 (see Table 6.2). The two samples have the same size but they are made of two different SiC polytypes, 4H and 6H, respectively for disks 4 and 5. Some pictures of experimental set-up are shown in Figure 6.13. All measurements of losses as function of temperature are collected in Figure 6.14.

6.10 Losses sum up.

Summing up all measurements previously collected, it is worth to try to infer some information about both intrinsic and extrinsic losses in the investigated material. Here and throughout the followings we will refer to the losses scheme that was already drawn in the preceding Chapter 4 and the same nomenclature is adopted. In the followings

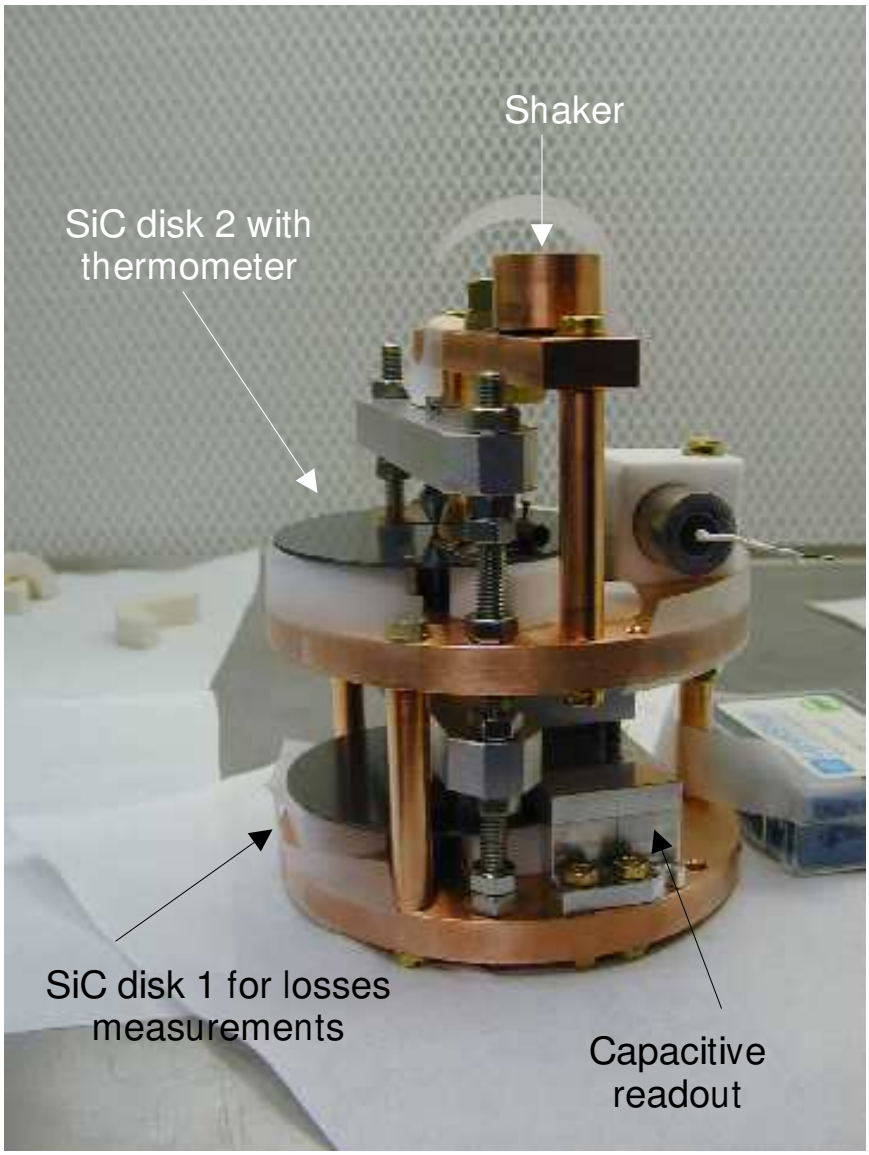

Figure 6.11: **Experimental set-up at Low Temperature Laboratories of Trento.**

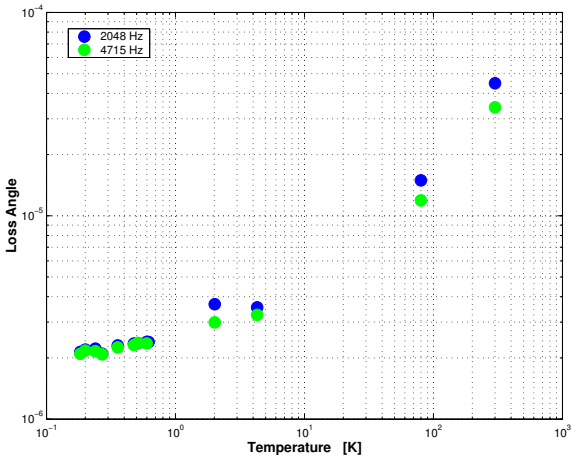

Figure 6.12: Measured losses of infiltrated Cesic SiC on disk 1 as function of temperature. All measurements are performed at Trento low temperature facility. Two modes was investigated, 2048 and 4715 Hz. Temperature values reported in the plot is the one measured on the sample with the thermometer glued on its surface.

some arguments about losses in the material are collected and grouped model by model.

Gas damping. During all SiC measurement sessions, the pressure inside IVC was always around $\sim 1 \times 10^{-6}$ mbar, except few experimental points around 4K for disks 1 and 2. In this range of pressure, according to the models already cited in the preceding Chapter 4, the gas damping contribute is negligible compared to the measured loss. Furthermore, this argument remains even more valid in the case of cited sqeezed-film model of Bao, and for disks 1, 2 and 3, since the damping due to the residual gas is in inverse relation to the thickness of the sample. These indications seems to suggest that gas damping is not a relevant dissipation mechanism in the SiC losses budget.

Thermoelastic effect. In Figure 6.8, in order to avoid confusion, measured loss of infiltrated SiC is plotted as function of temperature just for the highest frequency mode for each doublet. It is worth to remark how loss seems to be independent on the frequency, even if mode frequencies span from 2000 to 8000 Hz. This seems to indicate that the thermoelastic contribute is not the dominant one in the loss budget. In fact, thermoelastic losses depend strongly on the frequency of the considered normal mode,

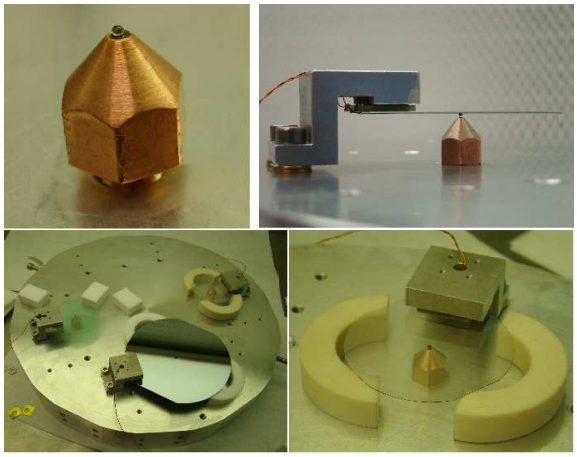

Figure 6.13: **Experimental set-up.** (Left top) A particular of the bottom disk holder is shown. The holder is screwed directly on the basement. On its top the 1mm diameter sapphire ball is glued, ready to be glued on bottom face of SiC disk. (Right top) Mono-Crystal SiC disk is shown in side view. The sample is provided with its small area "multistrip" capacitive readout for dielectrics. Glued nodal suspension and the gap are visible. (Left bottom) Picture shows how samples are arranged on the basement with their capacitive readouts. The two SiC disks and the bonded silicon wafer are visible. (Right bottom) A particular of 4H-SiC disk is shown. The two symmetric cuts are visible, one of them forefront, the other diametrically opposite.

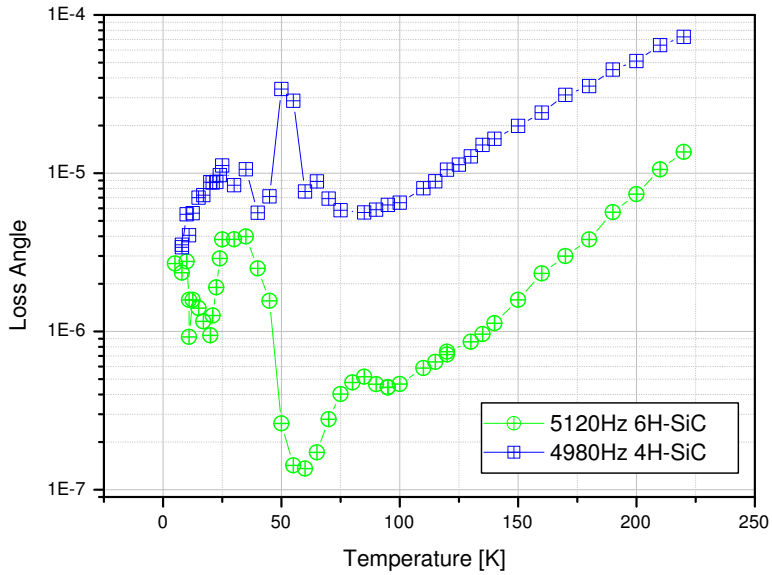

Figure 6.14: Measured losses of Mono-Crystal SiC on disks 4 and 5 as function of temperature. All measurements are performed at LNL TF. The investigated modes are 4980 Hz for disk 4 and 5120 Hz for disk 5. Frequencies refer to room temperature.

according the model already reported in the preceding Chapter 4. The theoretical estimation of thermoelastic losses in the case of infiltrated SiC is complicated by a series of difficulties. For instance, appropriated values for all needed thermal parameters are not easy to find. Partly this is due to the irregularities in the molecular structure deriving from the production processes and partly to the abundance of different polytypes. On the other hand, neither the manufacturer Cesic Company makes public the information about the carbon matrix of its product.

For what concerns mono-crystal 6H–SiC, its losses show a trend in temperature that could remember the typical thermoelastic curve as seen for silicon. A theoretical estimation of thermoelastic losses should be done soon and compared to experimental data, provided that all thermal parameters are known as function of temperature. This is still not available since measurements on 4H and 6H SiC are very late.

Superficial losses. Losses measurements on disks 1 and 2 could offer some information about superficial friction on sintered Cesic SiC. In fact, the disks' thicknesses are 1 and 2 mm, respectively, and the volume-surface ratio is almost each double the other. [1] But experimental data in both samples show about the same losses. This seems to suggest that superficial losses are negligible in sintered SiC.

Suspension losses. As regards infiltrated Cesic SiC, we measured losses on a cantilever and on a disk characterized by the same grain. Losses measured on disk were lower by a factor two than losses measured on cantilever. This suggests that, for cantilevers, clamping loss is of the same order of magnitude of the measured loss angle.

Nodal suspension on disks 1, 2 and 3 produced an improvement in measured quality factor, however its contribution to total losses seems to be not so negligible. On the other hand, the lowest measured loss angle glued on disk 5 suspended with nodal suspension is about 1.5×10^{-7}. But disk 5 is of mono-crystalline SiC, while disks 1,2,3 are of infiltrated Cesic SiC; this seems to indicate that probably the main contribution to measured losses is not due to suspension but to intrinsic sources.

Loss due to glue. Loss angle measurements were performed on the

[1] For a cylinder of radium r and height h, the Volume-Surface ratio is $rh/2(r+h)$. If $h \ll r$ then roughly the Volume-Surface ratio is $\sim h/2$.

same sample, clamped first without and then with glue on the central nodal spheres. Measurements were performed in two different runs, removing and then replacing back the sample in its holder. Measured loss angle in the two cases agree as function of temperature. This seems to suggest that a tiny drop of glue in the central notch between the disk and the clamping sphere does not contribute significantly in the total losses budget.

Carbon matrix loss. Disk 1 has the carbon matrix larger than that of the disk 2. This allows to estimate differences in losses due to the matrix. As already dealt with previously in this chapter, a weak evidence of dependence of measured loss angle on matrix size can be pointed out comparing measurements for corresponding doublets, as shown in Figure 6.9.

Bibliography

Bibliography for Chapter 5.

[1] C.Kittel, *Introduction in solid state physics.*, Wiley & sons, 7th edition

[2] P.G.Neudeck, A.J.Trunek, D.J.Spry, J.A.Powell, H.Du, M.Skowronski, X.Huang, M.Dudley, CVD growth of 3C-SiC on 4H/6H mesas, (2006) technical report.

[3] P.M.Sarro, *Silicon Carbide as a new mems technology*, Sensors and Actuators A, **82**, 210-218

[4] E.K.Hu *et al.*, Phys.Lett. A **157**, 209 (1991)

[5] R.N.Kleiman, G.Agnolet, D.J.Bishop, *Two-Level Systems obseved in the mechanical properties of single-crystal silicon at low temperature*, Phys.Rev.Lett., **59**, 18, 2079-2082

[6] K.A.Topp, David G.Chaill, *Elastic properties of several amorphous solids and disordered crystals below 100K*, Z. Phys B **101**, 235-245 (1996)

Chapter 7

Conclusions and perspectives.

Despite its good characteristics in terms of cost and machinability in large size, sintered and infiltrated SiC showed too large losses down to 3K to be employed in the carrying out of the sensitive mass for DUAL gravitational waves detector. Unfortunately measurements on infiltrated SiC down to ~ 0.2 K at Trento Facility did not give the expected results. Measured loss is still too large to allow the employment in carrying out the resonator mass. On the other hand, both measured loss angle and frequency shift showed a trend different from the expected one due to the Tunnelling Model of Two Level System, that should give the most contribute to losses in this temperature range. This seems to suggest that maybe measured loss had an extra contribute from external losses whose sources are to be found in the experimental apparatus. Some ultra-cryogenic measurements were performed at Trento Facility but most of all were performed at LNL Test Facility. The latter site offers slighter better performances, as it allows loss angle measurements down to 20mK and intrinsic loss measurements are already performed at cryogenic temperature in the case of thermoelastic of silicon wafers. Probably the first ultra-cryogenic run will start in the first months of the current year. However further tests should be tried for sintered and infiltrated silicon carbide as, for instance, annealing sintered SiC samples for longer time and loss angle measurements down to 20 mK (available at LNL TF).

Mono-crystalline silicon carbide showed the lowest measured loss angle 1.4×10^{-7} around 60K (in polytype 6H). This value is better than both sintered and infiltrated SiC but it is still slighter high to choose 6H-SiC to manufacture the DUAL test mass. Moreover this polytype does not lend itself to be machined in large size, and this

could make difficult to carry out the DUAL resonator. Maybe manufacturing technology will be able to carry out large size masses of mono-crystalline SiC in a far future. For what concerns mono-crystal 6H-SiC, its losses show a trend in temperature that is not saturated for low temperature. Ultra-cryogenic measurements should be thus performed. Anyway, even for this polytype the production is limited to small sizes.

Mechanical losses introduced by post processing treatments on silicon wafers have been measured in $3 \div 300$K temperature range and in $300 \div 4000$Hz frequency band. The main contributing loss mechanisms were identified. The thermoelastic damping, computed in the case of measured anisotropic wafers by a FEM model, was shown to dominate the lowest loss normal mode within $40 \div 300$ K temperature range. Surface losses and residual clamping losses are estimated to give the largest contribution to measured loss in the remaining $3 \div 40$ K temperature range.

As concerning bonding, the maximum bond losses that would allow the construction of a sensitive DUAL detector in silicon depend critically on the detector configuration, at present still not decided. However we can give a rough approximation of the maximum tolerable losses in the following pessimistic case, since it enhances the effect of bond layers. Let us consider to build a silicon body of volume $V_{tot} = 1m^3$ by bonding together 10^3 cubes with edge length of 0.1m. Let the faces of adjacent cubes be bonded over their whole surface and let $h_b = 100$nm be the bond thickness. Thus the total volume of the bond layers is $V_{bond} \sim 3 \times 10^{-7} m^3$. Then, if such mass has to show losses at the level of $\phi_M \sim 10^{-8}$ at 4K, the bond losses ϕ_{bond} should be

$$\phi_{bond} \lesssim \frac{V_{tot}}{V_{bond}} \phi_M = 3 \times 10^{-3} \tag{7.1}$$

Our sensitivity is thus enough for the purpose of constructing a DUAL gravitational wave detector if the hydroxyl-catalyzed bond is a good approximation. It is worth to remark that the sensitivity could be optimized by choosing a clever topology for the bonded sample. For instance at room temperature a thicker sample would suffer less from the thermoelastic damping and thus lead to a better sensitivity.

Appendix A

Thin circular disk vibrations.

A.1 Introduction.

Huang *et al.* [6] dealt with the theoretical analysis of dynamic characteristics for circular flat disks in the case of piezoceramics materials, considering the electric field - displacement coupling. Here the authors' results are reviewed to obtain a better insight into the normal modes of disk samples employed for all the measurements reported previously in the chapters of this thesis.

A.2 Elastic model.

In Figure A.1 the geometrical configuration of disk with radius R and thickness h is shown. The cylindrical coordinates (r, θ, z) are chosen, with the origin in the centre of the disk. Cited authors express the governing equations and basic hypothesis needed to analyse the vibration characteristics of the piezoceramics disk following Rogacheva [6, and therein ref.(17)]. Besides they consider the linear piezoceramics constitutive equations coupling displacement and electric field. Here this coupling is neglected in order to obtain from the authors' equations the pure elastic equations of motion, whose eigensolution are the normal modes for our disk sample. To this aim it is sufficient to put $d_{ij} = \varepsilon_{ij} = 0$ in linear system [6, therein eq.(3)]. Consequently it is $k_p = 0$ in following eq.(11) and hence it results $D' = Yh^3/12(1-\nu_p^2) \equiv D$ in eq.(13), where Y is the isotropic Young's modulus and ν_p the Poisson's ratio. According to cited authors, the basis hypotheses non-involving electric field are

- Normal stress σ_{zz} can be neglected relative to other stresses, hence $\sigma_{zz} = 0$.

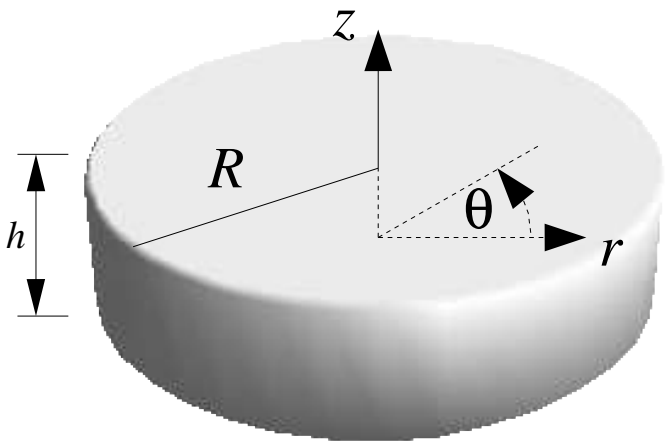

Figure A.1: Geometry and coordinate system of the disk. The cylindrical coordinate system is shown. The radius is R and the thickness is h.

- The rectilinear element normal to the middle surface before deformation remains perpendicular to the strained surface after deformation, and its deformation can be neglected, i.e. $\epsilon_{rz} = \epsilon_{\theta z} = 0$.

Finally, because the circular disk is thin, the out-of-plane (transverse) vibration and the in-plane (tangential and extensional) vibrations are decoupled. In the following section, as the thermoelastic dissipation was evaluated for samples' pure flexures, the transverse vibration is analysed in details, giving the main contribute to the total thermoelastic dissipation.

A.3 Transverse vibrations.

Let $w(x, y)$ be the displacement in the z-direction. We look for solutions such as the displacement is harmonic in time with amplitude depending only by the point over the middle plain, i.e.

$$w(r, \theta, t) \equiv W(r, \theta) e^{i\omega t}, \tag{A.1}$$

where ω is the angular frequency and t the time coordinate. In this case, the governing equation of free transverse vibrations has the following form:

$$\nabla^4 W - \frac{\rho h \omega^2}{D} W = 0, \tag{A.2}$$

where ∇^4 is the bi-harmonic operator, ρ is the density and D is the flexural rigidity just defined in the previous section. The solutions of

eq.(A.2) can be written as

$$\begin{aligned} W^{+}(r,\theta) &= \cos(a\theta)\left[B_{n,a}J_a(\beta_{n,a}r) + C_{n,a}I_a(\beta_{n,a}r)\right] \\ W^{\times}(r,\theta) &= \sin(a\theta)\left[B_{n,a}J_a(\beta_{n,a}r) + C_{n,a}I_a(\beta_{n,a}r)\right] \end{aligned} \tag{A.3}$$

where $n = 0, 1, 2, 3, \ldots$, $B_{n,a}$ and $C_{n,a}$ are constants and it is

$$\beta_{n,a}^4 \equiv \rho h \omega_{n,a}^2 / D. \tag{A.4}$$

In the above equations (A.3), J_a is an nth order Bessel function of the first kind and I_n is an nth order modified Bessel function of the first kind. Following the cited authors but adjusting the equations for the case of our sample, the constants $B_{n,a}$ and $C_{n,a}$ can be determined applying the circumferential-free boundary conditions at $r = R$ [6, eqs. (15a) and (15b)], but putting $d_{ij} = \varepsilon_{ij} = 0$ and $k_p = 0$. These equations give a system of two linear equations [6, therein eq. (16a,b), but with $k_p = 0$] to be solved in the coefficients $B_{n,a}$ and $C_{n,a}$. In order to obtain a non trivial solution for the constants $B_{n,a}$ and $C_{n,a}$, the determinant of coefficient matrix must be equal to zero; that yields the characteristic equation of resonant frequencies for transverse vibrations [6, therein eq.(17)], to be solved in the variable $\xi_{n,a} \equiv \beta_{n,a}R$. This equation is rearranged here in (A.5) with $d_{ij} = \varepsilon_{ij} = 0$ and $k_p = 0$.

$$\begin{aligned} \frac{(1-\nu_p)\left[n^2 J_n(\xi_{n,a}) - \xi_{n,a}J_n'(\xi_{n,a})\right] - \xi_{n,a}^2 J_n(\xi_{n,a})}{(1-\nu_p)\left[n^2 I_n(\xi_{n,a}) - \xi_{n,a}I_n'(\xi_{n,a})\right] - \xi_{n,a}^2 I_n(\xi_{n,a})} = \\ \frac{(1-\nu_p)n^2\left[J_n(\xi_{n,a}) - \xi_{n,a}J_n'(\xi_{n,a})\right] - \xi_{n,a}^3 J_n'(\xi_{n,a})}{(1-\nu_p)n^2\left[I_n(\xi_{n,a}) - \xi_{n,a}I_n'(\xi_{n,a})\right] - \xi_{n,a}^3 I_n'(\xi_{n,a})} \end{aligned} \tag{A.5}$$

Solving eq. (A.5) in the variable $\xi_{n,a}$, the eigen-frequencies $\omega_{n,a}$ are obtained, remembering the definition (A.4).

It should be noted that a labels the numbers of nodal diameters, n the number of nodal circles and $s \equiv +, \times$ is the symmetry index of the displacement fields. A solution is fully identified by the set (a, n, s). The orthogonal displacement fields $W^{+}(r,\theta)$ and $W^{\times}(r,\theta)$ stand for mode doublet. They have the same radial distribution of the deformation, mutually rotated by $\pi/2a$, and share the same $\beta_{n,a}$. When $a = 0$ the doublet merges in a single solution with rotational symmetry around the z-axis.

In the case of silicon, the solutions in equations (A.3) are approximated because Young's modulus is anisotropic, i.e. its value varies along different direction in the material (see section 4.10 in the text of this thesis). In order to take into account also the material's anisotropy and the real shape of our samples (different from circular because of

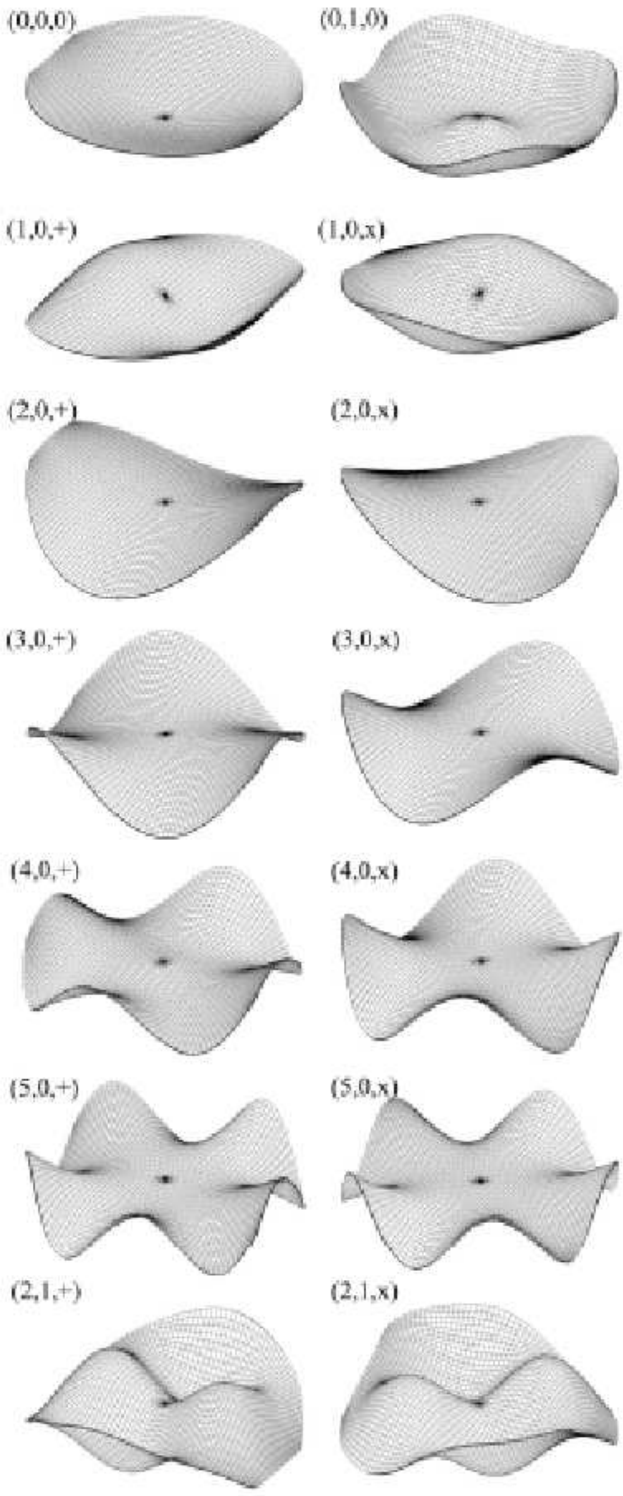

Figure A.2: Plot of the first 13 eigenmodes of the model described in the text. The displacement evaluation is performed by FEM analysis, ordered according to the (a, n, s) indexes and taking into account the material's anisotropy and the real geometry of silicon samples.

the two symmetric cuts), a FEM model of the wafer was developed employing commercial software [7]. Similarly to the experimental apparatus, also in the FEM model the wafer is clamped by both sides. The contact is modelled on two small circular areas with diameter 0.5 mmm around the centre of the disk, similarly to the real sample.

As resulting from FEM simulations with this model, the stiffness anisotropy and the flat cuts induce a splitting of the frequency of the mode doublets. This splitting is quite large for $a = 1$, when the modes are mutually rotated by $\pi/2$ and the effect of the flat cuts is maximized, and for $a = 2$, when the modes are mutually rotated by $\pi/4$ and the effect of stiffness anisotropy is maximized. In Figure A.2 the first 13 eigenmodes of the model are plotted with solution of the type described by equations (A.3). The (a, n, s) indexes of the corresponding mode in the isotropic case are also shown. it should be remarked that FEM analysis predicts the existence of "cantilever" modes of the disk pivoting around its suspension point. Such kind of solution cannot be described by periodic functions in θ. These modes depend crucially on the suspension details.

Appendix B

Temperature dependence of mode frequency.

The frequency of each normal mode changes with temperature according to the temperature dependence of all parameters that frequency is function as. It results that the eigenfrequencies depend on temperature mainly via the Young's modulus dependence of temperature. Then there is the possibility to estimate experimentally the Young's modulus of the material measuring the frequency as a function of temperature. In our case, the frequency measurement is always coupled to loss angle one. In fact, the ring down method employed to measure the loss angle offers a very accurate measurement of the resonant frequency, due to the employment of HP3325B synthesizer with high stability frequency reference. In the followings eigenfrequency and Young's modulus temperature dependence, experimental measurements with an estimate of the parameters, and a brief description of the problem to determine the Young's modulus in anisotropic materials are described.

B.1 Frequency of thin disk normal modes.

Let us consider a thin flat circular plate of uniform thickness t and radius r. Let the edges of plate be free. Let ω be the uniform load per unit area including own plate weight and ν be the (silicon, in our case) Poisson's ratio. The mode frequencies of the homogeneous circular flat plate is then [1]:

$$f = \frac{k_n}{2\pi}\sqrt{\frac{Dg}{\omega r^4}}, \tag{B.1}$$

where

- k_n is a coefficient that depends on the mode geometry. Some values are the followings:
  - $k_1 = 5.25$ two nodal diameters;
  - $k_2 = 9.08$ one nodal circle;
  - $k_3 = 12.2$ three nodal diamenters;
  - $k_4 = 20.5$ one nodal diameter and one nodal circle.
- $D = \frac{Et^3}{12(1-\nu)}$
- E is the modulus of elasticity (or *Young's modulus*).

The temperature dependence of the geometrical dimensions is weak. For our sample the difference between few K and room temperature is less than 0.5%, which is negligible if compared with the temperature changes of Young's modulus E in the same temperature range. Thus we can assume that the eigenfrequencies f_n depend on temperature via the temperature dependence of the Young's modulus $E(T)$.

B.2 Young's modulus temperature dependence.

The temperature dependence of the Young's modulus E is due to anharmonic effects of the lattice vibrations. Wachtmann *et al.* [2] suggested a semi-empirical formula which is valid for silicon in the high-temperature limit [3]:

$$E(T) = E_0 - BT \exp\left(-\frac{T_0}{T}\right) \tag{B.2}$$

where E_0 is the Young's modulus at 0K. The constants $B > 0$ and $T_0 > 0$ are temperature independent. Wachtman expected a correlation between T_0 and the Debye temperature Θ_D and between B and the Grueneisen parameter γ. Recently Gysin *et al.* reviewed that (in the limit of high temperature) it results

$$B = \frac{R\gamma\delta}{V_0} \quad \text{and} \quad T_0 \approx \frac{\Theta_D}{2} \tag{B.3}$$

where R is the gas constant, δ is the Anderson-Grueneisen parameter and V_0 is the volume at 0K. Putting the (B.2) in the equation (B.1), it results the frequency temperature dependence law.

B.3 Experimental measurements.

For each normal mode, frequency measurements as function of temperature are performed together with the loss angle measurements by the so-called ring down method described in Chapter 4. A lockin amplifier demodulates the signal from the displacement readout and gives the amplitude of vibration (in Volts) at the eigenfrequency. A synthesizer with high stability frequency provides lockin reference. While mode amplitude is decaying after excitation, phase slope is made vanish simply fine-tuning the frequency reference on the synthesizer. The lockin reference gives the experimental measurement of the eigenfrequency at the temperature of the experimental set-up during the measurement. An incidental difference between the reference frequency ν_{ref} and the mode frequency ν_m appears as a linear evolution of the lockin phase $\phi(t)$ described by the following equation:

$$\phi(t) = \phi_0 + 2\pi(\nu_{ref} - \nu_m)t. \tag{B.4}$$

A very accurate measurement of the eigenfrequency ν_m can be obtained by a linear fit of $\phi(t)$ by the B.4, that provides a measure of the difference $\Delta \equiv (\nu_{ref} - \nu_m)$.

Frequency data as function of temperature have been collected for the 0.5 mm thick silicon disk, both for squared blind and circular through central hole. All measurements are performed employing the capacitive readout. Each frequency against temperature experimental curve has been fitted using the model in equation (B.1) with the Young's modulus in equation (B.2). Table B.1 collects the parameters values with respective errors experimentally obtained in this way for three modes of the silicon sample, the ones that show the lowest loss angle.

The values agree very well within errors even for the two different central holes. Scattering in errors and values maybe depends on the different amount of data points for each mode. In particular, all fits were repeated changing the nominal temperature with the inferred sample temperature, as resulting from experimental measurements of a special cryogenic run, purposely dedicated to thermometers calibration (for details see section 4.7). The values of parameters did not show significant changes. However in Table B.1 the parameters values are reported as resulting from the fit with inferred temperature. It is worth to remark that the obtained values agree well with literature (for example see [5, and therein]). The mean measured value for the Debye temperature is $\Theta_D = 638$ K. the deviation from literature value 645 K [5, and therein] is $\sim 1\%$. The good agreement seems to justify

Hole	ν_0 [Hz]	E_0 [GPa]	B [Mpa/K]	T_0 [K]
Blind	~ 1729.5	167.50 ± 0.04	15.83 ± 0.05	316 ± 7
Through	~ 1728.5	167.50 ± 0.03	15.80 ± 0.03	325 ± 8
Blind	~ 2528.0	167.50 ± 0.03	15.80 ± 0.03	310 ± 8
Through	~ 2512.5	167.50 ± 0.05	15.80 ± 0.03	319 ± 7
Blind	~ 381.9	167.503 ± 0.007	15.80 ± 0.02	328 ± 11
Through	~ 384.7	167.5 ± 0.6	15.8 ± 0.9	317 ± 25

Table B.1: **Fit results.** The table shows the parameters estimation made by the fit of the measured mode frequency as a function of the temperature using the model described in the text. Measurements are performed on silicon disks with both blind and through central hole, as indicated in the first column. The frequency ν_0 in the second column is the approximated value of mode frequency at 4 K. E_0 and B are Young's and bulk modulus. T_0 is related to the Debye temperature; empirical reasons suggest that should be $\Theta_D/2$.

the approximation $\Theta_D \approx 2T_0$, to be valid in a low temperature range also. In particular for Young's modulus at 0 K, E_0, the value agrees to the literature one for the (110) direction of silicon. However, a brief discussion about the physical sense to give to these measurements is reported in the next subsection.

In Figure B.1 an example of fit is shown. It is reported the measured frequency temperature dependence for the mode (13). The two data sets refer to the two samples with blind hole (black markers) and through one (blue markers). The resulting parameters evaluation is reported in Table B.1. It is remarkable the fact that the model does not fit few experimental points at high temperature. Probably this is due to some problems in the thermalization of the sample. However it seems that this problem does not invalidate the results, since the parameter values agree with literature as discussed above.

B.4 The Young's modulus in anisotropic materials.

Silicon is an anisotropic material, i.e. it shows different values of its Young's modulus along different directions in it. Then it arises the problem to understand the physical sense of the Young's modulus measured with the experimental procedure described above. Landau [4, on page 37] defines the Young's modulus for an anisotropic material as the ratio between the stress and strain projections along a fixed direction

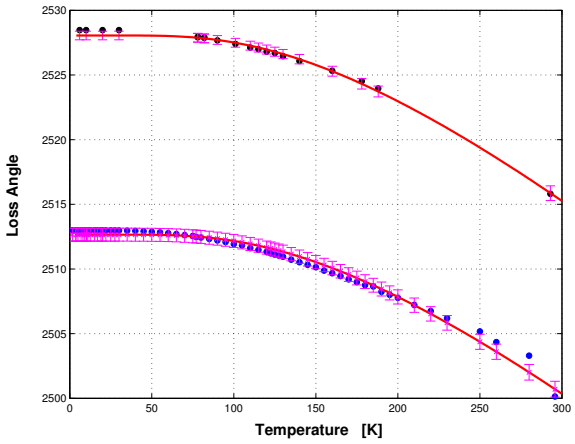

Figure B.1: **Example of fit on frequency VS temperature experimental data.** Measured frequency for the both samples with blind hole (black circles) and through one (blue circles) is reported as function of temperature. Red continuous lines are the respective best fitting curve with the model described in the text.

in the crystal. He solves the problem for the specific case of a cubic crystal (the same of silicon) and finds the expressions of the Young's modulus as a function of the coefficients that relate the free energy to the strain tensor.

In general, let $P(x, y, z)$ be a chosen point in the considered body. As reference system, the lattice crystal one can be chosen for simplicity, so that x, y and z are the reticular directions. Let the body be in vibration on a certain normal mode with its fixed geometry. The point P will undergo the mean displacement $\langle \mathrm{u}(\boldsymbol{x}, \boldsymbol{y}, \boldsymbol{z}) \rangle$, according to the shape of the considered normal mode. Let the longitudinal axis of a rod cut from the crystal in $\boldsymbol{P}$ be along a the unit vector $\hat{\boldsymbol{n}}$, directed parallel to the mean displacement $\langle \mathrm{u}(\boldsymbol{x}, \boldsymbol{y}, \boldsymbol{z}) \rangle$. The stress tensor $\boldsymbol{\sigma_{ij}}$ in the stretched rod must satisfy the following conditions:

- $\boldsymbol{\sigma_{ik} n_k} = \boldsymbol{p n_i}$, where $\boldsymbol{p}$ is the tensile force on unit area on the ends of the rod (condition at the ands of the rod);

- for the direction $\hat{\boldsymbol{t}}$ perpendicular to $\hat{\boldsymbol{n}}$, $\boldsymbol{\sigma_{ik} t_k} = \boldsymbol{0}$ (condition on the sides of the rod).

Such a tensor necessarily must have the form $\boldsymbol{\sigma_{ij}} = \boldsymbol{p n_i n_j}$. Recalling the general expression [4, eq.(4.8), page 11] for the strain tensor $\boldsymbol{u_{ij}}$ [1]

[1] Here the same letter $\boldsymbol{u}$ is used both for displacement and strain. This should not

in terms of the stress tensor $\boldsymbol{\sigma_{ij}}$, the components of the strain tensor result to be:

$$\boldsymbol{u_{ii} = p\left(\frac{1}{9K}\frac{1}{6\mu}\right) + \frac{p}{2\mu}n_i^2, \qquad u_{ij} = \frac{\sigma ij}{2\mu} = \frac{p}{2\mu}n_i n_j \quad (i \neq j),} \tag{B.5}$$

where $\boldsymbol{K}$ and $\boldsymbol{\mu}$ are respectively the *bulk modulus* and *shear modulus*.

The relative elongation of the rod around the point $\boldsymbol{P}$ is $\boldsymbol{u = (dl' - dl)/dl}$ where $\boldsymbol{dl'}$ is given by [4, eq.(1.2), page 1] $\boldsymbol{dl'^2 = dl^2 + 2u_{ik}dx_i dx_k}$. In our case it is $\boldsymbol{dx_i/dl = n_i}$. For small deformations this gives $\boldsymbol{u(x,y,z) = u_{ik}(x,y,z)n_i n_k}$. Finally the Young's modulus is determined in the point $\boldsymbol{P(x,y,z)}$ by the proportionality factor in $\boldsymbol{p = E(x,y,z)u}$, and it is found to be given by

$$\boldsymbol{\frac{1}{E} = \left(\frac{1}{3K} - \frac{1}{2\mu} + \frac{p}{2\mu} + \frac{1}{2\mu}\left(n_1^2 n_2^2 + n_1^2 n_3^2 + n_2^2 n_3^2\right)\right)} \tag{B.6}$$

The Young's modulus measured by the experimental procedure described in previous subsections should result in an *average* value of $\boldsymbol{E(x,y,z)}$ over the whole volume of the body:

$$\boldsymbol{\langle E\rangle = \frac{1}{V}\int_V E(x,y,z) \quad dxdydz} \tag{B.7}$$

Standard FEM software should provide, as result of analysis on each normal mode, the mean displacement (i.e. averaged over one oscillation) and the strain tensor for each node or cell. If this is case, unit vector $\boldsymbol{\hat{n}}$ is identified by the displacement direction ($\boldsymbol{\hat{n}(x,y,z)} = \langle$ u$\boldsymbol{(x,y,z)}\rangle$. Then the integral in equation (B.7) can be evaluated numerically over all nodes or cells and compared with the experimental measurement. Provided the FEM data being available, the above described procedure can be applied to the experimental measurements reported in the present thesis.

induce confusion because the displacement is a *vector* with just one suffix, while stain is a (symmetric) *tensor* with two suffixes.

Bibliography

Bibliography for Appendices.

[1] Roark, *Roark's formulas for stress and strain.*

[2] J.B.Wachtman *et al.*, *Exponential Temperature Dependence of Young's Modulus for Several Oxides*, Physical Review, Vol. 122, N. 6, 1754-1759, (1961)

[3] M.L.Nandanpawar and S.Rajagopalan, *Qachtman's equation and temperature dependence of bulk moduli in solids*, J. Appl. Phys. **49**(7), 3976-3979, July 1978.

[4] L.D.Landau and E.M.Lifshitz, *Theory of elasticity*, ed. Pergamon Press, 1986.

[5] U.Gysin *et al.*, Phys. Rev. B **69**, 045403 (2004)

[6] C.H.Huang, Y.C.Lin and C.C.Ma, *Theoretical analysis and experimental measurement for resonant vibration of piezoceramics circular plates.*, IEEE transactions on ultrasonics, ferroelectrics and frequency control, Vol. 51, No 1, Jan 2004

[7] J.P.Zendri *et al.*, article in preparation.

Acknowledgments.

The first thanks are for my family that supported me during all these years. In them I had always found help, encouragement and love, most of all in hardest times.

I would thank my wife Chiara who always stood by and patiently supported me at all difficult times with all her love.

I would give special thanks to dr. Jean-Pierre Zendri, whose contribution in the draft of this work is essential. He will always be a teacher for me.

Thanks to Michele who embellished this thesis with many very beautiful drawings.

Finally I would thank all DUAL collaboration for the opportunity they gave me to understand many things about experimental physics of gravitational wave detection.

I would dedicate this work to Francesco, my dead father, and Francesco, my newborn son.